Characterization of Photonic Quantum Dots with Coherent Scattering Methods

Zur Erlangung des akademischen Grades eines
DOKTORS DER NATURWISSENSCHAFTEN
von der Fakultät Physik des
Karlsruher Instituts für Technologie (KIT)

genehmigte

Dissertation

von

Dipl. Phys. Markus Riotte
aus Saarbrücken

Tag der mündlichen Prüfung: 16.12.2011

Referent: Prof. Dr.rer.nat. T. Baumbach

Korreferent: Prof. Dr. D. Schaadt

Kurzfassung

Inhalt dieser Arbeit ist die Charakterisierung von lichtemittierenden Halbleiterquantenpunkten mit Röntgenstrahlung. Die Arbeit besteht aus zwei Teilen:
Im ersten Teil wird eine "in-situ" anwendbare Mess- und Analysemethode entwickelt, mit Hilfe derer sich Gestalt, Verdehnung und chemische Zusammensetzung von Quantenpunkten messen lässt. Zu diesem Zweck wird ein bereits existierendes Streumodell, das "iso strain scattering" (ISS) Modell, durch zusätzliche Berücksichtigung des Streubeitrags des Substrates unter und zwischen den Quantenpunkten angepasst. Das Ergebnis ist ein ganzheitliches Model, das in dieser Arbeit "Holistic Iso Strain Scattering" (HISS) Modell getauft wird. Es ermöglicht, in wenigen Schritten Schlüsselinformationen aus den Röntgenstreudaten zu extrahieren. Die experimentellen Anforderungen können aufgrund des geringeren Bedarfs an Messpunkten im Vergleich zu konventionellen Herangehensweisen reduziert werden. Die Methode ist dadurch robust, schnell und "in-situ" anwendbar.
Im zweiten Teil der Arbeit werden verschiedene Quantenpunktproben mit den Röntgenmethoden charakterisiert. Dabei kommen sowohl die neu entwickelte Methode, basierend auf dem HISS Modell, als auch konventionelle Methoden zum Einsatz. In diesen Studien werden Gestalt, Größe, Verspannung, chemische Zusammensetzung und Anordnung der Quantenpunkte zueinander in Abhängigkeit der Herstellungsparameter gemessen. In einer ersten Studie werden die Auswirkungen von Erwärmungsphasen nach abgeschlossenem Wachstum untersucht. In einer zweiten Studie werden Proben mit verschiedenem Aluminiumgehalt verglichen und so der Einfluss der chemischen Zusammensetzung auf die Quantenpunkteigenschaften untersucht. Resultierend werden die Herstellungsparameter, die sich daraus ergebenden Eigenschaften und schließlich die Qualität der Lichtemission miteinander in Zusammenhang gebracht.

Abstract

Subject of this thesis is the characterization of light emitting semiconductor quantum dots with x-rays. The thesis consists of two parts:
In the method development part a measurement routine and analysis procedure for in-situ measurements of shape, strain and chemical composition of quantum dots is developed. For this purpose an already existing scattering model, the iso strain scattering (ISS) model is adapted by including the contribution of the substrate below and around the dots. The result is a holistic iso strain (HISS) model. It allows to extract key information from scattering data within very few steps. The experimental requirements can be relaxed due to a reduced need of data. The method is robust, fast and in-situ applicable.
In the second part of the thesis different quantum dot samples are characterized with x-ray methods. Thereby the new technique based on the HISS model, that was introduced in the first part of the thesis, and conventional techniques are used. In those studies the quantum dot parameters such as shape, size, strain, chemical composition and positional ordering are measured in dependence of the production parameters. In a first study the effects of post growth annealing are investigated. In a second study samples with different aluminum contents are compared in order to study the effect of chemical composition on the quantum dot properties. In conclusion the production parameters, the resulting quantum dot properties and the quality of the light emission are related to each other.

Danksagung

Meinem Doktorvater Herrn Prof. Dr. Tilo Baumbach danke ich für die wunderbaren Chancen und Möglichkeiten, die er mir an seinem Institut eröffnet hat. Seine wegweisenden Ratschläge und Ideen schufen das Fundament für diese Arbeit und meinen beruflichen Werdegang.
Herrn Dr. Daniil Grigoriev danke ich für die vielen Stunden, in denen er mich unermüdlich in die Details der Röntgenstreuexperimente und der Röntgenstreutheorie eingeführt hat. Aus seinem breiten Wissensfundus konnte ich unentwegt schöpfen. Auch für die Bereitstellung und Erläuterung seiner Simulationsprogramme gilt ihm mein herzlicher Dank.
Den beiden Diplomanden (mittlerweile Doktoranden) Marthe Kaufholz und Philipp Schroth möchte ich für ihre wichtigen Arbeiten in verwandten Themengebieten danken. Durch diese Unterstützung konnten breitere Themengebiete abgedeckt werden und die Arbeiten konnten sich gegenseitig befruchten.
Herrn Prof. Dr. Daniel Schaadt und seiner Arbeitsgruppe am Zentrum für Funktionale Nanostrukturen (CFN, KIT), allen voran Dr. Dongzhi Hu, danke ich für die intensive Zusammenarbeit. Die Röntgenmethoden dieser Arbeit konnten sehr zielgerichtet auf ihre Proben und wissenschaftlichen Fragestellungen angewandt werden. Diese Zusammenarbeit machte schon nach kurzer Zeit eine erste gemeinsame Publikation möglich.
Auch unseren Kooperationspartnern am Institut für technische Physik (Universität Würzburg), besonders Herrn Dr. Sven Höfling und Herrn Dr. Thomas Schlereth, möchte ich für die Probenserie und ihr Engagement danken.
Mein Dank gilt zudem Herrn Dr. Taras Slobodskky für seine Arbeit bei der Entwicklung der in-situ MBE Kammer, aus der die jüngsten Ergebnisse stammen.
Herzlich bedanken möchte ich mich auch bei den Strahlrohrwissenschaftlern Herrn Dr. Gernot Buth und Herrn Dr. Stephen Doyle an ANKA in Karlsruhe sowie den Strahlrohrwissenschaftlern und ihren Arbeitsgruppen an den ESRF Strahlrohren ID10B und ID01.
Meinen Kollegen Dr. Edwin Fohtung, Dr. Andrey Minkevich und Martin Köhl danke ich für ihre Hilfe und ihre guten Ideen bei der Datenauswertung und dem Lektorat. Auch allen anderen Kolleginnen und Kollegen danke ich für die kreative und freundschaftliche Atmosphäre.

Ganz besonders möchte ich mich bei meinen Eltern für die bedingungslose Unterstützung während meiner Ausbildung und Promotion bedanken.

Contents

1 Introduction and Aims of the Thesis

1.1 X-Ray Characterization of Quantum Dots

Nanoscience is one of the most important and most promising sources of technological innovation. According to the "Bundesministerium für Bildung und Forschung" (BMBF), nanotechnology has the potential to contribute essentially to the solution of major challenges to society such as energy supply and health care (26).
Photonic semiconductor nanostructures are particularly important nano materials. Their outstanding optoelectronic properties can be used for example in efficient solar cells, laser devices for medical applications or energy saving lightening systems (25, 37, 47, 59, 85). In semiconductor technology a stepwise rapprochement towards the nano scale was seen. Driven by the desire to make use of the *quantum confinement effect*, first thin layers, later wires and finally dots were produced in oder to limit the electron movement to 2-, than 1- and finally 0-dimensions (10, 11, 12). Due to the resulting quantum confinement effect these nanosized dots are typically called quantum dots.

Besides production technologies robust characterization methods for quantum dots are needed since the knowledge about their physical properties and parameters is essential to understand the later device performance and the important relation with the production process.
In order to "image" quantum dots a resolution far better than the resolution of visible light (several hundred nm), given by Abbey's equation that limits the resolution to a value of approximately half of the wavelength, is needed. This means that either the Abbey limit has to be overcome (e.g. by the use of near field scanning optical microscopy or mechanical methods like atomic force microscopy (AFM) or, alternatively, very small wavelengths must be used (e.g. electron beam or X-ray techniques).
An optimal characterization requires a complementary mix of different methods. In case of light emitting semiconductor quantum dots the outer morphology (shape and

size) is often imaged by AFM or scanning electron microscopy (SEM). The inner structure (internal distribution of chemical composition and strain) can be accessed by x-ray diffraction techniques (6, 7, 8, 9, 43, 51, 89) or transmission electron microscopy (TEM) (42, 61). Photo luminescence (PL) measurements are often used as first evaluation of the later device performance.
While the local methods (AFM, STM, etc.) today directly deliver real space images in very high quality and resolution (2), the X-ray diffraction techniques generate measurement data, usually given in reciprocal space, and the analysis procedures of the reciprocal space data is still far from a robust routine and requires computational effort and expert knowledge. The recent trend towards in-situ and real time measurements (15, 70, 71, 99) however further strengthens the need of x-ray methods since they are in-situ applicable.

1.2 Aims of the Thesis

The thesis has two principal aims: the development and the application of in-situ suited characterization methods for morphology, strain, chemical composition and positional ordering of semiconductor nanostructures.
In the METHOD DEVELOPMENT part a new x-ray based nanotomography method that provides real space images of quantum dots showing the internal distribution of strain and chemical composition has to be developed. The method must be robust, easy to handle and in-situ applicable. In the past the dream to provide such a nanotomography method has led to two approaches:
1. Coherent diffraction imaging approaches (CDI) (22, 40, 46, 50, 51, 53, 64, 76, 103, 104) exploit suitable constraints based on a priori knowledge and apply automatized algorithms to directly transfer reciprocal space data into real space images. Even through this approach has recently been successfully extended to the technologically relevant case of strongly strained semiconductor nanostructures (52), it is yet far behind a robust routine method for broad applications. The need to measure very large and complete reciprocal space maps results in very long measurement time, which makes it unsuited to follow fast evolving processes in real time.
2. The so-called iso strain scattering model (ISS) (35, 39, 48, 87) introduces a

number of approximations and simplifications by focusing on the most important structure elements which are directly extractable from *key* features in the measured reciprocal space maps. As it is, the model suffers from increasing inaccuracy for decreasing size of the investigated dots and it is not applicable in case of the technologically relevant, and thus small quantum dots, that are measured in this thesis. That happens, since an essential part of "key features", addressed by the ISS-model to the dot, is not generated by the quantum dots but rather by substrate regions outside the dot.
The principle "as simple as possible, as precise as necessary" is however strongly appealing, especially for the robust use and application to large sample series in technological studies and in case of in-situ experiments. The general idea of the iso strain scattering concept can (and should) be kept, but a correct interpretation of the key features needs a more general model that includes all parts of the sample and thus the contribution from the substrate. The development of such an holistic iso strain model (here referred to as "HISS" model) will be part of this thesis. Based on this HISS model, a direct analysis that provides real space images of the distribution of strain and chemical composition is developed. The in-situ applicability of the new developed method is experimentally demonstrated.

In the section on Quantum dot characterization, a study which relates quantum dot properties to growth parameters and device performance is performed. The characterization method based on the HISS model, that is developed in the first part of this thesis will play an essential role.
The leitmotif for this study is to investigate the redistribution of material driven by the principle of minimization of the elastic-("strain-") energy in the system. The most prominent effect of the material redistribution is the growth of the dots itself. Similar to rain drops on the window, a 3D-agglomeration of material is energetically preferable to a thin 2D-layer. While in a thin layer the deposited material is intensively strained to fulfill the epitaxy condition, a dot allows effective strain relaxation at the top. The details of the dot growth such as, size, shape, facets, ordering (82) and the remaining strain distribution is of interest in this study. All features that contribute to the minimization of elastic energy can be tailored by the growth conditions and determine the later device performance. The growth conditions and processing parameters will be classified according to the question in how far they accelerate or slow down the strain relaxation by ma-

terial redistribution. The conditions are "close the thermodynamic equilibrium" if they allow for material distribution and strain relaxation, e.g. by high growth temperatures, slow growth speed or growth interruptions, post growth annealing or the use of high mobility materials. In the opposite case the conditions are "far from thermodynamical equilibrium".
Two concrete growth- or process- conditions should be investigated in detail. The first is a post growth annealing treatment. The effect of post growth annealing on morphology, strain and ordering of quantum dots should be investigated. For this purpose two InGaAs quantum dot samples have to be measured. Both samples were grown on GaAs(001) substrate under identical conditions away from thermodynamical equilibrium. After growth, one sample was taken out of the growth chamber, the other one was post growth annealed. By comparison of the two samples, the effect on size, shape and positional ordering of this post growth annealing treatment should be studied. AFM and x-ray scattering methods are therefore applied. Grazing incidence small angle scattering (GISAXS) and AFM should be used to determine the shape and to measure the positional ordering before and after annealing. Grazing incidence diffraction (GID) measurements should contribute to the interpretation of positional correlation as strain driven phenomenon.
The aim of the second study, is the investigation of the effect of chemical composition. For this purpose a series of three $Al_xGa_{0.4-x}In_{0,6}$ QD samples grown on GaAs(001) with varying AL concentration (x = 0, 0.08 and 0.19) was used. The reason for replacing Gallium by Aluminum is the different surface mobility. Aluminum is less mobile on the GaAs surface and might therefore have a restraining effect on the QD growth, possibly similar to conditions "far from thermodynamical equilibrium". The aim of this study is to investigate the effect of chemical composition on size, shape, ordering, but also on internal material distribution and strain. For this purpose the new analysis method, based on the HISS model, and conventional methods should be used. From these results, the relation between the nominal Al concentration, the internal distribution of chemical composition and strain and, finally, the emission wavelength should be established.

2 Background in Methods and Theory

2.1 Description of the Scattering Process

The discovery of x-ray diffraction in 1912 by Max von Laue, Walter Friedrich and Paul Knipping initialized a capacious development of diffraction theory. Together with Max von Laue, also Paul Peter Ewald (Ewald'sphere), William Henry and William Lawrence Bragg (Bragg equation) have to be mentioned among the pioneers in the field.
Nowadays extended theoretical work is available and the difficulty a "diffractionist" has to face can be phrased as "when to use what". The principle desire is to have a theory that is as simple as possible, but as precise as necessary. Two commonly used theoretical approaches are the kinematical theory (4, 16, 29, 33), that is based on the assumption of one single scattering process, and the dynamical theory (3, 4, 65, 98), that considers the possibility of multiple scattering (see below for details). Furthermore there are mixed forms, like the distorted wave born approximation (DWBA), which is introduced later in this thesis. The kinematical theory is attractive because of its extremely convenient use. If it is combined with the far-field (Fraunhofer) approximation the scattering amplitude is identified as Fourier transformation (FT) of the electron density of the scattering object. In that way, a very elegant concept to display scattering maps (the reciprocal space) and a short mathematical formalism (FT) for quick and easy forward calculation (from the sample to its scattering amplitude) and backward calculation (from the scattering amplitude to the sample) is on hand. However, the well known challenge, that only the scattered intensity, which is the absolute square of the complex scattering amplitude, can be experimentally measured whereby the phase information is lost remains (phase problem of scattering).
Since kinematical theory assumes weak interaction between the radiation and the scattering object, the application to nanostructures seems absolutely appealing. Grazing incidence diffraction geometries (GID and GISAXS), that are used in this thesis, however, aggravate effects that are neglected in kinematical theory such

as total external reflection and multiple scattering. Those effects are described in numerous theoretical work (6, 8, 29, 94, 94) and considered in this thesis.

The methodical goal of this thesis requires to find an analysis procedure that profits from (kinematical) simplicity, overcomes the phase problem of scattering and accounts for as much dynamical effects as necessary. To reach this goal, a reductionist philosophy is followed. The information that is extracted from the scattering maps is reduced to a few key parameters of the dot. These key parameters can be accessed by key features that they generate in the scattering map. The mathematical relation between the key parameters in real space and the key features in reciprocal space is very convenient and, as it will be shown in this thesis, independent of the choice of theory (kinematical or dynamical). The next chapters will demonstrate that many changes take place if multiple scattering effects or refraction corrections are included in the simulation, but the relation between the key features in reciprocal space and key parameters in real space always remains valid which makes the procedure extremely robust.
Of course, these key parameters do not deliver a complete picture of the dot, but this complete picture is obtained if the key parameters are used as constraint for standard finite element modeling (FEM).

In the past, the idea to extract key parameters in real space from key features in reciprocal space was realized within the iso strain scattering concept (35, 39, 44, 45, 48, 87). Besides assumptions and approximations concerning the scattering behavior this concept also contains assumptions and approximations concerning the scattering object itself (iso strain area model). In chapter 3 these assumptions will be critically tested and probed in detail. The results will lead to a new model, the *holistic iso strain model* (chapter 3). The necessary basics, i.e. ,the kinematical theory, selected dynamical effects and the conventional iso strain scattering concept, are sketched on the following pages.
The deviations are done following ref. (29). The starting point of the derivation are Maxwell's equations in matter

$$\nabla \mathbf{D} = \rho_f \tag{2.1}$$

$$\nabla \mathbf{B} = 0 \tag{2.2}$$

$$\nabla \times \mathbf{E} = -\frac{\partial \mathbf{B}}{\partial t} \tag{2.3}$$

$$\nabla \times \mathbf{H} = \frac{\partial \mathbf{D}}{\partial t} + \mathbf{j}_f \tag{2.4}$$

with

$$\mathbf{D} = \epsilon_0 \mathbf{E} + \mathbf{P} \tag{2.5}$$

and

$$\mathbf{B} = \mu_0 \left(\mathbf{H} + \mathbf{M}\right) \tag{2.6}$$

The aim on the next pages is the derivation of the scalar wave equation 2.18 from Maxwell's equations. the first step is the application of $\nabla\times$ to equation 2.3:

$$\nabla \times (\nabla \times \mathbf{E}) = \nabla \times \left(-\frac{\partial}{\partial t}\mathbf{B}\right) \tag{2.7}$$

With $\mathbf{a} \times (\mathbf{b} \times \mathbf{c}) = \mathbf{b}(\mathbf{ac}) - \mathbf{c}(\mathbf{ab})$ one has

$$\nabla(\nabla \mathbf{E}) - \Delta \mathbf{E} = -\frac{\partial}{\partial t} \nabla \times \mathbf{B} \tag{2.8}$$

In the following the response of the material in the external field is assumed to be linear and isotropic. Furthermore the material is assumed to be non conducting ($\mathbf{j}_f = 0$) and non magnetic ($\mu(\mathbf{r}) = 1$). Equation 2.5 and 2.6 reduce to

$$\mathbf{D} = \epsilon_0 \epsilon(\mathbf{r}) \mathbf{E} \tag{2.9}$$

and

$$\mathbf{B} = \mu_0 \mathbf{H}. \tag{2.10}$$

Equation 2.4 can be written as

$$\nabla \times \mathbf{B} = \mu_0 \epsilon_0 \epsilon(\mathbf{r}) \frac{\partial}{\partial t} \mathbf{E}. \tag{2.11}$$

Inserting 2.11 in 2.8 with leads to:

$$\nabla(\nabla \mathbf{E}) - \Delta \mathbf{E} = -\mu_0 \epsilon_0 \epsilon(\mathbf{r}) \left(\frac{\partial}{\partial t}\right)^2 \mathbf{E} \tag{2.12}$$

or with $c_0 = \frac{1}{\sqrt{\mu_0 \epsilon_0}}$

$$\Delta \mathbf{E} = \nabla(\nabla \mathbf{E}) + \frac{\epsilon(\mathbf{r})}{c_0^2} \left(\frac{\partial}{\partial t}\right)^2 \mathbf{E} \tag{2.13}$$

If there is no free charge $\rho_f = 0$, $\epsilon(\mathbf{r}) \approx 1$ follows and one has $\nabla\mathbf{E} = 0$. Equation 2.13 reduces to the wave equation in vacuum

$$\Delta\mathbf{E} = \frac{1}{c_0^2}\left(\frac{\partial}{\partial t}\right)^2 \mathbf{E} \tag{2.14}$$

which for $\mathbf{E}(\mathbf{r},t) = \mathbf{E}_0 e^{i(\mathbf{kr}-\omega t)}$ delivers the vacuum dispersion relation

$$k^2 = \frac{\omega^2}{c_0^2} \tag{2.15}$$

Inserting 2.15 in 2.13 and using the same Ansatz as above delivers

$$\Delta\mathbf{E} = \nabla(\nabla\mathbf{E}) - \epsilon(\mathbf{r})K^2\mathbf{E} \tag{2.16}$$

with the relation $\epsilon(\mathbf{r}) = 1 + \chi(\mathbf{r})$ for the dielectric function one obtains

$$\left(\Delta + K^2\right)\mathbf{E} = \nabla(\nabla\mathbf{E}) - K^2\chi(\mathbf{r})\mathbf{E} \tag{2.17}$$

The term $\widehat{V}(\mathbf{r}) = \texttt{graddiv} - K^2\chi(\mathbf{r})$ is now identified as the operator of the scattering potential and one can finally write

$$\left(\Delta + K^2\right)\mathbf{E}(\mathbf{r}) = \widehat{V}(\mathbf{r})\mathbf{E}(\mathbf{r}) \tag{2.18}$$

This wave equation has to be solved. For this purpose, the Green's function concept will be applied according to (29). The Green function is defined as solution for a delta distribution as inhomogeneity of the wave equation

$$\left(\Delta + K^2\right)\mathbf{G}_0(\mathbf{r}-\mathbf{r}') = \delta^3(\mathbf{r}-\mathbf{r}') \tag{2.19}$$

The final solution of 2.18 can be written in the quantum mechanic notations with help of Green's function

$$E(\mathbf{r}) = E_i(\mathbf{r}) + \int d^3(\mathbf{r}')G_0(\mathbf{r}-\mathbf{r}')\widehat{\mathbf{V}}(\mathbf{r}')E(\mathbf{r}') \tag{2.20}$$

or in bra-ket notation

$$\mid E\rangle = \mid E_i\rangle + \widehat{\mathbf{G}}_\mathbf{0}\widehat{\mathbf{V}} \mid E\rangle \tag{2.21}$$

where $\mid E_i\rangle$ denotes the incident wave. It should be mentioned that there is an analogy between the concept of the Green's function and the procedure in section 2.1.1. In kinematical theory the electron is considered as a point scatterer. The scattering strength of an electron is not infinite, but expressed with the classical electron radius r_{el}. Its scattering solution is described by the Thomson formula (see equaution 2.28). The similarity between the Thomson scattering formula and the solution of 2.19 for the Green function

$$G(\mathbf{r}-\mathbf{r}') = -\frac{1}{4\pi}\frac{e^{iK|\mathbf{r}-\mathbf{r}'|}}{|\mathbf{r}-\mathbf{r}'|} \tag{2.22}$$

is visible. Also the later procedure is similar in kinematical theory and in case of using Green's concept. In both cases the solution for the total scattering response is obtained by coherent addition of the responses to delta like distortions (Green's function), respectively the responses of single electrons (Thomson scattering).
A look at equation 2.21 shows a problem. The term on the right hand side, which gives the solution for the total wave $\mid E_i\rangle$ contains this solution itself. One can express the problem by using a scattering operator, that acts on the incident wave (see (29) or (17))

$$E(\mathbf{r}) = E_i(\mathbf{r}) + \int d^3(\mathbf{r}')G_0(\mathbf{r}-\mathbf{r}')\widehat{\mathbf{T}}(\mathbf{r}')E_i(\mathbf{r}') \tag{2.23}$$

or in bra-ket notation

$$\mid E\rangle = \mid E_i\rangle + \widehat{\mathbf{G}}_\mathbf{0}\widehat{\mathbf{T}} \mid E_i\rangle \tag{2.24}$$

The scattering operator is now expressed as infinite sum with the scattering potential

$$\widehat{\mathbf{T}} = \widehat{\mathbf{V}} + \widehat{\mathbf{V}}\widehat{\mathbf{G}}_0\widehat{\mathbf{V}} + \widehat{\mathbf{V}}\widehat{\mathbf{G}}_0\widehat{\mathbf{V}}\widehat{\mathbf{G}}_0\widehat{\mathbf{V}} + ... \tag{2.25}$$

Principally the integral form of the wave equation 2.20 and 2.23 could be solved by continuing the successive iterations. However, it can be shown easily that the series of successive iterations converges very slowly, and moreover, the expression for higher iterations of the wavefield are extremely complicated (29). At this point further considerations concerning the scattering object are helpful. Two special cases are discussed. The first case is the scattering from a very large, perfect crystal. Instead of using the successive iterations, the differential wave equation 2.18 is solved. For this purpose one can make use of the perfect periodicity of the

sample by writing the solution of the wave equation in the form of a Bloch wave. This is done in dynamical theory and describes the scattering of large perfect crystals.
The very small nano sized quantum dots in this thesis, however, represent another case. They are far from the assumption of very large perfect crystals. The dots are not larger than a couple of atomic layers. Furthermore, strain and strain relaxation disturbs the "perfect" periodicity. However, nano objects do not dramatically disturb the incident wave. Therefore it is possible to start from a kinematical approach and later correct the result by including specific dynamical effects within the Distorted Wave Born Approximation (DWBA).

2.1.1 Kinematical Theory

The general kinematical diffraction theory is described in many textbooks (4, 16, 29, 33). Its fundamental essence is the assumption of one single scattering act (equation 2.26). This means that after being scattered by one electron the x-ray photon cannot be scattered by another electron again (29). The scattering operator is approximated by the first term of equation 2.25.

$$\widehat{\mathbf{T}} \approx \widehat{\mathbf{V}} \tag{2.26}$$

The derivation of the kinematical theory on the next pages is systematically build up. Starting point is the scattering of one electron. Similar to the scattering response to a delta like distortion (Green function equation 2.22), the scattering response of one point scatterer, i.e., the electron, is considered as starting point. Coherent summation of the scattering of all electrons in one atom leads to the scattering amplitude of the atom, called atomic form factor. The coherent summation of the atomic form factors of all atoms in a unit cell leads to the structure factor. Finally the coherent summation of the structure factors of an infinite number of unit cells leads to the (theoretical) scattering of an infinite crystal. In order to obtain the scattering of an object the *shape function* has to be introduced. It "cuts" a certain area (later called "iso strain area") out of the infinite crystal which in Fourier space becomes physically evident as shape scattering, for example as besselrings (see below).
This gradual *coherent* adding to complexity can be compared to the concept of the Green function. The response of the system is obtained by adding the responses of delta like distortions (electrons). Finally, the fundamental statement

of kinematical theory is obtained. If combined with the far-field (Fraunhofer-) approximation, the scattering amplitude of an object is the FT of its electron density and, thus, represents tho object in reciprocal space.
Before starting with mathematical formalism, all assumptions are listed. In chapter 3, this list is discussed in detail, tested and evaluated step by step.

Assumptions of kinematical approximation:

1. Only one single scattering act; no multiple scattering
2. Elastic scattering; the modulus of the wave vector is always kept the same
3. Every electron inside the sample "feels" the undisturbed primary incident wave
4. Interaction of X-rays with electrons in vacuum; refraction index n=1 everywhere; no refraction at the air to sample
5. The incident wave is plane and monochromatic; perfectly sharp wavelength selection, no divergence of the incident beam **The far field (Fraunhofer-) approximation:**
6. The distance between sample and detector is large compared to the dimensions of the coherent scattering object

Scattering from the Electron: Thomson Scattering

The starting point of the kinematical approach is the scattering by one scattering center which is an electron. The monochromatic and plane incident wave (red lines in figure 2.1):

$$\mathbf{E_0}(\mathbf{r}, t) = \widehat{\epsilon} E_0 e^{i(\mathbf{k_0 r} - \omega t)} \tag{2.27}$$

is scattered by one single electron. The scattered wave amplitude E_s is expressed with the incident wave by the Thomson scattering formula

$$E_s(\mathbf{r}, t) = -E_0 \frac{r_{el}}{|\mathbf{r} - \mathbf{r'}|} C e^{i(\mathbf{k_0 r'} - \omega t)} e^{ik|\mathbf{r} - \mathbf{r'}|)} \tag{2.28}$$

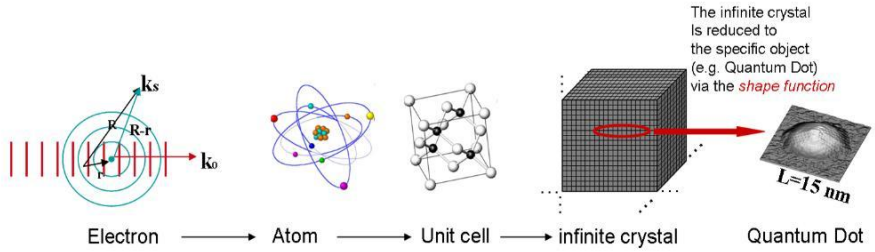

Figure 2.1: Gradually adding to complexity. Starting from the scattering of one single atom (Thomson scattering) the mathematical description of the scattering of an Atom unit cell and infinite crystal is achieved by step by step coherent summation. The scattering of a specific object is calculated by reducing the infinite crystal with its shape function (see equation 2.36).

The scattering response from the electron is a spherical wave (Huygens' Principle). The amplitude of the scattered wave corresponds to the amplitude of the incident wave multiplied by the "scattering length" r_{el} of the electron and the direction dependent polarization factor C (see figure 2.2). The absolute value of the scattered wave vector modulus $k = |\mathbf{k_o}|$ is the same as before the scattering process (elastic scattering). The phase obtains an additional term corresponding the phase evolution during the travel from the sample to the detector (retardation traveling along $|\mathbf{R} - \mathbf{r}|$, see figure 2.1). Furthermore a minus in front of the term indicates an additional 180° phase shift. This phase shift refers to a refractive index of the material smaller than unity and in so far the minus sign is a lookahead to later interpretation, since until now n=1 was assumed (see (33)page 62).

The polarization factor C corresponds to

$$C = \begin{cases} 1 & \text{in case of } \pi\text{-polarization,} \\ cos(2\theta) & \text{in case of } \sigma\text{-polarization.} \end{cases}$$

Scattering of the Atom far from Resonances - the Atomic Form Factor

In the following the wave field scattered by one atom is calculated by coherent summation of the scattering responses of all Thomson scatterers (electrons) inside the atom. The positions of the electrons are distributed statistically according to the quantum mechanical charge density $\rho(\mathbf{r})$. The time dependence, that is

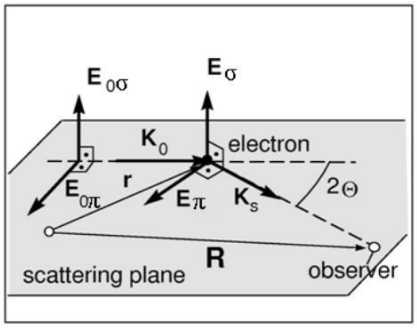

Figure 2.2: Dependence of the polarization factor C on the scattering angle and the polarization (π- or σ-) of the incident wave. source: (29)

present in equation 2.28, was suppressed in equation 2.29, since the integration time per measurement step is very long compared to the high x-ray oscillation frequencies. It should be recalled that the x-ray detectors will not record the scattering amplitude as a complex number but the scattered intensity $I_s = |E_s(\mathbf{Q})|^2$ which is the absolute square of the scattering amplitude and thus a real number (phase problem).

$$E_s(\mathbf{r}) = -E_0 C r_{el} \int_{V_{atom}} \frac{\rho(\mathbf{r}')}{|\mathbf{r}-\mathbf{r}'|} e^{i\mathbf{k}_o\mathbf{r}'} e^{ik_o|\mathbf{r}-\mathbf{r}'|} d^3r' \tag{2.29}$$

To further simplify this term, the Fraunhofer (farfield-) approximation

$$k_o\,|\mathbf{r}-\mathbf{r}'| \;\approx\; k_0 r - \mathbf{k}_s\mathbf{r}' \tag{2.30}$$

with

$$\mathbf{k}_s = k_0 \frac{\mathbf{r}}{r} \tag{2.31}$$

is applied and one obtains

$$\begin{aligned} E_s(\mathbf{r}) &\approx -E_0 C r_{el} \tfrac{e^{ik_0 r}}{r} \textstyle\int_{V_{atom}} d^3r' \rho(\mathbf{r}') e^{-i(\mathbf{k}_s-\mathbf{k}_0)\mathbf{r}'} \\ &= Const \cdot \textstyle\int_{V_{atom}} d^3r' \rho(\mathbf{r}') e^{-i\mathbf{Q}\mathbf{r}'} \\ &= Const \cdot f_i(\mathbf{Q}) \end{aligned} \tag{2.32}$$

The last expression contains two interim goals. The difference between the incoming and the scattered wave vector (momentum transfer) was defined as the scattering vector $\mathbf{Q} = \mathbf{k_s} - \mathbf{k_0}$. Thus the combination of kinematical theory and

Fraunhofer approximation delivered the important measurement coordinate **Q**. The Fourier integral after the constant factor in 2.32 expresses the scattering response of one atom. It is called atomic form factor and is listed in the international tables of crystallography for the different elements.
The second goal during the derivation of kinematical theory already appears since the mathematical expression of the atomic form factor (integral in the second line in equation 2.32) corresponds to the FT of the electron density. Generalizing this result to any electron density delivers the most important issue of kinematical theory: In the far field (Fraunhofer approx.) the scattering amplitude of an object is proportional to the FT of this electron density $\rho(\mathbf{r})$. The relation will allow to transform from real or **r**-space to reciprocal or **Q**-space by forward and invers FT. It should be mentioned again that detectable is not the scattering amplitude but the intensity which is $I \propto |E|^2$ and has "lost" the phase term (phase problem).

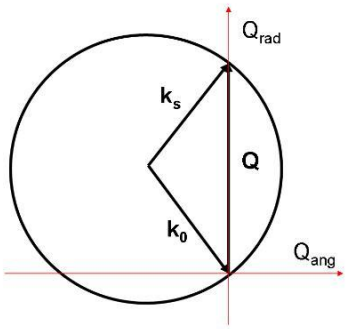

Figure 2.3: The incident wave vector $\mathbf{k}_o$ defines the *Ewald sphere*. In case of elastic scattering ($|\mathbf{k}_0| = |\mathbf{k}_s|$) the scattered wave vector ends here. The difference $\mathbf{k}_s - \mathbf{k}_0 = \mathbf{Q}$ defines the measurement coordinate of the scattering experiment. The illustration depicts the special case of a symmetrical diffraction geometry.

Scattering from the Unit Cell - The Structure Factor

In this thesis the scattering around the Bragg peaks is of high interest since it contains the footprint of the Quantum dots. The absolute Bragg peaks position or the peak intensity is not used since it is generated by the substrate, and the substrate unit cell is anyway well known. Nevertheless it is important to consider the scattering strength of different Bragg peaks in order to choose the one around which the reciprocal space should be measured. To obtain the scattering of one

complete unit cell the process is continued: Coherent adding of the atomic form factors of all atoms inside one unit cell delivers the scattering response of the unit cell:

$$F(\mathbf{Q}) = \sum_{j=1}^{S} f_j(\mathbf{Q}) e^{-i\mathbf{Q}\mathbf{r}'_j} \tag{2.33}$$

When the scattered wave fields of all electrons were coherently added up to calculate the scattering of the atom, the electron positions were given by the quantum mechanical density function and the summation was done within an integral. The atom positions in the unit cell r'_j are discrete. Hence, integration reduces to discrete summation. The result is the scattering from the unit cell, the so called structure factor. All materials investigated in this thesis are group III-V alloys and have zincblende structure. Thus, $F(\mathbf{Q})$ is given by

$$F(\text{h,k,l}) = \begin{cases} 4f_{III} + 4f_V & \text{in case h+k+l=4n e.g.(004),(220)} \quad \text{"strong"} \\ 4f_{III} + 4if_V & \text{in case h+k+l=4n+1 e.g. (113)} \quad \text{"medium"} \\ 4f_{III} - 4f_V & \text{in case h+k+l=4n+2 e.g. (002),(006)} \quad \text{"weak"} \\ 4f_{III} - 4if_V & \text{in case h+k+l=4n+3 e.g. (115)} \quad \text{"medium"} \end{cases} \tag{2.34}$$

From this table one can see that the (220) reflection that was selected for the GID measurements is classified "strong". The movement of the atoms around the equilibrium positions r'_j due to quantum mechanical fluctuations on the one hand and thermal movement (phonon) on the other hand leads to attenuation of the coherent x-ray scattering peaks. Thermal vibrations can be expressed by the **Debye-Waller factor**. It will be shown in chapter 3 that HISS, the special model and analysis procedure introduced in this thesis, does not depend on the absolute intensity of scattering data. The Debye-Waller factor is thus not relevant here.

The Reciprocal Space Representation of Nanostructures - Clouds around the Reciprocal Lattice Points

In case structure factors are coherently summed over an infinite crystal, the scattering condition results. The scattering condition is fulfilled in case the scattering vector corresponds to a reciprocal lattice vector (see textbooks,e.g.,).

Up to now, the scattering response of single electrons were coherently added to obtain the response of an ensemble of electrons in the atom, the atomic form factor. Coherent summing the scattering of all atoms inside a unit cell delivered the structure factor and the coherent adding the unit cell scattering of unit cells inside an infinite extended crystal delivered the reciprocal lattice. In this paragraph the infinite extended crystal will be reduced to a realistic object, e.g., an iso strain area inside a quantum dot. The electron density of an infinite, perfect crystal can be expressed by the real space (crystal) lattice with the electron density of the unit cell "pinned" to each lattice point. Mathematically this "pinning" corresponds to a convolution of the functions:

$$\rho_{inf.cryst.}(\mathbf{r}) = (\rho_{uc}(\mathbf{r}) \otimes \rho_{latt.}(\mathbf{r})) \tag{2.35}$$

To obtain a finite object (e.g. an iso strain area) the expression for the infinite crystal is multiplied with the shape function $\Omega(\mathbf{r})$:

$$\Omega(\mathbf{r}) = \begin{cases} 1 & \text{inside the sample} \\ 0 & \text{outside} \end{cases} \tag{2.36}$$

that is "carving" the object out of the infinite crystal:

$$\rho_{sample}(\mathbf{r}) = \Omega(\mathbf{r})(\rho_{uc}(\mathbf{r}) \otimes \rho_{latt.}(\mathbf{r})) \tag{2.37}$$

The FT of a product of two functions corresponds to the convolution of the FT of the single functions and vice versa. The FT of 2.37 results in:

$$\rho^{FT}_{sample}(\mathbf{Q}) = \Omega^{FT}(\mathbf{Q}) \otimes (\rho^{FT}_{uc}(\mathbf{Q}) \cdot \rho^{FT}_{latt.}(\mathbf{Q})) \tag{2.38}$$

The terms in equation 2.38 can be interpreted step by step with the help of the objects of interest in this thesis (e.g. the iso strain areas inside the Quantum dots). These objects are described by their "outer" shape and their internal crystallographic properties such as crystal lattice and unit cell. These real space features are represented in reciprocal space. The real space crystal lattice is represented in reciprocal space by the reciprocal lattice. The unit cells are represented by the "brightness" of the reciprocal lattice points via the structure factor; the "outer" shape is represented by the blurring of the reciprocal lattice points (see figure 2.4). Later, another real space property of quantum dots, the positional ordering and its reciprocal space representation will be introduced.

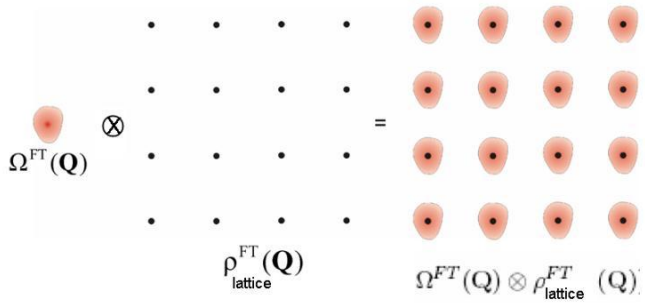

Figure 2.4: Illustration of the "blurring" of reciprocal lattice points. The FT of the shape function of an object leads to a specific distribution (orange clouds) of the scattering amplitude around the reciprocal lattice points. (taken from (5))

Summary

In summary, the main achievements of kinematical theory were illustrated in this section. The combination of kinematical theory and Fraunhofer approximation enabled the measurement coordinate $\mathbf{Q}$ for the scattering experiment and the concept of understanding the scattering amplitude as the the FT of the electron density of the sample given in reciprocal space coordinates.

2.1.2 X-Ray Reflection - Selected Dynamical Effects

This thesis focuses on the specific distribution of the scattering amplitude around the reciprocal lattice points (orange clouds in figure 2.4). To measure this distribution two diffraction geometries, i.e., GID and GISAXS are used and will be introduced in section 2.2. The mentioned techniques cannot be fully treated in the kinematical approximation. The dynamical effects, that are necessary in this context, are introduced in this section.
One challenge during the x-ray characterization of quantum dots in this thesis is the fact that the structure of interest is situated on or closely below the sample surface. For best signal to noise ratio the probing area or probing depth should be reduced to a nanometer thin surface slice of the sample. Grazing incidence diffraction techniques (GID and GISAXS) are very appealing, since the radiation and, thus, the probing area can be concentrated exactly to the surface close volume. These techniques make use of refraction and (total) external reflection at interfaces between materials with different refraction indices. In kinematical

approximation where n=1 is assumed, these effects are obviously not considered. For this reason the theory on x-ray reflection/refraction is summarized here. The reflectivity,i.e ,the Snell's law and values for the penetration depth will be given. Finally, another aspect appears. If reflection at the surface has to be considered (and diffraction is considered anyway), also combinations of reflection and diffraction have to be discussed. These multiple scattering events will be handled by using the Distorted Wave Born Approximation (DWBA).

To start with surface reflection and refraction effects one has to go back to equation 2.18 *before* the kinematical approximation was introduced:

$$\left(\Delta + K^2\right)\mathbf{E}(\mathbf{r}) = \widehat{V}(\mathbf{r})\mathbf{E}(\mathbf{r}) \tag{2.39}$$

In case no free charges exist, the scattering potential can be simplified to $\widehat{V}(\mathbf{r}) = -K^2\chi(\mathbf{r})$ leading to the Helmholtz equation:

$$\left(\Delta + K^2\right)\mathbf{E}(\mathbf{r}) = -K^2\chi(\mathbf{r})\mathbf{E}(\mathbf{r}) \tag{2.40}$$

The Ansatz of planes waves $\mathbf{E}(\mathbf{r}) = e^{i(\mathbf{kr}-\omega t)}$ delivers:

$$\mathbf{k}^2 = \sqrt{\epsilon}\mathbf{K}^2 \tag{2.41}$$

with $\chi(\mathbf{r}) = \epsilon(\mathbf{r}) - 1$, or

$$|\mathbf{k}| = n\,|\mathbf{K}| \tag{2.42}$$

with $n = \sqrt{\epsilon}$. This means that the length of the wave vector (i.e. the radius of the Ewald's sphere) compared to the vacuum wave vector depends on the refraction index n. For the semiconductor materials GaAs, InAs and AlAs n is smaller than 1 (Energy=8KeV). The radius of the Ewald's sphere in the material is thus smaller than the one in vacuum (see figure 2.5).

Boundary Conditions

According to classical electrodynamics, the tangential components of the wave vectors are continuous at every point of the interface. This can only be fulfilled, if the in-plane components of the wave vectors on both sides of the interface are the same (29).

$$\mathbf{K}_{||}^{i} = \mathbf{K}_{||}^{f} = \mathbf{k}_{||}^{t} \tag{2.43}$$

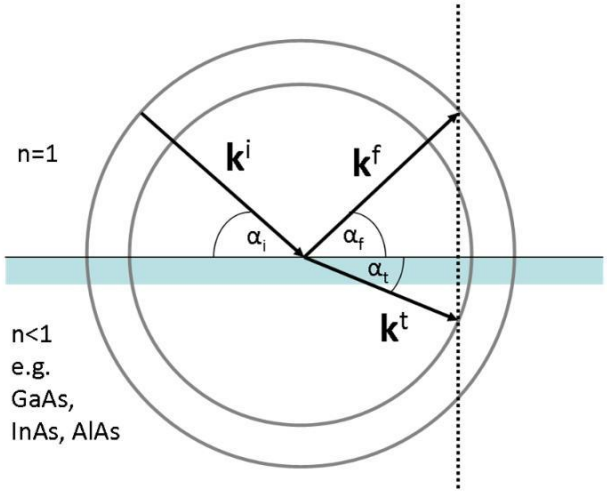

Figure 2.5: The different refraction indices in vacuum and material result in different radii of the respective Ewald's sphere. Together with the conservation of the tangential component of the wave vector (equation 2.43) the Snell's law and the critical angle of total external reflection can be derived.

From the geometry in figure 2.5 and the angles α, it follows that

$$|\mathbf{K}|\cos(\alpha_i) = |\mathbf{K}|\cos(\alpha_f) = n\,|\mathbf{K}|\cos(\alpha_t) \tag{2.44}$$

from equality of equation 2.44 one can directly derive the

Reflection Law

$$\alpha_i = \alpha_f \tag{2.45}$$

The intensity maximum that appears according to the reflection law at $\alpha_i = \alpha_f$ is called "specular reflection".

Snell's Law

The second equality in equation 2.44 leads to the Snell's refraction law

$$\frac{\cos(\alpha_i)}{\cos(\alpha_t)} = n \tag{2.46}$$

The incident angle is defined as the angle between the surface and the incident beam. (In some literature, the angle between the surface normal and the incident beam is defined as incident angel. In this case the well known sin-functions appear in equation 2.46.)

Total External Reflection and the Critical Angle

In case the incidence α_i angle is equal to or smaller than the critical angle α_c, the radiation "propagates" with $\alpha_t = 0$. From Snell's law (equation 2.46) follows for this case

$$cos(\alpha_c) = n \tag{2.47}$$

and the radiation can not (or hardly) penetrate the material. Approximating $\cos\alpha_c \approx 1 - \frac{(\alpha_c)^2}{2}$ and using $n = 1 - \delta$ with $\delta = \frac{2\pi\rho r_{el}}{k^2}$ delivers the relation between the critical angle and the average electron density.

$$\alpha_c = \lambda\sqrt{\frac{r_{el}}{\pi}\rho(\mathbf{r})} \tag{2.48}$$

material	critical angle α_C [°]
GaAs	0.308
InAs	0.318
AlAs	0.263

Table 2.1: critical angles of GaAs, InAs and AlAs at $\lambda = 1.45\mathring{A}$

The measurement of the critical angle directly gives access to the electron density of a material and vice versa. Wave fields traveling parallel to the surface inside a material can be generated by realizing the values of the incident angles around the critical angle. In that way a concentration of the wave field and, thus, the probing area to the region close to the surface is possible. In case these waves leave the material, refraction occurs again and the exit angle is α_c. This intensity peak at α_c is called Yoneda peak, or Yoneda wing. The values for the critical angels of the materials, that are investigated in this thesis, are given in table 2.1.

Penetration Depth

So far the critical angle of total external reflection was introduced. It was shown, that if a wave hades a material surface under this angle, it will continue its way parallel to the surface. According to this consideration the wave cannot penetrate in the material at all. In reality, an *evanescent* wave with very small

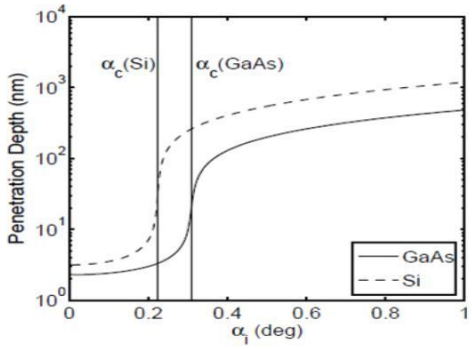

Figure 2.6: Penetration depth of the evanescent wave inside the sample in dependence of the incident angle for Silicon and GaAs. ($\lambda = 1.54$ $\mathring{A}$) Source: (58)

penetration depth (exponentially decreasing intensity below the surface) occurs. More detailed theory allows to calculate the penetration depth of the evanescent wave (19, 20). Figure 2.6 displays the dependence of the penetration depth on the incident angle. One can see that a penetration depth of only 10 nm can be realized. Such a penetration depth is perfectly adapted to measure the surface-close nano objects and, as seen later, nano-sized iso strain areas just below the surface inside the substrate.

Distorted Wave Born Approximation (DWBA)

On the previous pages refraction and reflection at the interface between two media with different refraction index n was considered. In order to make use of resulting effects, like total external reflection, grazing incidence angles in the order of the critical angles are used in the experimental geometries GID and GISAXS. This means that conditions to foster surface reflection are intentionally chosen. So far it becomes clear that reflection cannot be neglected. For the GID geometry, where diffraction and reflection are combined (see below), the consideration of multiple scattering events is inevitable and exceeds the kinematical assumption. A commonly used approach to consider multiple scattering events is the distorted wave born approximation (DWBA) (29, 36, 69). The principle idea of DWBA is to divide the scattering potential $\widehat{\mathbf{V}}(\mathbf{r})$ from equation 2.18 in two parts.

$$\widehat{\mathbf{V}}(\mathbf{r}) = \widehat{\mathbf{V}}_A(\mathbf{r}) + \widehat{\mathbf{V}}_B(\mathbf{r}) \tag{2.49}$$

In this thesis the multiple scattering processes that are considered in DWBA are combinations of diffraction and reflection. Four different "channels" take 4 possible combinations of reflection and diffraction into account (see figure 2.7). These processes are dynamical reflections at the surface of the substrate, considered by $\widehat{\mathbf{V}}_A(\mathbf{r})$, in combination with the kinematical diffraction in the quantum dots, described by $\widehat{\mathbf{V}}_B(\mathbf{r})$.
The final scattering is the coherent sum of the contributions. Since the reflections at the substrate enable a momentum transfer uniquely along the z-coordinate (see figure 2.7) one may conclude that only the $\mathbf{Q_z}$ component of the scattering amplitude changes due to the use of the different DWBA channels. The reason for this is the lateral symmetry of the reflecting surface. One might further conclude that, in case the data is anyway integrated along Q_z, the differences concerning change of the Q_z distribution can be neglected and the final 2D result, after integration, does not depend on using or not using the DWBA channels. However, this argumentation is misleading. Clearly, only the Q_z component is affected by reflections at the surface, but *interference* of the radiation which was scattered according to different channels has to be considered. This is important since interference between waves scattered according to different channels may be constructive or destructive depending on the path difference,i.e., the height above the substrate inside the dot where the radiation was diffracted. Due to the vertical strain gradient that exists inside the dot, this position dependence is automatically linked to a strain dependence. That means that interference between Born channels might darken of enlighten the reciprocal space map along coordinates that reveal strain e.g. Q_{rad} and that are not oriented along Q_z. In section 3.2 this effect is investigated mathematically and illustrated by simulations of diffraction maps with 4-channel and one-channel DWBA.

2.2 Scattering and Diffraction Geometries

Different kind of information, that should be gained by scattering or diffraction experiments, is included in different parts of the reciprocal space. As derived above, the shape of nano objects is enclosed in the blurred surrounding of the reciprocal lattice points. Depending on the area in reciprocal space, the speed and the circumstances, in which these areas should be measured, different scattering and or diffraction techniques are differentiated. In figure 2.8 an overview of the

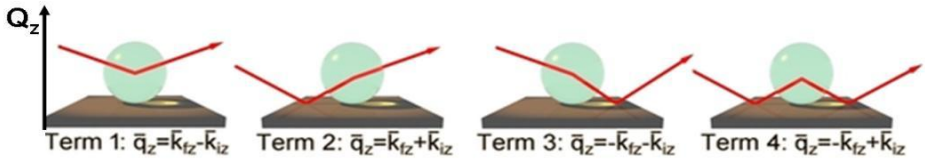

Figure 2.7: The four different channels of the distorted wave Born approximation (DWBA). The first channel corresponds to the kinematical approximation. The other three channels depict consecutive combinations of reflection and diffraction processes. In these cases the q_z component of the scattered photon changes compared to kinematical theory. Image source: (49)

most common diffraction and scattering techniques is given.
Surface sensitive grazing incidence methods access the lattice points situated in the sample surface plane (turquoise plane in figure 2.8). The (hk0) reflections (surface normal (001)) can be accessed by grazing incidence diffraction (GID). In the special case of (000), i.e. the origin of reciprocal space, the corresponding method is called grazing incidence small angle scattering (GISAXS).
In this thesis the (220) and the (000) lattice point were measured. The details for both, the measurement of (220) in GID geometry and the measurement of (000) in GISAXS, are explained in the next two paragraphs.

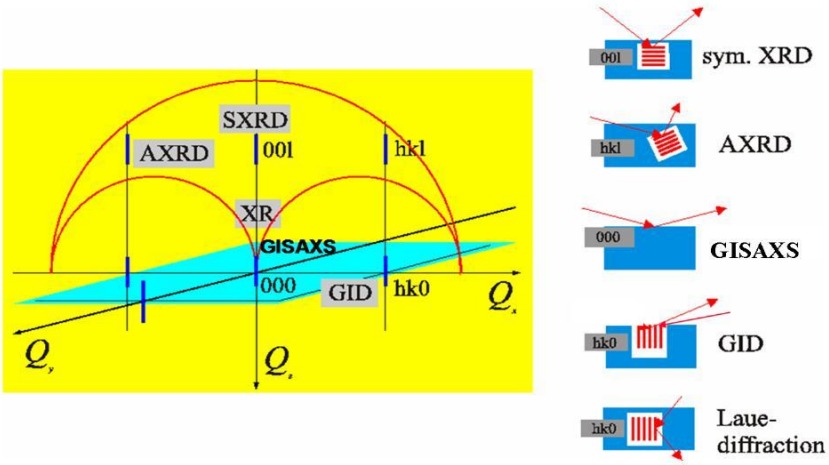

Figure 2.8: Overview on different experimental geometries. Depending on the orientation between the atomic planes corresponding to the reflection and the sample surface symmetrical (SXRD), asymmetrical (AXRD) and grazing incidence (GID) x-ray diffraction can be distinguished. Grazing incidence small angle scattering (GISAXS) is method to record the scattered intensity around the origin of reciprocal space. Source: (5).

2.2.1 Grazing Incidence Small Angle X-ray Scattering (GISAXS)

Grazing incidence small angle scattering (GISAXS) is a scattering technique that measures the reciprocal space around its origin i.e the (000) reciprocal lattice point. At the center of this reciprocal lattice point, the diffraction vector is zero ($\mathbf{Q} = 0$) and the diffraction condition is always fulfilled. This means that the FT of the shape function (see figure) of any objects under investigation is pinned to that lattice point independent of its real space crystallographic lattice parameter. Therefore, the method is sensitive to shape and morphology but not sensitive to real space lattice parameter or strain. In so far there is overlap between the outcome of GISAXS measurements and other morphology sensitive methods, like AFM for example. This creates a comfortable situation: For every kind of information that should be obtained and every measurements situation (e.g. in-situ) the most appealing method can be chosen. In this thesis, the general real space images of the outer morphology of the dots is taken from AFM and SEM measurements. For the characterization of specific and important features GISAXS measurements are used. These features are

- **side facets** visible in GISAXS through the side facet truncation rods (yellow color in 2.11),
- **positional correlation** visible in GISAXS through the correlation peaks (red colored intensity spots in 2.11)
- and **average aspect ratio** of the lateral dot extensions visible in GISAXS through the inverse average aspect ratio of the shape scattering (blue colored cloud in 2.11)

Now the mathematical description of the relation between these three QD features and their apparition in the GISAXS data will be introduced. Principally, the measurement of the (000) lattice point requires scattering angles close to zero. This motivates the term "small angle scattering". In case of free nano objects, forward scattering is possible in transmission geometry. In case the nano objects are situated on top or closely below the surface of a comparably thick substrate, a transmission geometry through the substrate is unfavorable and the special grazing incidence geometries, that are described above (total external reflection), have to be used. Figure 2.9 displays the typical grazing incidence geometry of

the GISAXS technique.

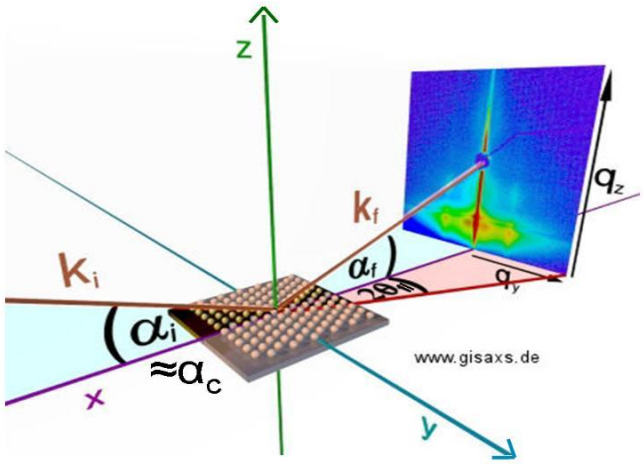

Figure 2.9: Geometry of the GISAXS set-up. The value of the grazing incident angle α_i is typically chosen around the critical angle α_c which is approximately 0.3° in case of GaAs and a wavelength of 8 KeV. The intensity along the outgoing angles α_f contains the typical features: sample horizon, yoneda wing and specular reflection. The outgoing in-plane angles 2Θ are typically between $-2°$ and $2°$. Source: (49)

Two scattering planes can be distinguished: the horizontal plane, in which lies the $2\Theta_{||}$ angle (rose color), and the coplanar plane, containing the incident and exit angles α_i and α_f (blue color). In reciprocal space q_x, q_y (in-plane) and q_z, q_x (out-of-plane) are associated with these planes.
In kinematical approximation the scattering amplitude around the reciprocal lattice point was described by the FT of the shape function of the scattering object. This approximation holds well for the in-plane, but not for the out-of-plane direction, since the refraction corrections affect the q_z component of the scattered photon and thus the out of plane intensity distribution. Due to the reflection and refraction at the surface, two intensity maxima (see figure 2.9) along q_z appear, that are not explained in kinematical theory. These are the so called Yoneda wing (106) at $\alpha_f = \alpha_c$ and the specular reflection at $\alpha_f = \alpha_i$. The two peaks would coincide if one choses the incident angle exactly equal to the critical angle.
In this thesis only specific information has to be extracted from the GISAXS maps (see above). In order to start the analysis it is very convenient to integrate the 3D intensity distribution along q_z around the position of the Yoneda level. In that way, in case of GISAXS, most specific information can be extracted from the

resulting q_x, q_y intensity map according to kinematical theory. One needs to understand the refraction and reflection theory in order to realize an advantageous scattering geometry (grazing incidence) or in order to select a suited q_z integration range (around Yoneda). For most steps of the analysis itself, the refraction and reflection corrections can again be neglected. As seen later this approach is valid only for GISAXS but not for GID. In the next three paragraphs it is step by step explained how the specific information is extracted from the GISAXS maps.

Truncation Rods

The QDs under investigation are made from crystalline material and thus tend to develop side facets rather than a round shape in order to reach an energetic minimum of the surface energy. These side facets can be very small and it is sometimes difficult to resolve the facets and their crystallographic orientation with microscopy techniques. In this case GISAXS measurements are appealing, since the facets generate a characteristic and easy to resolve feature in reciprocal space: the facet truncation rod (TR)(54, 74).
In order to introduce the TR, a thin layer of a crystalline material is considered. The surface normal of the layer is oriented along z in a standard kartesian coordinate system. The thickness of the layer is t, along x and y it is infinitively extended. The electron density inside the layer is ρ_{Layer}. Its shape function can be written

$$\Omega(x, y, z) = \Theta(z) - \Theta(z - t) \tag{2.50}$$

where

$$\Theta(z) = \begin{cases} 1 & z \geq 0 \\ 0 & z < 0 \end{cases} \tag{2.51}$$

is the heavy side function. The FT of the shape function is

$$\Omega^{FT}(\mathbf{Q}) = 4\pi^2 t \cdot sinc\left(Q_z \frac{t}{2}\right) e^{-iQ_z \frac{t}{2}} \delta(Q_{||}) \tag{2.52}$$

This means that around the reciprocal lattice points the scattering amplitude of a thin layer is concentrated in a streak (see delta function), the so called truncation rod (TR). The truncation rods are oriented along the direction of the surface normal of the layer. The intensity inside the TR is modulated according to the "sinc" function term. It is visible in equation 2.52 that the periodicity of the sinc

function is determined by the layer thickness. Very often this oscillation is used in order to measure the thickness of thin layers. In this thesis the TR's are used in order to reveal the existence and the orientation of side facets of quantum dots. The side facets of dots have a finite sizes. Nevertheless they can be compared to the infinite layer since they generate TRs in reciprocal space. Those TRs are not infinitesimal thin but they have finite thicknesses. From their orientation the orientation of the facets can be determined in analogy to the example of the infinitely extended thin layer.

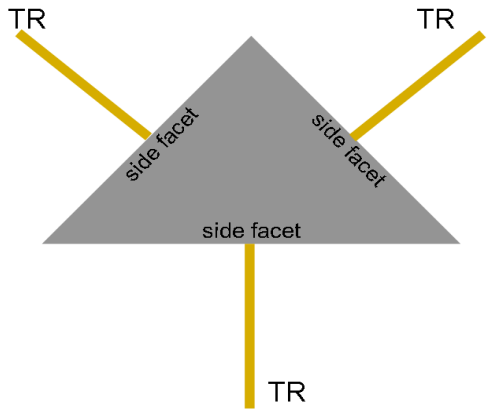

Figure 2.10: Illustration of side facet truncation rods (TR). Plane facets generate facet Truncation rods in reciprocal space. From the orientation of theses rods the orientation of the facets of the object (e.g. Quantum dot) in real space can directly be deduced.

This will be done in chapter 4 where the appearance of side facets during post growth annealing is studied. In the GISAXS data example (figure 2.11) the projection of the side facets TR is seen as yellow streaks in the center of the image.

Positional Correlation of the Dots

In chapter 2.1.1 the scattering amplitude around a reciprocal lattice point was identified as the FT of the shape function of the object under consideration. During the experiment not only one quantum dot, but a large number of dots is simultaneously illuminated. The size of the footprint on the sample (including enlargement due to the grazing incidence) is approximately 0.2 mm x 100 mm in case of GISAXS. The radiation is fully coherent only within the coherence volumes. The coherent domain, which is the area on the sample, that is coherently

illuminated, is about 100 μm^2 large. This means that during the GISAXS measurement approximately 10000 Dots are coherently illuminated. To clarify the difference between the measurement of an ensemble of dots and a single dot, two scenarios are distinguished: randomly distributed positions of the dots and correlated positions. The cases are distinguished by the correlation function $C(\mathbf{r}, \mathbf{r'})$ (29)

$$C(\mathbf{r}, \mathbf{r}') = \langle \chi_0(\mathbf{r})(\chi_0(\mathbf{r}'))^* \rangle \tag{2.53}$$

The zero-th Fourier coefficient of the polarizability χ_0 is proportional to the electron density and thus to the position of the dots. The polarizability can be expresses by the position vector of the n-th dot $\mathbf{R}_n$ and the shape function $\Omega(\mathbf{r})$ of the dot. The covariance $M(\mathbf{r} - \mathbf{r}')$ is

$$\begin{aligned} &M(\mathbf{r} - \mathbf{r}') \\ &= |\Delta\chi_0|^2 \left[\sum_{m,n} \langle \Omega(\mathbf{r} - \mathbf{R_m}) \Omega(\mathbf{r}' - \mathbf{R_n}) \rangle - \sum_{m,n} \langle \Omega(\mathbf{r} - \mathbf{R_m}) \rangle \langle \Omega(\mathbf{r}' - \mathbf{R_n}) \rangle \right] \end{aligned} \tag{2.54}$$

where $\Delta\chi_0 = \chi_0^{object} - \chi_0^{matrix/vacuum}$ is the contrast in χ_0 between the dot and its neighborhood. For the sake of simplicity it is assumed here that all dots have the same form and lie in the same plane (surface of the substrate). In the first step their positions are assumed to be random. The scattered intensity is (29)

$$I_{rand.pos} = I_i \frac{K^6}{16\pi^2 A} \left| \omega^{FT}(\mathbf{Q}) \right|^2 G_{||}(\mathbf{Q}_{||}) \tag{2.55}$$

where A is the irradiated sample surface. One can see that the scattered intensity is still proportional to the FT of the shape function $\Omega^{FT}(\mathbf{Q})$. The fact that not a single dot, but an ensemble of dots is measured just increased the scattering signal by a constant factor. Since the lateral geometrical factor $G_{||}$

$$G_{||}(\mathbf{Q}_{||}) = \left\langle \sum_{m,n} e^{-i\mathbf{Q}_{||}(\mathbf{R}_{||m} - \mathbf{R}_{||n})} \right\rangle \tag{2.56}$$

is constant in case the dots are not ordered. The intensity distribution in reciprocal space is entirely determined by the shape of a single dot. In the following the case of correlated positions of the dots is considered. Two models for the dot arrangement are discussed following the approach of (29).

Short-Range-Order Model

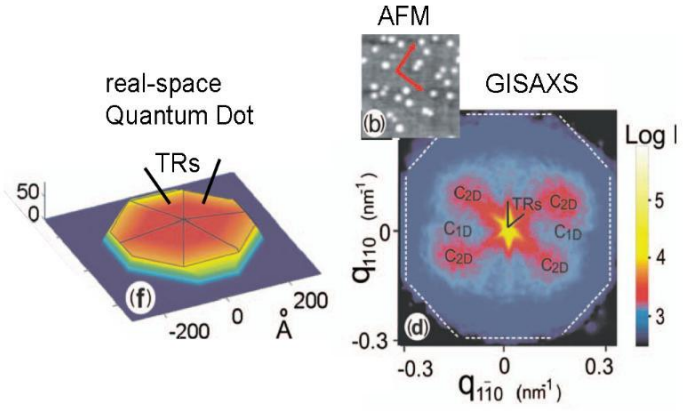

Figure 2.11: Example of an typical GISAXS image. Three main features can be identified on the scattering image (right) and related to the real space model (left): 1. the truncation rods from the facets, visible in yellow on the RSM and marked with the black lines, 2. the FT of the QD shape (blue cloud) and 3. the QD ordering (red correlation peaks). source: (75)

In this model the position of a particular dot depends only on the position of the neighboring dots. Here only the one dimensional version will be derived, a two-dimensional model can be obtained by analogous way. The lateral position of the m-th dot is X_m. The distance between a dot and its neighbor is $L_m = X_m - X_{m-1}$. If the total number of dots N is very large, the lateral geometrical factor is (16, 29, 68)

$$G_{||}(Q_{||}) = N\left[1 + 2Re\left(\frac{\eta}{1-\eta}\right)\right](1 - \delta_{Q_{||},0}) + N^2\delta_{Q_{||},0} \tag{2.57}$$

where

$$\eta = \left\langle e^{-iQ_{||}L} \right\rangle \tag{2.58}$$

is the characteristic function of the probability distribution of L. The dispersion of L depends on the order m of the gamma distribution of the distance L by $\sigma_L = \frac{\langle L \rangle}{\sqrt{m}}$. The geometrical factor now exhibits maxima in points

$$Q_{||p} \approx p\frac{2\pi}{\langle L \rangle}, p = 0, \pm 1, \pm 2, ... \tag{2.59}$$

The better ordered the dots are (i.e. the larger m), the narrower the maxima, later called correlation peaks, are. The width of the correlation peaks will be

used in order to estimate the quality of ordering. The position of the correlation peaks in reciprocal space reveals the characteristic dot to dot distance and the direction of ordering. In the GISAXS data example (figure 2.11) four correlation peaks (red colored intensity maxima labeled C_{2D}) are visible. They reveal ordering along the {100} directions.

Long-Range-Order Model

Until now short range ordering was considered. This kind of ordering happens in case neighboring dots interact with each other, while the interaction of dots that are afar from each other can be neglected. An example for this interaction might be forces between the dots that are mediated by the surrounding substrate strain.

Another type of ordering is the long-range-ordering. The introduction of this type of ordering is taken from (29), where also graphical illustrations can be found. In a one dimensional long-range-order model, a periodic ideal lattice with the period L is assumed. The dots are displaced from the lattice points by random displacements U_m. It is assumed that $\langle U_m \rangle = 0$ and $\langle U_m, U_n \rangle = \sigma^2 \delta_{mn}$, where σ is the root mean square displacement of the objects from their ideal positions. The lateral geometrical factor for N dots is (29, 105)

$$G_{||}(Q_{||}) = N(1 - D^2) + D^2 \left| \sum_{m=1}^{N} e^{-iQ_{||}Lm} \right|^2 \tag{2.60}$$

where

$$D = \left\langle e^{-iQ_{||}U} \right\rangle \equiv e^{-\sigma^2 Q_{||}^2/2}. \tag{2.61}$$

The factor D is analogous to the static Debye-Waller factor defined in Chapter 5 and its formula has been obtained assuming a normal distribution of the random displacements U_m.

The lateral geometrical factor exhibits a sequance of latzeral maxima for

$$Q_{||p} \approx p\frac{2\pi}{L}, p = 0, \pm 1, \pm 2, ... \tag{2.62}$$

In contrast to the short-range-order model, the width of the maxima is constant and independent of σ. The width of the maxima is inversely proportional to the number of dots occurring in a coherent domain (see above). In case the sample

is large and fully covered, by the dots the width of the maxima reveals the size of the coherent domain. Their height decreases with increasing σ. If the long-range-order model is valid, the integrated intensity is not directly determined by the shape of the objects. An example for long-range-ordering could be dots on a surface that shows a regular surface mesh, for example after surface reconstruction. In case the dots preferably grow in a certain point of this mesh, long range ordering might occur.

Average Aspect Ratio of the Lateral Dot Extensions

After the side facets and the positional correlation, now the average aspect ratio of the lateral dot extensions in considered. Principally this information is extractable from single dots in one AFM image, however, the mentioned aspect ratio is of enormous importance and needs to be measured with high statistical relevance, since the strain field, that is induced around the dot into the substrate, will be considered as driving force for the positional ordering. This strain field depends on the shape and its symmetry, in particular on the ratio between the lateral extensions of the dot along different directions. Therefore this ratio has to be measured with high statistical relevance, i.e. averaged from thousands of dots. In the following the formalism that will be used to extract the ratio between the lateral extensions of the dots from GISAXS data is introduced.
The Quantum dot is considered to be a stack of round shaped flat discs with different radii r and diameter D. The 2D scattering of such a disc is proportional to the square of its 2D FT

$$I(Q_{||}) \propto \left|\Omega^{FT}(Q_{||})\right|^2 \propto \left|2\pi r^2 \frac{J_1(Q_{||}r)}{Q_{||}r}\right|^2 \tag{2.63}$$

where J_1 denotes the first order Bessel function. Figure 2.12 illustrates such a quantum dot model and the corresponding scattering amplitudes.

It can be seen that the width of the central maximum and the distances between higher orders of the shape scattering are inverse proportional to the radius of the discs. Consequently from the oscillation period along $Q_{||}$ the diameter of a disc can be extracted. It was shown that, especially for grazing incidence condition, non kinematical effects such as refraction and multiple scattering affect the Q_z intensity distribution. In order to still apply kinematical theory, the intensity was integrated along Q_z around the Yoneda level and projected to the in-plane

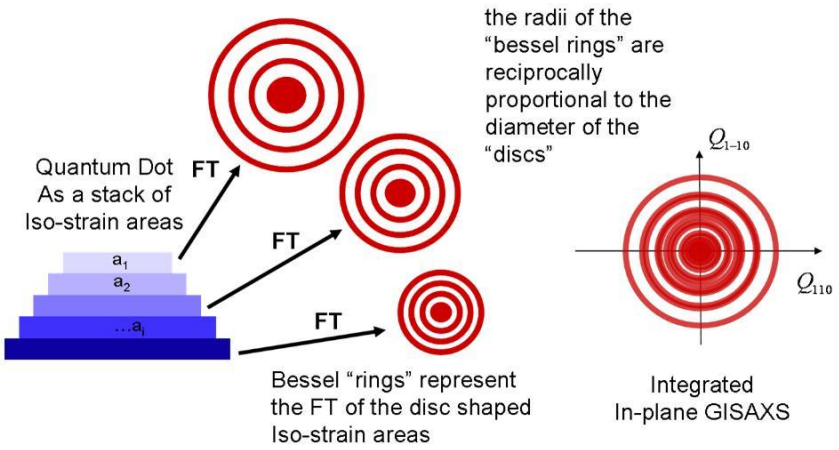

Figure 2.12: Illustration of a quantum dot model composed by a stack of discs with different diameter. The radii of the 2D FT of these disc "Bessel rings" are inversely proportional to the diameter. After integration along Q_z all "Bessel rings" overlap in the in-plane reciprocal space projection.

map. Thus non kinematical effects are faded out. Since GISAXS is not sensitive to strain, the bessel rings that are generated by different discs at different z position all overlap in the scattering map (see figure 2.12). A smooth blue cloud instead of distinct oscillations is therefore visible in the experimental GISAXS data (see figure 2.11). The absolute diameter of each disc cannot be extracted. However, in case the discs are not round, the ratio between the diameter along different directions can be extracted in a very simple way. The ratio between the average dot diameter $\frac{D_{110}}{D_{1\bar{1}0}}$ corresponds to the inverse ratio of the extensions of the blue cloud $\frac{\widetilde{D}_{1\bar{1}0}}{\widetilde{D}_{110}}$ (figure 2.11).

$$\frac{D_{110}}{D_{1\bar{1}0}} = \frac{\widetilde{D}_{1\bar{1}0}}{\widetilde{D}_{110}} \tag{2.64}$$

As described later in detail, the problem of overlapping contributions from different discs is overcome in GID, since the discs are separated by different lattice parameters. At this point the GISAXS analysis is "reduced" to the ratio of the diameter along different directions. One must recall that this information will play an essential role later in this thesis, since the asymmetry in shape might be responsible for the induction of asymmetric strain around the dot, which will be discussed later as driving force for asymmetric positional ordering.
In summary, GISAXS and AFM measurements are used in this thesis to deter-

mine the quantum dot shape. While the general shape picture is delivered from AFM, the GISAXS measurements are focused on three important dot features. These are side facets, positional dot ordering and in-plane dot symmetry (i.e., ratio between the lateral extensions along different directions). All features will play an essential role during the dot characterization in chapter 4 of this thesis.

2.2.2 Grazing Incidence Diffraction (GID)

Grazing incidence diffraction (GID) is a technique to measure the scattered intensity around in-plane reciprocal lattice points. In this thesis the (220) in-plane lattice point is selected, since it is "strong"(table 2.34) and accessible with convenient wavelengths. Similar to the GISAXS technique, GID makes use of refraction effects (see section 2.2). The experimental setup of the GID experiment (figure 2.13) is therefore similar to that of GISAXS, shown in figure 2.9. Again the sample surface is hit by the radiation under a small "grazing" angle. In opposite to GISAXS, not the small angle scattered radiation is recorded but the radiation that was Bragg diffracted by atomic planes perpendicular to the surface. The 2θ angle is not "small" but corresponds to values that are large enough to fulfill the in-plane Bragg condition.

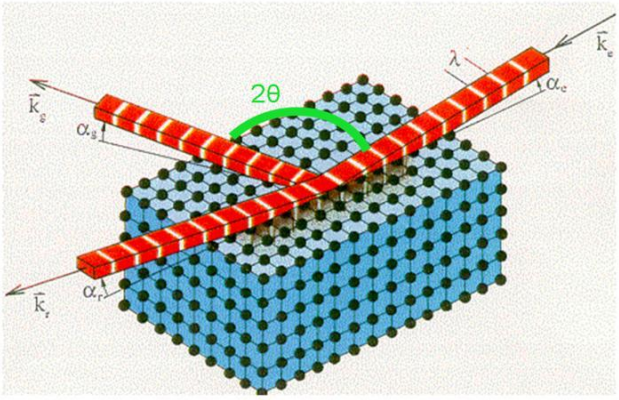

Figure 2.13: GID geometry. The incident, the forward scattered and the diffracted beam are visible. While GISAXS measures the forward scattered beam the GID measurement records the radiation that was Bragg diffracted. The 2θ angle is given by the Bragg law. It can be seen that in opposite to GISAXS where the scattering of all parts of the dot widely overlaps, a separation according to the lattice parameter differences occurs. source: (18)

During the introduction of the kinematical theory in section 2.1.1, it was shown that the FT of the shape function is "pinned" to every reciprocal lattice point (figure 2.4). The exact position of the reciprocal lattice points depends on the real space lattice parameter. The fact, that materials with different "natural" lattice parameters are brought together in epitaxy, indicates the presence of different lattice parameters in the sample. Therefore, the position of the (220) reciprocal lattice point is not clearly defined. Usually its position is given with reference to the relaxed substrate lattice parameter. The position differs for regions in the sample with other lattice parameter. In order to still evaluate the GID data according to simple considerations a second approximation in addition to the kinematical approximation, the so called iso strain scattering (ISS) concept, will be used. Since in this thesis major development is done in the area of the ISS model, a description of the principles of the ISS approximation, as it is commonly known, is given in the next paragraph. In the subsequent paragraph, the new development of a **holistic iso strain model (HISS)**, that is one of the major achievements of this thesis, is depicted.

2.3 Quantum dot scattering - the iso-strain scattering model

The iso-strain scattering concept was developed about a decade ago (35, 36, 48). It introduces a number of approximations and simplifications. The ISS concept suggested that "by identifying key features of the x-ray intensity distribution in reciprocal space, one can directly reconstruct the geometry as well as the distribution of local lattice parameter and material composition. Thus, a transformation of scattering data from quantum dots to nanometer-scale tomographic images is achieved" (35).
On the following pages the iso strain model "as it is" is described and explained. In the conventional iso strain model (35, 39, 48, 87) the dot is assumed to be a stack of laterally extended, slightly curved areas with constant lattice parameter a, the noted iso strain areas (ISAs):

$$\rho^{dot} = \sum_i \rho_i^{ISA} \tag{2.65}$$

Following kinematical theory, the scattering signal of one single ISA is proportional to the absolute square of the FT of its electron density modulo absolute

scaling:

$$I(\mathbf{Q}) \propto \left| FT\left[\rho^{ISA}(\mathbf{r})\right]\right|^2 = |S_i(\mathbf{Q})|^2 \tag{2.66}$$

The iso strain scattering model claims that the scattering of the whole dot can be approximated by the *incoherent* superposition of the scattering signals of the single ISAs.

$$I(\mathbf{Q}) \propto \left|\sum_i S_i(\mathbf{Q})\right|^2 \approx \sum_i |S_i(\mathbf{Q})|^2 \tag{2.67}$$

where $S_i(\mathbf{Q})$ is a complex number. In equation 2.67 the mixed terms are neglected.

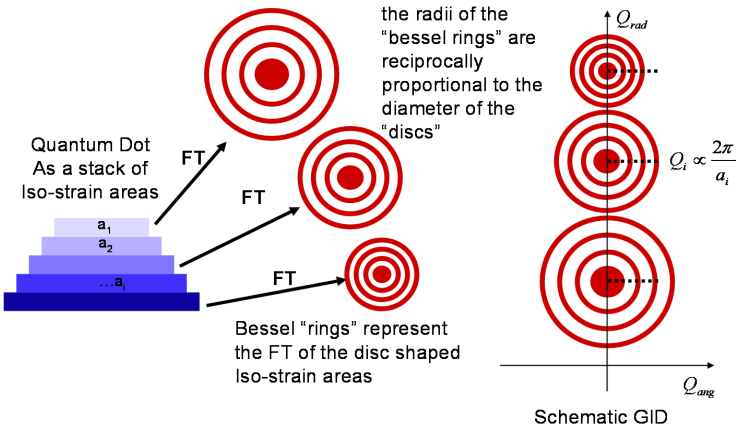

Figure 2.14: Schematic drawing of the scattering of a free standing quantum dot according to the iso-strain (ISS) model. Left side: the quantum dot is represented as stack of iso-strain areas. Each ISA has its own lateral extension D_i and its own lattice parameter a_i. The reciprocal space images is assumed to be the incoherent sum of the FT of the single ISAs. The lattice parameter defines the position in reciprocal along Q_{rad}, the radius of the Bessel rings represented also by the periodicity of the intensity oscillations along Q_{ang} defines the lateral size of the ISA.

This means that the scattering of the whole dot is assumed to be the simple sum of the scattering of the single ISAs, neglecting interference between the scattering amplitude of different ISAs. The validity and applicability of this approximation is tested later in this thesis.
In the conventional iso strain model in three analysis steps the strain, the size, and the height above the substrate is determined for the ISAs.

Extracting the Strain of an ISA from the $\left|H^i\right|$

Every ISA has its own lattice parameter a^i. Therefore, the reciprocal space contribution of different ISAs (shape scattering of the disc) is centered around a certain $\mathbf{H}^i$ position

$$\left|H^i\right| = \sqrt{h^2 + k^2 + l^2} \cdot \frac{2\pi}{a^i} \tag{2.68}$$

From this H^i value the lattice parameter inside the iso strain area i is deduced.

Extracting the size of an ISA from the Intensity oscillation along q_{ang}

The shape of the ISA generates shape scattering in reciprocal space. The shape scattering is analyzed according to the coordinate $\mathbf{q}$, which is defined by

$$\mathbf{q}^i = \mathbf{Q} - \mathbf{H}^i \tag{2.69}$$

The intensity profile along q^i_{ang} contains the shape scattering (shape oscillation) of the ISAs. The periodicity of the oscillation indicates the ISA diameter D. To extract the diameter of the ISA i, the Intensity profile is reviewed along a line that crosses Q^i_{rad} parallel to the Q_{ang} axis. The position of the first order scattering maximum q^i_{max} delivers D_i via

$$D_i = \frac{2 \cdot f}{q^i_{max}}. \tag{2.70}$$

In case of circular shaped ISAs, $f = 5.13$ is the value of the first order maximum of $(J_1(x)/x)^2$. J_1 denotes the first order Bessel function. In this way the pair $(a_i; D_i)$ is obtained for every ISA.

Extracting the ISA position above the surface - Intensity along Q_z

In this thesis the analysis of the reciprocal space data is performed on the basis of 2D intensity maps. For this purpose the measured 3D intensity is projected to the Q_{rad}, Q_{ang}-plane. The exact intensity distribution along Q_z (perpendicular to the sample) is not used for the analysis since the data is integrated along this direction. However, principally it is possible to extract the position of each ISAs (at least for those above the sample surface) by analyzing the intensity distribution along Q_z. Here, since the intensity is integrated along Q_z, it is important to understand the Q_z intensity distribution in order to choose a proper

integration ranges for the projection.
Since (220) reflections are measured the lattice vector lies parallel to the sample surface ($H_z = 0$) and one has

$$q_z = Q_z - H_z = Q_z \tag{2.71}$$

To calculate the intensity distribution along Q_z, which is perpendicular to the sample surface, dynamical terms are essential due to refraction and reflection effects at the surface. It was shown in chapter 2.1.2 that combinations of surface reflection and diffraction can be treated with a specific DWBA approximation. In the formula for the intensity distribution of an ISA, situated at z above the surface, the transmission function t is replaced by a special transmission function t^{fps} that includes the four-process scattering (fps) that is used in DWBA (see figure 2.7) (36)

$$F^z_{total}(Q_z, z, \alpha_i, \alpha_f) = F^z(Q_z) t^{fps}(\alpha_i, z) t^{fps}(\alpha_f, z) \tag{2.72}$$

with

$$t^{fps}(\alpha, z) = 1 + r(\alpha). \tag{2.73}$$

The reflectivity and transmittivity are usually given as (36)

$$r(\widehat{\alpha}) = \frac{\widehat{\alpha} - \sqrt{\widehat{\alpha}^2 - 1}}{\widehat{\alpha} + \sqrt{\widehat{\alpha}^2 - 1}} \tag{2.74}$$

and

$$t(\widehat{\alpha}) = \frac{2\widehat{\alpha}}{\widehat{\alpha} + \sqrt{\widehat{\alpha}^2 - 1}} \tag{2.75}$$

with the reduced coordinates

$$\widehat{\alpha} = \frac{\alpha}{\alpha_c} \tag{2.76}$$

and

$$\widehat{z} = k\alpha_c z \tag{2.77}$$

The Intensity distribution along Q_z after including the surface reflection is now given in two parts. In case α_f is smaller than the critical angle ($\widehat{\alpha} < 1$) one has (36)

$$I^{fps}(\widehat{\alpha}, \widehat{z}) = 2 + 2(2\widehat{\alpha}^2 - 1)\cos 2\widehat{\alpha}\widehat{z} + 4\widehat{\alpha}\sqrt{1 - \widehat{\alpha}^2}\sin 2\widehat{\alpha}\widehat{z} \tag{2.78}$$

from the maximum of that distribution the height z of the iso strain area above the surface can be determined (36)

$$z = \frac{1}{k\alpha^{max}} \arccos \frac{\alpha^{max}}{\alpha_c} \tag{2.79}$$

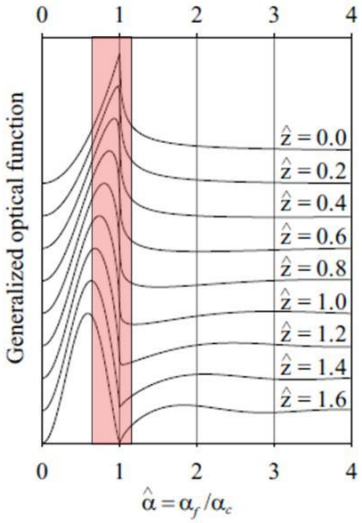

Figure 2.15: The distribution of t^{fps} along α_f is shown for ISAs situated at different $\widehat{z}$. One can see that the maximum shifts from the critical angle to lower values for larger z. Above α_c oscillations become visible for large z values, that correspond to the kinematical view. The red ares marks the typical integration range. source: (36)

The intensity distribution for $\widehat{\alpha} > 1$ is

$$I^{fps}(\widehat{\alpha}, \widehat{z}) = 1 + \frac{2\widehat{\alpha} - 1 - 2\widehat{\alpha}\sqrt{\widehat{\alpha}^2 - 1}}{2\widehat{\alpha} - 1 + 2\widehat{\alpha}\sqrt{\widehat{\alpha}^2 - 1}} + 2\frac{\widehat{\alpha} - \sqrt{\widehat{\alpha}^2 - 1}}{\widehat{\alpha} + \sqrt{\widehat{\alpha}^2 - 1}} \cos 2\widehat{z}\widehat{\alpha} \tag{2.80}$$

One can recognize the oscillation of period $2\widehat{z}$ in the formula. That is the oscillation period that one expects from kinematical theory (sinc-function). Principally it is possible to derive the $\widehat{z}$ value of every ISA from that period. As seen from the theoretical curves in figure 2.15 the intensity is very low in this area and it could not be accessed experimentally.
The integration area for Q_z is typically chosen close around α_c in order to "catch" all maxima. The highest ISA in the sample, which is the top of the dots is at around $\widehat{z} \approx 1,1$. At higher z values no ISAs exist in the sample. The integration area is illustrated with a red background in figure 2.15.
One has to state that in the conventional ISS model, ISAs are assumed only above the sample surface at $\widehat{z} > 0$. The Q_z intensity distribution of ISAs underneath the sample surface is not considered in the conventional model. It is clear from this point that another approach is needed for ISAs underneath the surface. Such an approach will be proposed in chapter 3.1 of this thesis.

Ensemble of the Iso strain areas

The schematic drawing in figure 2.14 shows the FT of three casually selected ISAs placed at different Q_{rad} positions in reciprocal space. The accuracy is optimized, if the number of determined ISAs inside the Dot is possibly high, since in that case, the vertical extension of every single ISA is small and the assumption of identical strain inside is suited. In figure 2.16 the overlap of a large number of the FT's of different ISA's is depicted.

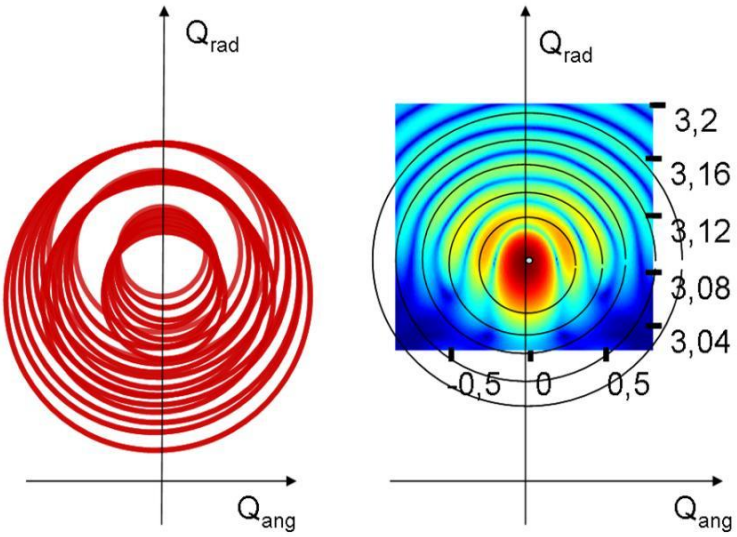

Figure 2.16: Left: Schematic drawing of graphical overlap of the FT's of a set of ISA's. Right: The calculation of the reciprocal space intensity based on a realistic QD FEM model. During the calculation, the FTs of different ISAs were coherently added. A matlab based algorithm, developed by Dr. Daniil Grigoriev, was used.

Figure 2.16 can be used for an interesting comparison: On the left side the simple graphical overlap of the FTs of single slices leads to the characteristic horseshoe like curved maxima in the upper area. The same curves are visible on the calculated image. During the calculation, coherent summation of the complete QD was used. The difference between both pictures is very delicate. In both cases similar maxima are visible. The incoherent summation can never produce extinction. At the lower part, where the rings do not overlap, a constant flat background is created. In case of the coherently calculated map, the addition of complex numbers with different phase enables extinction. Therefore zero intensity is possible. This effect is visible by comparing both pictures. The maxima are similar on the left and on the right. The smooth background in the lower part

of the left image does not exist in the right one. Instead destructive interference has "killed" the intensity.

In the next chapter, the accuracy of the iso-strain model will be evaluated in detail for the quantum dots of interest in this thesis. It will be seen, that, as it is, the model suffers from increasing inaccuracy for decreasing size of dots. That happens because an essential part of the key features addressed to the dot by the conventional ISS model are generated by the strained regions in the substrate. However, the principle "as simple as possible, as precise as necessary" is strongly appealing especially for the robust use and application to large sample series in technological studies. Therefore, a new model, the holistic Iso strain model (HISS), will be proposed that overcomes the essential limitations.

Summary

In this chapter the theoretical background for the later method development as well as method application (i.e. quantum dot study) was introduced. This included the kinematical scattering theory, selected dynamical effects and a short introduction to the iso-strain scattering model. Two measurement techniques, GID and GISAXS, were described in detail.
In case of kinematical scattering theory it was shown that stepwise coherent summation of the scattering amplitude of one single electron (Thomson scattering) finally leads to the scattering amplitude of an object. It was shown that if kinematical theory and Fraunhofer approximation are combined, the scattering amplitude can be interpreted as the FT of the electron density, i.e., its reciprocal space representation. In this way, the FT of the shape function for example is "pinned" to every reciprocal lattice point.
After the introduction of refraction and reflection theory at interfaces, GID and GISAXS techniques that enable the measurement of the scattering amplitude around the two reciprocal lattice points (000) and (220) were introduced. It was shown how side facets, positional ordering and the lateral aspect ratio of the dots can be extracted from GISAXS data.
In case of the GID-measurement the situation is more complicated since in this geometry the exact position of the (220) reciprocal lattice point is lattice parameter dependent. Therefore, areas of the quantum dot with different lattice

parameters will appear in reciprocal space at different positions. In order to still use simple considerations during the analysis, an additional model, the conventional iso-strain model was introduced.
Both, the kinematical approximation itself and the iso strain model, are assumptions that neglect physical effects which are assumed to be small. It is necessary to qualitatively and quantitatively test the accuracy. This will be done in the special case of the quantum dots that are relevant in this thesis in the next chapter.

3 Methodical Development

3.1 Methodical Development 1 - The Holistic Iso-strain Model

In the previous paragraph the kinematical theory and the conventional iso strain scattering model were introduced. Both are based on a number of approximations that neglect physical effects. In this chapter the validity of these approximations is qualitatively and quantitatively evaluated. I will be shown that the principals of the conventional iso strain approximation are surprisingly well suited, but it suffers from incompleteness, especially in case of small QDs, that a most relevant in this thesis. This incompleteness leads to misinterpretations that refer to more than 50% of the relevant data in some cases.
A new model, the holistic iso strain (HISS) model, is introduced in this chapter in order to overcome the limitations an enable correct interpretation of the key features.

Test Quantum Dot for the forward Calculation - generated with FEM

In order to test the accuracy of the kinematical and the ISS approximation a "test-QD" with exactly known shape, chemical composition and strain distribution is needed to perform forward calculations of scattering maps. The correctness of the backward analysis can be evaluated in that way. In order to obtain a realistic test-QD, the shape and the chemical composition are chosen according to the typical QDs of interest in this thesis. The test-QD consists of $In_{0,9}Ga_{0,1}As$ dots on $GaAs(001)$ substrate. A realistic strain distribution for the test-QD is obtained by finite element modeling (FEM).

Detailed descriptions of FEM can be found in (14, 60, 93) for example. A description of the finite element modeling process of the test-QD that is used in this thesis is given in (86). On the next pages the principles of the calculation are illustrated. The result will be intensively discussed since they give first evidence for the need of the HISS model.
The strain in the QD and the substrate is generated as a consequence of heteroepi-

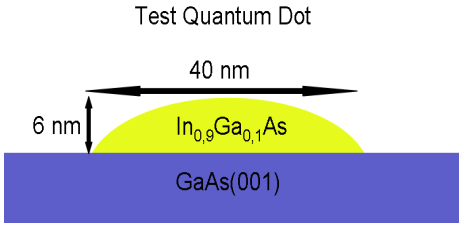

Figure 3.1: Test-QD for the forward calculation of scattering maps. The size and chemical composition are chosen according to the "real" QDs under investigation in the later chapter. Realistic strain distribution inside the dot and the substrate is calculated via the FEM method for the depicted test-QD model.

tactical growth. The term epitaxy is derived from the Greek word epi, meaning "above", and taxis, meaning "in ordered manner". Heteroepitaxy describes an energetic favorable connection of two materials, where perfect matching of the lattice parameter and crystallographic orientation at the interface is achieved. In that way, atomic bonding (covalent or mixed covalent ionic in case of Si or GaAs) is continued atom by atom throughout the interface. The price to pay is compressive in-plane strain in the material with the larger and tensile in-plane strain inside the material with the smaller lattice parameter. With increasing distance from the interface this strain relaxes. Efficient elastic strain relaxation is possible if the material is organized in 3D dots instead of a 2D layer, which already explains, as seen late in detail, the reason for the dot growth.

Lattice Mismatch and Elastic Properties as Input for FEM

The difference between the substrate and dot lattice parameter is expressed by the mismatch m:

$$m = \frac{a_{dot}^{rlx} - a_{sub}^{rlx}}{a_{sub}^{rlx}} \tag{3.1}$$

where a^{rlx} is the relaxed bulk lattice parameter. In case of the test-QD, that consists of $In_{0,9}Ga_{0,1}As/GaAs(001)$, the natural bulk lattice parameter is calculated according to Vegard's law

$$a_{In_xGa_{1-x}As} = xa_{InAs} + (1-x)a_{GaAs} \tag{3.2}$$

and the mismatch is

$$m = \frac{a_{In_{0,9}Ga_{0,1}As}^{rlx} - a_{GaAs}^{rlx}}{a_{GaAS}^{rlx}} = 1,0645 \tag{3.3}$$

which means, that the bulk lattice parameter of the test-QD material is approximately 6.5% larger than the one of the substrate. In the FEM calculations the lattice parameter difference is indirectly expressed via a different thermal expansion coefficient α_{th}. Increasing the temperature by ΔT leads to "thermal strain", that represents the larger lattice parameter of the dot:

$$\epsilon_{ij}^{T} = \alpha_{th} \Delta T \delta_{ij} \tag{3.4}$$

If the material can freely expand, the actual strain corresponds to the "thermal strain". This represents the case where the dot material is totaly relaxed, i.e.,

$$\epsilon_{ij}(\vec{x}) = \epsilon_{ij}^{T} \tag{3.5}$$

There are no remaining forces. The epitactical connection of areas with different lattice parameters induces strain. The different lattice parameter are expressed via different koiefficients α_{th}. In this case a strain difference, called elastic strain $\epsilon_{kl}^{E}(\vec{x})$, exists between the thermal strain (free expansion) and the actual strain:

$$\epsilon_{kl}^{E}(\vec{x}) = \epsilon_{ij}(\vec{x}) - \epsilon_{ij}^{T} \tag{3.6}$$

The corresponding forces, called stress, can be expressed by Hooke's law

$$\sigma_{ij}(\vec{x}) = c_{ijkl}\epsilon_{kl}^{E}(\vec{x}) = c_{ijkl}[\epsilon_{kl}(\vec{x}) - \alpha \Delta T \delta_{kl}] \tag{3.7}$$

where c_{ijkl} is the elasticity tensor of the material. In case of GaAs and InAs the elasticity tensors are

$$c_{GaAs} = \begin{pmatrix} 1.4505 \cdot 10^{-7} & 2.625 \cdot 10^{-8} & 5.32 \cdot 10e^{-8} & 0 & 0 & 0 \\ 2.625 \cdot 10^{-8} & 1.4505 \cdot 10^{-7} & 5.32 \cdot 10^{-8} & 0 & 0 & 0 \\ 5.32 \cdot 10^{-8} & 5.32 \cdot 10^{-8} & 1.181 \cdot 10^{-7} & 0 & 0 & 0 \\ 0 & 0 & 0 & 3.245 \cdot 10^{-8} & 0 & 0 \\ 0 & 0 & 0 & 0 & 5.94 \cdot 10^{-8} & 0 \\ 0 & 0 & 0 & 0 & 0 & 5.94 \cdot 10^{-8} \end{pmatrix}$$

$$c_{InAs} = \begin{pmatrix} 1.0387 \cdot 10^{-7} & 2.4685 \cdot 10^{-8} & 4.526 \cdot 10^{-8} & 0 & 0 & 0 \\ 2.4685 \cdot 10^{-8} & 1.0387 \cdot 10^{-7} & 4.526 \cdot 10^{-8} & 0 & 0 & 0 \\ 4.526 \cdot 10^{-8} & 4.526 \cdot 10^{-8} & 8.329 \cdot 10^{-8} & 0 & 0 & 0 \\ 0 & 0 & 0 & 1.9015 \cdot 10^{-8} & 0 & 0 \\ 0 & 0 & 0 & 0 & 3.959 \cdot 10^{-8} & 0 \\ 0 & 0 & 0 & 0 & 0 & 5.959 \cdot 10^{-8} \end{pmatrix}$$

respectively. The elasticity tensor of a compound, for example the test-QD $In_{0,9}Ga_{0,1}As/GaAs(001)$, is calculated by linear interpolation of the matrix elements:

$$c_{comp} = 0,9c_{InAs} + 0,1c_{GaAs} \tag{3.8}$$

The input parameter for the FEM calculation can now be summarized. First the shape of the test-QD has to be fixed. This automatically leads to boundary conditions. The points at the dot to vacuum interface can only move within the interface plane. Variations of the perpendicular to this plane would increase or reduce the dot volume. The physical material properties are introduced by a) the material dependent bulk lattice parameter (expressed via thermal expansion coefficients) and b) by the material dependent elasticity matrix.
Due to limited calculation capacity the size and shape of one elementary volume ("finite element") needs to be larger than the physical unit cell. For highest efficiency the density of elementary volumes is high wherever abrupt strain gradients are expected and low elsewhere. The explicit mesh density of the QD in this investigation can be seen (86) figure 4.2.1.

Discussion of the FEM Result

The raw result of the FEM analysis is the 3D displacement field $\Delta\mathbf{u}(\mathbf{x})$, that describes the absolute shift of a point in the QD model in comparison to its position in the fully relaxed case. For the scattering experiment not the absolute displacement of atoms is relevant, but the local distance between atomic planes. This distance changes compared to the fully relaxed situation only if neighboring points were shifted by different amounts. Thus, the relevant quantity for the scattering experiment are the partial derivatives of the displacement

$$\epsilon_{ij} := \left(\frac{\delta u_i}{\delta x_j} + \frac{\delta u_j}{\delta x_i} \right) \tag{3.9}$$

Which is a 3x3 matrix, called strain tensor. The diagonal elements of the strain tensor are called principal strains. The values on the diagonal correspond to a change in atomic plane distance along the three principal tensor axis. These distances are increased for $\epsilon_{ii} > 0$ or reduced if $\epsilon_{ii} < 0$. The non-diagonal elements are called shear strains. The shear strains preserve the distances between the atomic planes but changes their orientation.
In the diffraction experiments in this thesis only the (220) reflection is investigated. This means that only the ϵ_{xx} component of the strain tensor is of interest, where x denotes one main axis of the strain tensor that is oriented exactly along the direction of the diffraction vector (220).

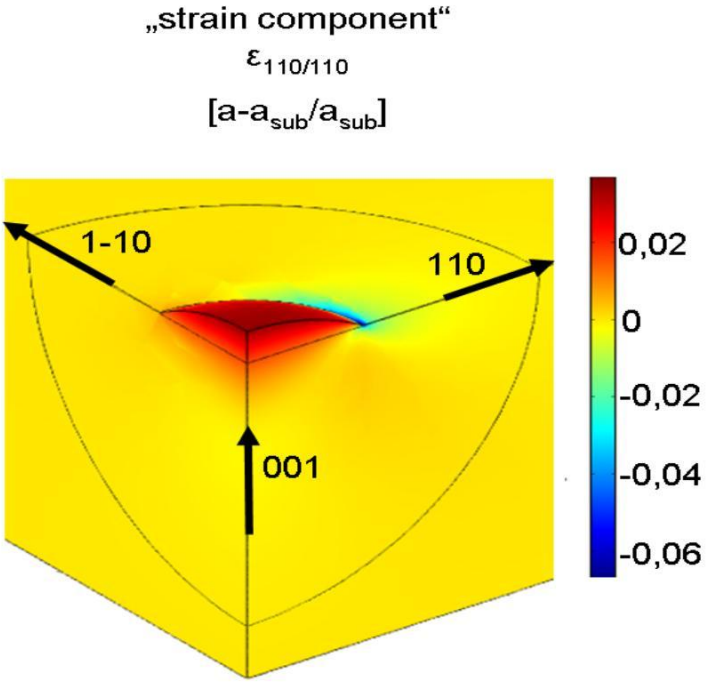

Figure 3.2: Strain inside and around the test-QD. Only one fourth of the complete QD model is depicted in order to enable the "insight" view. Due to symmetry this fourth contains the complete information. The color scale indicates the $\epsilon_{110/110}$ component of the strain tensor. The values are shown as percentage difference of the lattice parameter of the strained material relative to the relaxed substrate lattice parameter. Positive values indicate lattice parameter larger than the substrate lattice parameter, negative values correspond the lattice parameter smaller than a_{sub}. Inside the substrate both are visible: Red color underneath the dot depicts tensile strain, while the blue color around the dot depicts compressive strain.

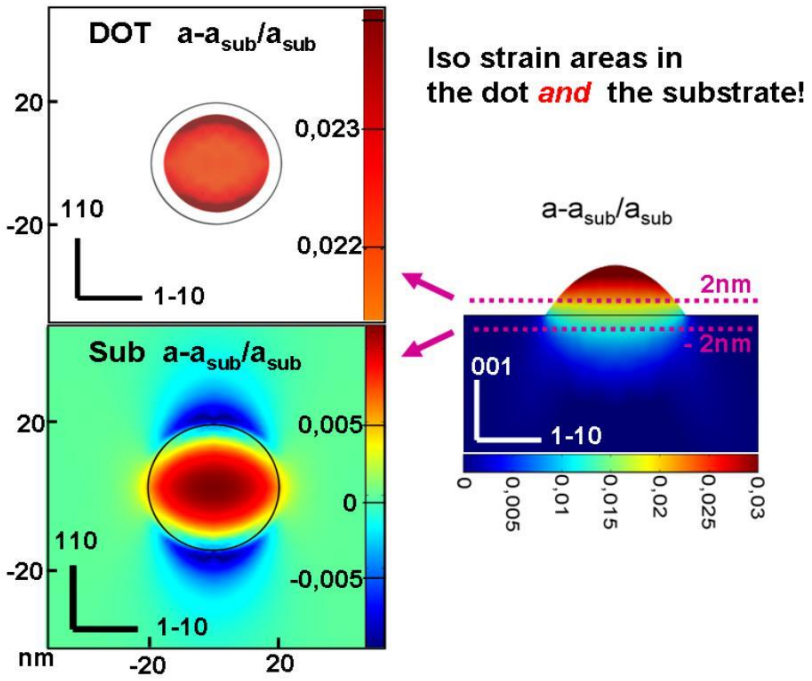

Figure 3.3: Iso strain areas in the dot and the substrate. 2D slices trough the 3D FEM model (figure 3.2) are depicted. Horizontal slices (left) show the iso strain areas in the substrate (upper one) and the dot (lower one). In both cases areas with homogeneous strain can be seen. Also in the substrate ISA, the lattice parameter variation from left to right is smaller than 0.5 %.

The measurement unity and the definition of strain component need further explanation. In general, the term strain denominates the deviation of the local lattice parameter from its relaxed bulk value. The application of this definition is difficult, since the relaxed lattice parameter depends on the chemical composition. For the test-QD the chemical composition is well known. In the realistic case it is not known in advance. Therefore, as measurement unity, the deviation of the local lattice parameter from the substrate lattice parameter is used:

$$\epsilon_{110/110}(\mathbf{r}) = \frac{a^{local}(\mathbf{r}) - a_{sub}}{a_{sub}} \tag{3.10}$$

a_{sub} denotes the relaxed bulk lattice parameter of the substrate. Generally a is the lattice parameter along the (110) axis, which is oriented parallel to the diffraction vector (220).
Figure 3.2 indicates the strain inside the test-QD and its surrounding substrate. The value 0 stands for the relaxed substrate lattice parameter. Positive values

indicate lattice parameter larger than the substrate lattice parameter, negative values correspond to lattice parameter smaller than a_{sub}. As expected, it is seen that the dot relaxes towards the top. In case of full relaxed $In_{0,9}Ga_{0,1}As$, the value is $0,0645$. One can see that at the top the material is "half" relaxed ($\approx 0,03$). At the bottom a small deviation from the substrate lattice parameter (about 1%) is visible. This lattice parameter is coniniously induced inside the substrate. Only after a depth of $5-6\ nm$ under the dot (which corresponds to the dot height) relaxed substrate is visible. Around the tensile strained area underneath the dot, blue parts are visible. These parts represent compressive strain. Its origin can be intuitively understood. In case tensile strain is induced by the dot inside the substrate underneath the dot, the need for space is compensated by compressive strain around this area. At the border between compressive and tensile straine areas the lattice parameter gradient is very sharp. It changes from 1% to -5% within very small distances.
In order to investigate the dot and substrate strain a little closer, 2D cuts thought the 3D model are shown in figure 3.3. The upper left map illustrates a horizontal cut though the dot 2 nm above the substrate. It can be seen that the complete cross section is homogeneously red colored (fig. 3.3 upper left). In order to see the small difference, the color scale was refined compared to the vertical cut. If one follows the values from left to right through the vertical center of the red area, the strain variation is smaller than 0,001. Thus, the lattice parameter fluctuation is less than $0,1\%$ inside this iso strain area. This already suggests good validity of the iso strain approximation. Nevertheless the validity of the iso strain scattering approximation is quantitatively evaluated later in this thesis.
More surprising is the 2D cut thought the substrate 2 nm underneath the dot. Again a homogeneous red colored part is visible, that suggests the existence of iso strain areas in the substrate. This iso strain area is not delimited by vacuum (end of the quantum dot), but it is delimited by blue color (compressive strain) at the top and bottom and by green color (relaxed substrate lattice parameter) on the left and right. Again the scale has to be refined in order to see lattice parameter differences inside this iso strain area. Fluctuation of approx $0,7\%$ can be seen, which is a little more than in case of the cut through the dot. Scattering simulations will show that these iso strain areas in the substrate are homogenious enough in the inside and delimited enough towards the outside to generate thikness oszillations that contribute to the key features. The scattering of the test-QD

can not be investigated within the conventional iso strain scattering model, since the iso strain areas in the substrate (fig. 3.3 upper left) would be completely neglected. In order to include these areas, a new model, the holostic iso strain scattering model, is now introduced.

Holistic Iso Strain Scattering Model

The holistic iso strain (HISS) model intends to describe the scattering of free standing quantum dots including the scattering contribution of the substrate. As shown later, the substrate contribution is essential to correctly interpret the key features in reciprocal space, that are fully addressed to the dot by the conventional iso strain model.

Figure 3.4 depicts the full calculation (left) and the interpretation of the scattering according to the iso strain model (right). The full calculation is done in the following. The FEM result represents a 3D matrix. For every point in this matrix the position x,y,z and the strain component ϵ_{xx} is known. The density of these points is intentionally inhomogeneous (high density in areas with high expected strain modulations and vice versa). From this matrix very thin lateral slices of a thickness of $2\mathring{A}$ (adapted to the Mono layer thickness) are extracted. For these slices a homogeneous distribution (grid) of data points is calculated by positional interpolation of the values of the inhomogeneous distributed data points from the FEM model.

The calculation of the scattering map is done in the following way. According to kinematical theory the scattering amplitude is

$$A(\mathbf{Q}) = \int_{Vz}\int_{Vy}\int_{Vx} \rho(\mathbf{r}) e^{i\mathbf{Q}\mathbf{r}} dxdydz \tag{3.11}$$

Since the full model was segmented in a number N of "sufficiently thin" lateral slices $\rho^i(\mathbf{r})$ the "*Riemann segmentation*" can be applied to substitute the z-integral:

$$A(\mathbf{Q}) \approx \sum_{i=1}^{N} \int\int \rho^i(\mathbf{r}_{||}) e^{i\mathbf{Q}_{||}\mathbf{r}_{||}} e^{iQ_z z^i} d\mathbf{r}_{||} \tag{3.12}$$

This conversion to a discrete sum does not represent the iso strain model. The

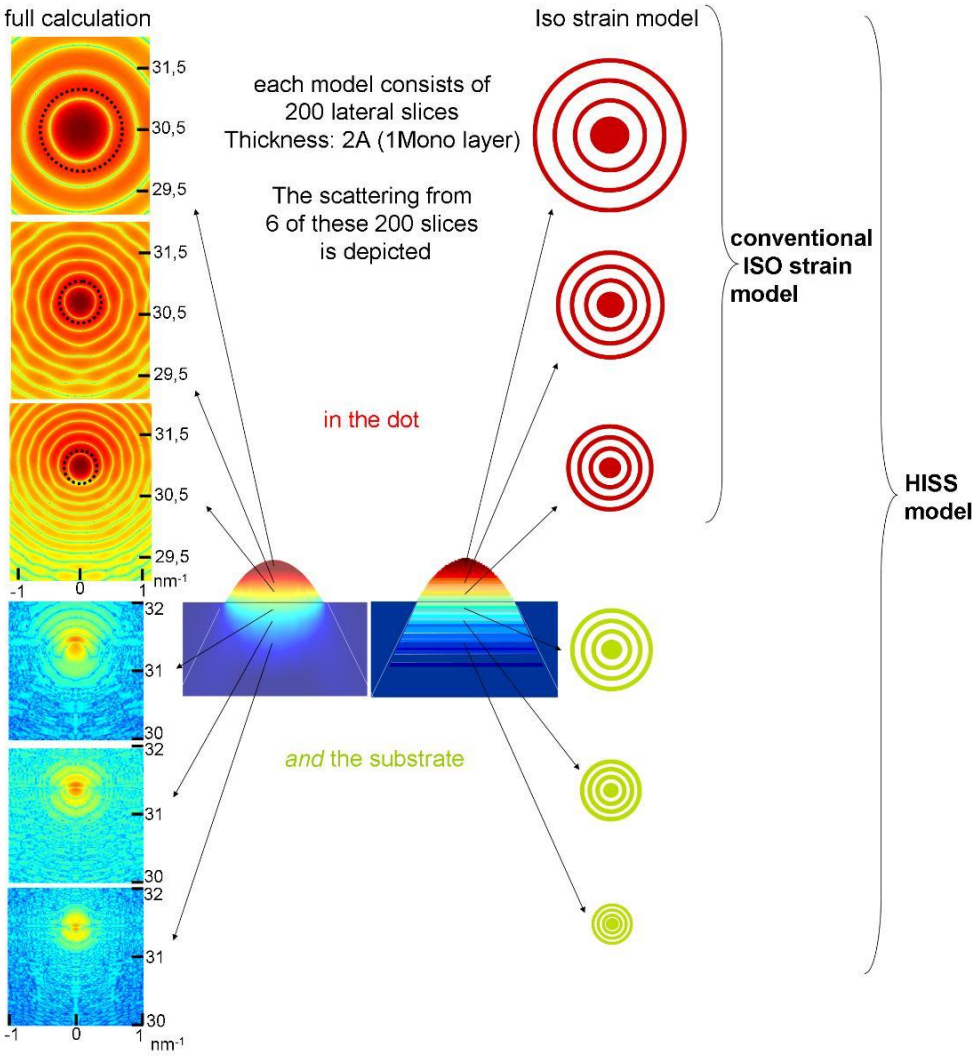

Figure 3.4: Scattering from single lateral slices through the test-QD. Left: The full calculation of the scattering from the actual strain values is given. Right: Schematic illustration of the scattering according to the iso strain model. The lattice parameter inside one iso strain area is constant in this model. The scattering thus corresponds to Bessel like rings that are centered around the reciprocal space values, that correspond to the lattice parameter of the corresponding iso strain area.

strain values inside each slice $\rho^i(\mathbf{r})$ are not assumed to be homogeneous. They are the real values from the FEM simulation. The strain distribution inside two of these slices, one thought the substrate and one through the dot, is visible in figure 3.3. Since the thickness of the layers is extremely thin the thickness oscillations have extremely large oscillation periods along q_z and can be approximated by 1. the total scattering amplitude is thus calculated by

$$A(\mathbf{Q}) \approx \sum_{i=1}^{N} S^i(\mathbf{Q}_{||}) e^{iQ_z z^i} \tag{3.13}$$

where

$$S^i(\mathbf{Q}_{||}) = \int\int \rho^i(\mathbf{r}_{||}) e^{i\mathbf{Q}_{||}\mathbf{r}_{||}} d\mathbf{r}_{||} \tag{3.14}$$

$S^i(\mathbf{Q}_{||})$ is shown for selected layers in figure 3.4 on the left side. It becomes clear that the strain values inside one slice are not exactly identical. If they were, the FT would correspond to homogeneous and concentric Bessel circles centered around exactly one reciprocal space position, that corresponds to the homogeneous strain value, like illustrated on the right side of figure 3.4. Instead the rings are not homogeneous. They seem to be "opened" at the lower part and more intense at the upper part. The approximation of concentric rings in general, however, seems well suited in case of the slices through the dot, and a little less, but still accurate in case of the slices through substrate.
The essence of the HISS model is the correct interpretation of the key features in the scattering map. These key features are the first order shape scattering oscillations, i.e. the radius and position of the Bessel rings from each iso strain area. The calculated rings in figure 3.4 are not perfect Bessel rings. While $S^i(\mathbf{Q}_{||})$ from the ISA at the top of the dots is very close to that approximation, the circles are less complete the lower the iso strain area is situated. Only ring fragments are visible due to the heterogeneous inner strain distribution. However, the two key parameters that are later used in the analysis, the radius and the position of every S(Q) are perfectly predicted. This means that the HISS model is not suited to predict the whole reciprocal space map, but, as far as key features are visible in the measurement data, the HISS model enables to extract the lattice parameter and diameter of every ISA from the position and radius of the Bessel rings in the scattering map. The corresponding mathematical relations are

$$|H|^i = \sqrt{h^2 + k^2 + l^2} \cdot \frac{2\pi}{a^i} \tag{3.15}$$

and

$$D^i = \frac{2 \cdot f}{q^i_{max}}. \tag{3.16}$$

In case of circular shaped ISAs $f = 5.13$ is the value of the first order side maximum of $(J_1(x)/x)^2$. J_1 denotes the first order Bessel function. In this way the pair $(a_i; D_i)$ is obtained for single ISAs.
Until know single ISAs and the scattering of single ISAs was considered. In the realistic experiment all iso strain areas contribute, if the complete reciprocal space map is measured. At one measurement point a certain number of iso strain areas contributes even simultaneously. The question arises whether the HISS model also describes the reciprocal space map of the complete QD model, which means the scattering from all iso strain areas, including possible interference. According to kinematical theory, the scattering of the ensemble of iso strain areas is the coherent summation of the scattering of the single iso strain areas:

$$I^{total}(\mathbf{Q}) \propto \left| \sum_i^N S^i(\mathbf{Q}_{||}) e^{iQ_z z^i} \right|^2 \tag{3.17}$$

where $S(\mathbf{Q})$ is a complex number. In figure 3.4 only the Amplitude of $S(\mathbf{Q})$ was depicted. In order to evaluate the weight of the contribution of the substrate and the dot separately

$$I^{dot}(\mathbf{Q}) \propto \left| \sum_{i \in dot} S^i(\mathbf{Q}_{||}) e^{iQ_z z^i} \right|^2 \tag{3.18}$$

and

$$I^{sub}(\mathbf{Q}) \propto \left| \sum_{i \in sub} S^i(\mathbf{Q}_{||}) e^{iQ_z z^i} \right|^2 \tag{3.19}$$

is also calculated. The result (given in figure 3.5) is very surprising.

The key features, which are the first order shape scattering maxima, are visible on all three maps. They are marked with a dashed line in case of the dot scattering and with a continuous line in case of the substrate scattering. On the scattering map of the total system both lines are visible. It is very surprising that the substrate contribution tends to be the *dominant* source for the *key features*. It can be seen that more that 50% of the visible key features in the total map are generated by the substrate. From this picture one has to conclude that the interpretation in the conventional ISS model, that adresses all key features to the

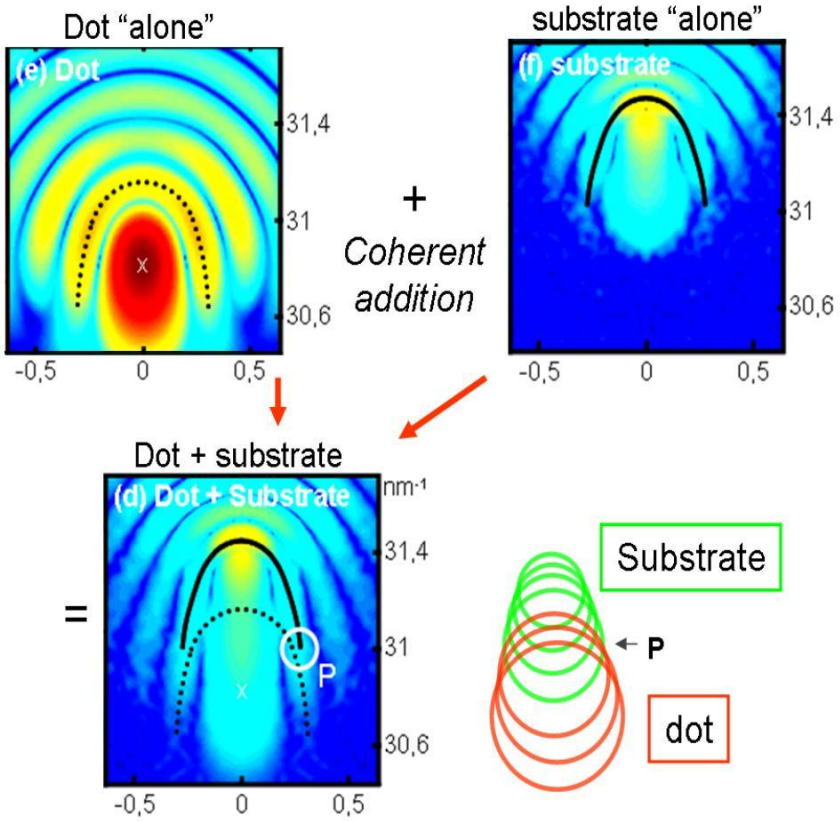

Figure 3.5: Comparison of contribution of the substrate and the dot to the total scattering map. The key features are marked with a dashed line in case of the dot scattering and with a continuous line in case of the substrate scattering map. On the scattering map of the total system both lines are visible. It can be seen that more that 50% of the visible "key" features in the total map are generated by the substrate and not by the dot.

dot, is incomplete. The contribution of the dot, especially the iso strain areas that are situated at the top of the dot, generate nice and pronounced Bessel rings as long as they are alone, not in neighbourship with the rest of the model. In case the scattering of the ensemble is calculated, the top areas seem to loose importance while the bottom and substrate iso strain areas gain weight. The ration between dot and substrate contribution depends on the concrete case. The principle behind that effect is the interference of the scattering of different iso strain areas, that enhances or reduces the relative contribution of single ISAs, once the scattering of the ensemble is calculated. A detailed study is given in the next paragraph.

Summary - Holistic Iso-Strain (HISS) Model

In this section the holistic iso strain (HISS) model was introduced. It was shown that the HISS model is able to deliver a correct interpretation of the key features in reciprocal space. The model offers the possibility to extract the diameter and the lattice parameter of all iso strain areas in the sample. The conventional iso strain model neglects the contribution of the substrate. In our case of small technological relevant dots more than 50% of the key features would be untruely addressed to the dot by the conventional iso strain model. In the next paragraph the HISS model is tested under different scenarios arrising from the inclusion of dynamical effects. In the after next paragraph an express analysis method is introduced that combines the outcome from the HISS analysis with finite element methods and thus delivers tomogaphic QD images containing strain and chemical composition distribution.

3.2 Study of Interference between Iso Strain Areas and Multiple Scattering Effects

In the previous paragraph it was shown that the HISS model allows to extract the lattice parameter and the diameter of every iso strain area (in the dot and the substrate). This result might be surprising. Interference of the scattering response of different iso strain areas for sure leads to a scattering result for the whole system, that does not simply correspond to the incoherent summation of the scattering of the single ISAs. It is therefore not obvious that the scattering of every single ISA is identifiable in the final map of the ensemble and, even more,

suited to extract D and a. In this paraghraph the effect of interference between the scattering of different ISAs and the influence of dynamical effects is qualitatively studied.
In the following the scattering of the ensemble is calculated by coherent summation of the scattering of the single ISAs

$$I(\mathbf{Q}) = \left|A(\mathbf{Q}_{||}, Q_z)\right|^2 \propto \left| \sum_{i=1,2,\ldots}^{N} S^i(\mathbf{Q}_{||}) e^{i\mathbf{Q}_z z^i} \right|^2 \tag{3.20}$$

and by incoherent summation. In this case, first, the square amount of the complex scattering amplitude of each ISA is calculated, afterwards the summation is done. The *coherent* sum is thus replaced by the *incoherent* sum:

$$\left| \sum_{z=1,2,\ldots}^{N} S_z(\mathbf{Q}_{lat}) e^{i\mathbf{Q}_z \mathbf{r}_z} \right|^2 \approx \sum_{i=1,2,\ldots}^{N} \left| S^i(\mathbf{Q}_{||}) e^{i\mathbf{Q}_z z^i} \right|^2 \tag{3.21}$$

Figure 3.6 depicts the result according to both calculation types. As one might have expected, the total absolute intensity is much larger in case of coherent summation. In order to compare also the relative intensity distribution, both maps are normalized. Surprisingly, the intensity distribution is very similar on both maps. Only a careful comparison reveals the small differences. In case of incoherent summation the individual contribution of every ISA is intuitively understandable: The large ISAs at the bottom of the dot contribute more than the small ones at the top of the dot. Thus, a continuous decay of intensity is seen along a vertical centered line from the substrate peak towards the lower end of the map. In case of coherent summation the contribution of different iso strain areas is less regular. The same decay as in case of incoherent summation is visible, however, the intensity decay is superposed by another modulation: At the value of $31,1 nm^{-1}$ and additional intensity enhancement is visible. The ratio between the contribution of different ISAs in case of coherent summation is not the same as in case of incoherent summation. The first order maxima of the shape scattering of each ISA is clearly visible in both cases. Even if the peak value is differently predicted depending on whether coherent or incoherent addition is used, its position is the same for both calculation types.
Here one can already state that coherent summation leads to slight enhancement of the contribution of certain iso strain areas in comparison with the others. This slight enhancement does not prohibit the identification of single iso strain

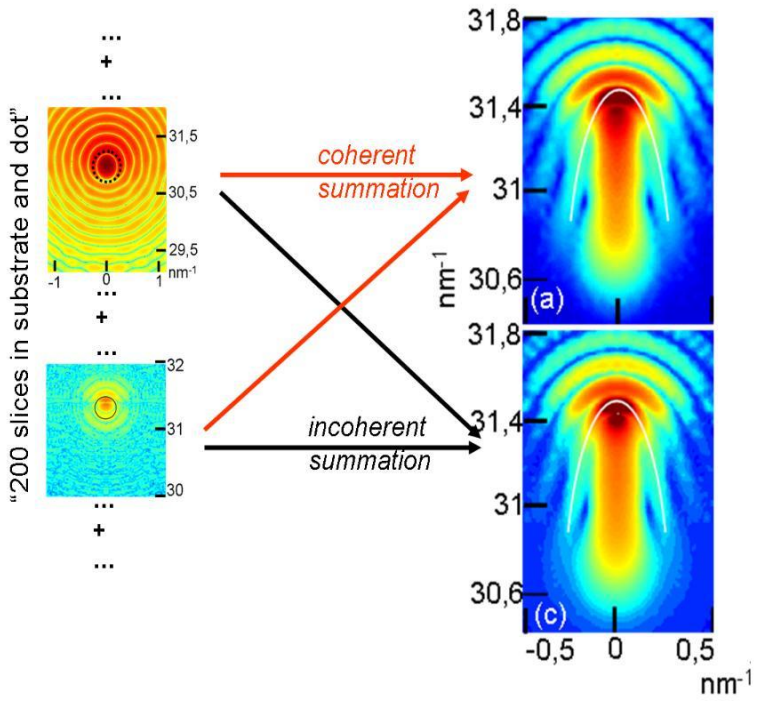

Figure 3.6: Comparison of coherent summation (pure kinematical theory) and incoherent summation according to the HISS concept. Surprisingly the total scattering map is very similar in both cases. Figure 3.10 illustrates the condition that is necessary for that similarity of the scattering maps.

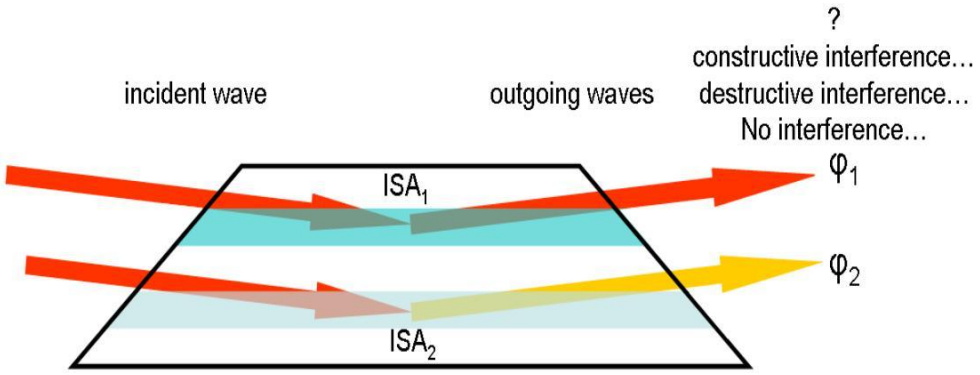

Figure 3.7: Illustration of the question to answer: How do waves that are diffracted at different ISAs interfere?

areas and it does not disturb the analysis of the position of the first order shape scattering.

Principally this result is sufficient to reason the later analysis procedure. For a more complete understanding, the reason, why only slight intensity modulations but never real destructive interference between the scattering of different iso strain areas can be observed, is investigated in the following.

Figure 3.7 illustrates the question to answer. If one wants to investigate how the scattering response from different ISAs interferes, one needs to take a closer look at their phase differences. Two sources for phase differences can be identified.

1. Path difference: The wave scattered at the higher positioned ISA traveled less way than the one at the lower ISA (compare standard reflectivity). Their path difference corresponds to a phase difference (ΔQ_z).

2. Strain: Different ISAs have a different lattice parameter and thus diffracts at different angles ($\Delta Q_{||}$).

Point number two is treated first. Principally one might think that never more than one ISA is excited at once by the incident radiation, since Bragg's law is only fulfilled for discrete pairs of incident angle (θ) and lattice parameter a, within a very small acceptance interval (Darwin width). Figure 3.8 explains via "Umwegeanregung" why at one incident angle θ also ISAs that do not fulfill the Bragg law can be exited. Besides the kinematical single diffraction process, also combinations of diffraction and diffuse scattering must be considered. It is possible that a phoiton arrives at an angle that is unsuited to fulfill the bragg

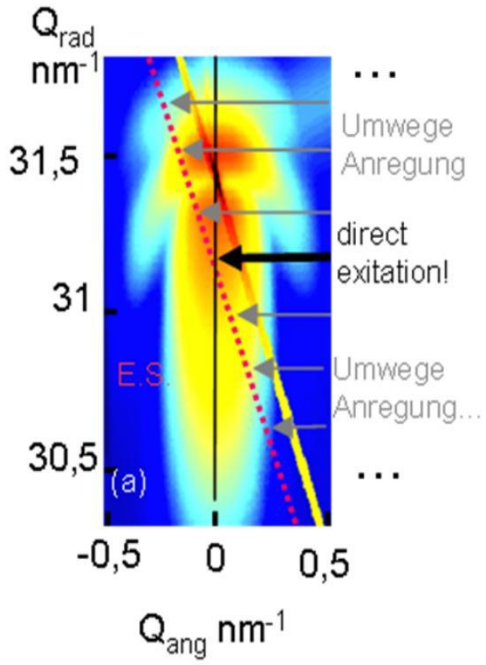

Figure 3.8: Illustration of "Umwegeanregung". Besides the directly exited ISA also other ISAs are exited at one incident angle due to multiple scattering effects that allow combinations of diffuse scattering and diffraction.

condition of a certain ISA, but after diffuse scattering e.g. by the dot shape the Bragg condition might be fulfilled. Also other combinations are possible. Details are described in textbooks (29).

In the example of figure 3.8 the dashed line corresponds to the Ewald's sphere (its large radius allows a line-approximation) of an incident wave entering at an angle θ that is is chosen to directly excite an ISA at the bottom of the QD. It can be seen, that besides the direct excited ISA scattering response, the Ewald's sphere crosses also areas of diffuse scattering that do belong to other ISAs. An estimation revealed, that the highest situated ISA that is still exited is situated approximately 4 nm above the substrate. In case of ideal QDs (having all absolutely the same shape) the higher order shape scattering oscillations are more pronounced (compare the calculation with the experiment) and points in reciprocal space more far from the direct excited area contribute due to resonant diffuse scattering via "Umwegeanregung" (29).
So far, one can state that the simultaneously excited area in the QD during the

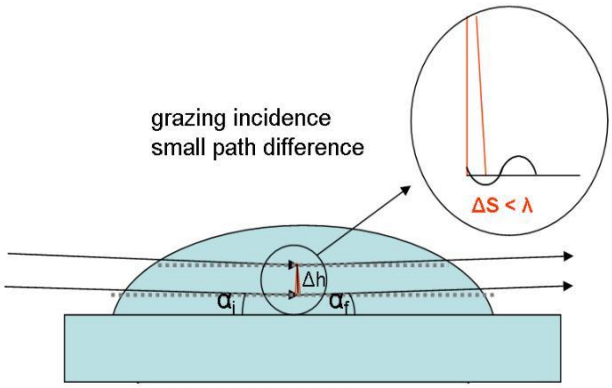

Figure 3.9: Different ISAs are situated at different positions. The path difference that waves scattered at those ISAs is small compared to the wavelength and thus corresponds only to a very small phase shift.

measurement is a thin lateral layer through the dot. The very rough strain gradient (quantum dots are formated in order to enable efficient strain relaxation) from down to the top of the model allows only a very thin slice inside the volume to be directly excited at once. Only via "Umwegeanregung" the neighbor slices (above and below) are also exited, however much less than the directly excited one. The excitation intensity of one ISA drops down very fast with larger distance to the direct excited area. ISAs situated more than 4 nm away from the direct excited ISA are not at all or only very little excited vie "Umwegeanregung". This means that, from this point of view, interference between the scattering of different ISAs is possible, but very limited in space.

path difference - why is the HISS model sufficiently precise?

Since the question whether the scattering of different ISAs can principally interfere, even if different ISAs have different lattice parameter, is answered positive.

In the next step it should be explained why, in spite of possible interference, the coherent and the incoherent summation of $S_z(\mathbf{Q}_{lat})$ leads to very similar results. The path difference between waves diffracted at different ISAs is be calculated according to:

$$\Delta s = z sin\alpha_i + z sin\alpha_f \tag{3.22}$$

The path difference can be written as an integer number times λ plus a phase difference:

$$\Delta s = n\lambda + x\lambda \tag{3.23}$$

The incident and exit angles are kept constant ($\alpha_i = 0.35$, and $\alpha_f = 0.3$ which is the Yoneda level). For these condition the phase difference with reference to the ISA at z=0 can be calculated as a function of z. Figure 3.10 indicates the phase difference between waves scattered at iso strain areas at different height z above the surface.

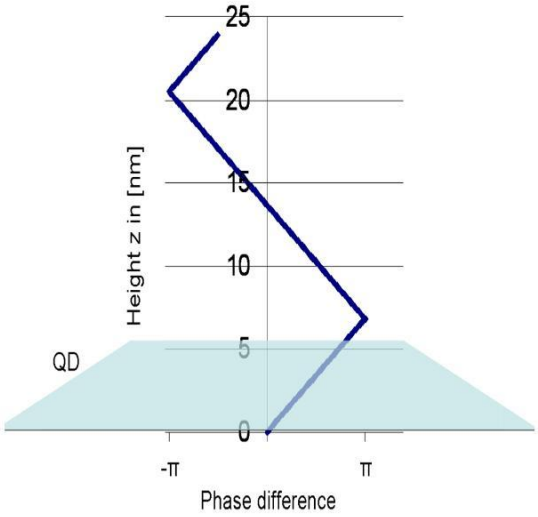

Figure 3.10: The phase difference between waves that are scattered at different Iso strain areas (situated at different height z above the substrate) is illustrated. Only the phase shift due to different positions of the ISAs is considered. The fact that different iso strain areas have different lattice parameter is not included in this phase shift.

Figure 3.10 indicates that the phase difference between the waves scattered at different ISAs is very small. For sure, the phase difference increases with increasing distance between ISAs, but since the QDs are extremely small, the phase difference even for the most distant ISA-ISA pair is less than Π. This explains, why the phase difference shown in figure 3.10 is never sufficient to generate destructive interference.
Using the information of figure 3.10 the result in figure 3.6 can be interpreted. It was seen that, while in case of incoherent addition all ISAs contribute in a regular way to the final scattering map, in the coherent case the ISAs situated in

the center of the QD seemed to contribute more to the scattering map than the ISAs situated at the lower and uper ends of the QD model. A look at the phase differences in figure 3.10 shows that the maximal phase between the scattering of ISAs situated in the center is approximately $\frac{\pi}{2}$. This is not enough to essentially weaken its contribution. The scattering of ISAs situated at the very top has a phase difference, that is only little smaller than π compared to the scattering of those, that are situated at the bottom of the model. This means, that these scattering signals weaken each other visibly. Destructive interference to zero does not happen, since either the top or the bottom can be directly excited. The other part is only excited via Umwegeanregung and thus very week.
Nevertheless the weakening of the contribution of the ISA at the top and bottom (or the strengthening of those at the center) can be observed, if one compares the coherently with the incoherently calculated scattering map. Again, it should be repeated, that this weakening or strengthening is a visible, but small effect, that changes the intensity distribution in the scattering map. The position of the first order Bessel maxima, that will be used in the HISS analysis, stays unchanged.
So far the assumptions needed in the HISS model (identification of the scattering of every ISA in the scattering map and usability of the position of the first order shape scattering maxima) was probed and evaluated.

Assumptions of Kiematical Approximation:

It was shown in the previous paragraph that the specific approximations of the HISS model are justified. In this paragraph the kinematical approximation is tested and evaluated. It is found that there is more difference between using kinematical theory or allowing multiple scattering than between using or not using the HISS approximations. This is in so far surprising as the kinematical approximation is widely used and accepted while the HISS approximation seems to be very rough et the first look. One must state that this comparison holds for the special case of the small QDs investigated in this thesis.
To start the evaluation of kinematical theory all kinamaticals assumptions are again listed:

1. Elastic scattering: modulus of wave vector is always kept constant
2. No extinction or absorption: every electron inside the sample "feels" the undisturbed primary incident wave

Compound	absorption coefficient [1/cm]
GaAs	384.49
InAs	394.76
AlAs	245.43

Table 3.1: Absorption coefficients of GaAs, InAs and AlAs at a wavelength of 8 KeV

3. The incident wave is plane and monochromatic: perfectly sharp wavelength selection, no divergence of the incident beam

4. Far field (Fraunhofer) approximation: the distance between sample and detector is large compared to the dimensions of the scattering object

5. Only interaction of x-rays with electrons in vacuum; refraction index n=1 everywhere; no refraction at the air to sample interface, ect..

6. No multiple scattering: every gamma-photon interacts only once with the sample.

Assumption 1 and 2

Besides the elastic scattering process, also inelastic interactions, where the photon changes its wavelength, are principally possible and therefore the assumptions number 1 and 2 are put into question. Absorption, extinction (reduction of the incident wave due to scattering) and the Compton effect (partial energy shift plus change in propagation direction) all reduce the intensity of the incident wave during its way through the sample. The assumption that every electron inside the sample "sees" the same incident wave has to be discussed.
To avoid absorption only wavelengths around 8 KeV, far away from any absorption edge of the materials, are used. The absorption coefficients μ for GaAs InAs and AlAs are given in table 3.1.

The coefficients reflect the different atomic numbers. If now one assumes that the photons travel under the angle of 0.35° diagonally through the quantum dot, a maximal path length of 40 nm through the dot has to be traversed. In case the dot would fully consist of InAs, which has the highest absorption coefficient, a fraction of only $3.6 \cdot 10^{-3}$ would be absorbed. Therefore the small size of the

Compound	extinction length [μm]
GaAs	0.672
InAs	0.569
AlAs	0.683

Table 3.2: Extinction length of GaAs, InAs and AlAs at a wavelength of 8 KeV

quantum dots supports and validates the neglection of absorption inside the dot. The extinction length of GaAs, InAs asd AlAs are listed in table 3.2.

The weakening of the incident wave due to extinction is thus more important than its weakening due to absorption. After traveling through 40 nm of GaAs, about 6% of the intensity are "lost" due to extinction. As shown later, only a part of the dot is simultaneously in Bragg condition. That means that the intensity loss due to extinction is even smaller than 6%.
From this point of view the assumption number 2 can already be approved to be valid: Since the quantum dots are very small, absorption and extinction can be neglected inside the dot volume and it is suited to assume that the whole dot "feels" the incident wave field without absorption or extinction. For the large bulk substrate underneath the dots these assumptions are clearly incorrect. An electron deep inside the substrate feels only the rest of the incident radiation that is already weekended through absorption and extinction. This issue finally solves the apparent violation of the energy conservation law. Instead of increasing with the number of scatterers N by N^2 as kinematically predicted, the scattered intensity from the substrate is reduced. The exact value of the substrate peak intensity is not used at any point of the analysis procedure that will be presented in this thesis. The deviation from kinematical theory concerning the substrate peak intensity is therefore noted at this point, but it stays without any influence for the later approach.

The last aspect in this consideration is the Compton effect. This effect might be problematic, since it does not only contribute to the absorption, but photons (with reduced energy) could reach the detector after a Compton knock. However, the Compton scattering is dominant compared to the photoelectric process in case that the primary photon energy is "in the order of the rest mass of the electron" $mc^2 = 511keV$ or higher. The use of radiation of $8keV$-photons dimin-

ishes this effect. Furthermore the extremely small number of Compton photons has no strong dependence of the scattering angle and gives rise to a smoothly varying background (33), which does not disturb the later analysis procedure that is independent of absolute intensities.

So far assumptions number 1 and 2 could be approved. Due to the small dot volume, extinction and absorption do not dramatically reduce the primary intensity during the traveling through the dot. From this point of view the conclusion, that every electron inside the dot "sees" the same incident wave, is suited. Later it will be shown that the electrons in the dot might "see" even more than the incident wave. If multiple scattering is considered, the electron might see the incident wave field plus wave fields, that already interacted with the sample elsewhere (e.g. by surface reflection) and now pass through the dot. This is treated within the Distorted Wave Born Approximation (DWBA) later in this chapter.

Assumption 3 and 4

In the following the assumptions 3 and 4 can be validated by considering the experimental setup.
In realistic experiments the incident wave is neither plane nor monochromatic. The two undulator beamlines, that were used for the experiments, are very close to these requirements. The energy resolution and the incoming divergence of the two experimental stations are both very small $\frac{\Delta E}{E} < 10^{-4}$ and $\Delta\Theta_{in} < 0,001°$. The size of the resolution element along ω is thus essentially smaller than the necessary sampling width in that direction. Since quantum dots are nanometer sized objects, the shape scattering in reciprocal space is spread over large distances. The sampling must therefore cover a big area (around 2° in ω), but the step width can be large (0.01°) in the present experiments. The real space view to deal with divergence and imperfect energy resolution is the look to the size of the coherence volume. The longitudinal and transversal coherence length are

$$L_l = \frac{\lambda^2}{2\Delta\lambda} \tag{3.24}$$

and

$$L_t^{h/v} = \lambda \frac{d}{S^{h/v}} \tag{3.25}$$

$S^{h/v}$ is the horizontal and vertical source size, d the Distance between the source and the sample and $\Delta\lambda$ the wavelength resolution. In case of ID01 one has: $L_l = 1,3\mu m$, $L_t^h = 56\mu m$ and $L_t^v = 311\mu m$. In case of ID10B one has: $L_l = 1,3\mu m$, $L_t^h = 6,7\mu m$ and $L_t^v = 2701\mu m$. On the one hand this coherence length is easily large enough to coherently illuminate one nanometer sized quantum dot. In case of the GISAXS experiments even a large number of dots (several thousands) are illuminated coherently, giving rise to the ordering peaks. On the other hand the coherence volume is small compared to the sample to detector distance (about 1 m). This means that the incoming divergence and the imperfect energy resolution help to fulfill the Fraunhofer approximation.

So far the kinematical assumptions from 1 to 4 could be evaluated and approved by standard discussion and easily accessible information about the beamline parameters.

Assumption 5 and 6

The last two kinematical assumptions (5 and 6) cannot be evaluated and approved on the basis of simple consideration. It is clear that refraction can not be neglected since the existence of the critical angle of total external reflection and thus the GID and GISAXS methods in principle are based on this effect. Since there is a considerable chance to be (specular) reflected at the surface (Fresnel coefficient), one must consider not only the diffraction process, but also the pure reflection and even more difficult combinations of diffraction and surface reflection processes. The assumption of one single interaction between sample and x-ray radiation and the assumption of n=1 inside the sample do not hold. The Distorted Wave Born Approximation offers a possibility to deal with multiple scattering effects.
Now, the mistake, coming from neglecting refraction corrections and multiple scattering, has to be qualitatively evaluated. The theoretical background of this dynamical effects (especially refraction and multiple scattering) was introduced in the theory part of the thesis. Now, 4 different scattering scenarios are calculated and compared. They exactly refer to the QDs of this thesis. In these scenarios multiple scattering effects and the iso strain scattering approximation can be switched "on and off" on demand. In that way the effect and the mistake by applying these approximations can be precisely studied. The different reciprocal space maps (according to different scattering scenarios) have been calculated for

the test-QD model (figure hier).

Scenario 1: Kinematical Theory

In this scenario the pure kinematical approach is simulated (see 3.11 a). The different contributions $S_z(\mathbf{Q}_{lat})$ from each layer at the height z are coherently added. The square of the scattering amplitude is calculated after the summation.

$$A(\mathbf{Q}_{||}, Q_z) \propto \sum_{i=1,2,...}^{N} S^i(\mathbf{Q}_{||}) e^{iQ_z z^i} \tag{3.26}$$

and

$$I(\mathbf{Q}) = \left|A(\mathbf{Q}_{||}, Q_z)\right|^2 \propto \left| \sum_{i=1,2,...}^{N} S^i(\mathbf{Q}_{||}) e^{iQ_z z^i} \right|^2 \tag{3.27}$$

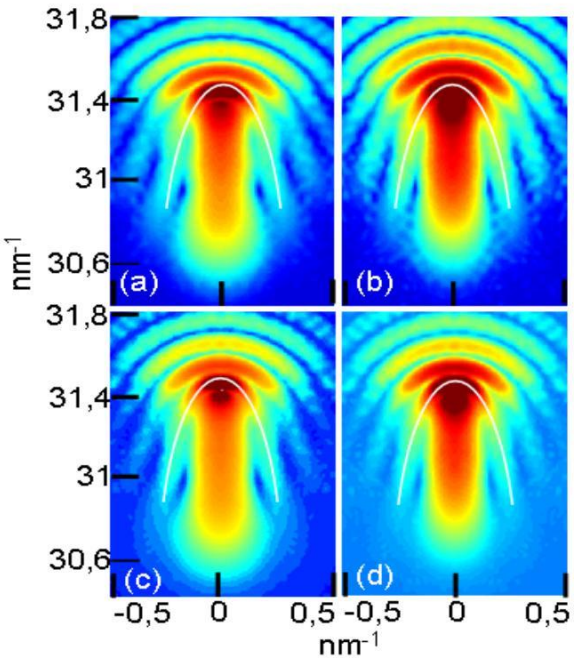

Figure 3.11: Scattered intensity around the (220) reflection, calculated according to the 4 different diffraction scenarios: kinematical (a), kinematical + DWBA(b), iso strain scattering (c), iso-strain scattering + DWBA (d).

Scenario 2: DWBA

This option extends the limits of kinematical theory. Multiple scattering effects, such as the combination of specular surface reflection and diffraction, are considered according to the DWBA concept (see figure 2.7). The mathematical formalism that was used for the simulation (figure 3.11 b) is developed in the following. One can start from the kinematical equation 3.26. The term $S_z(\mathbf{Q}_{||})$ remains unchanged, since it is not affected by the change of Q_z (reflection on a plane surface). The exponent function is split again according to $Q_z = k_z^{in} - k_z^{out}$ in order to let the incident (k_z^{in}) z-wave component (k_z^{in}) and the z-wave component after interaction k_z^{out} reappear.

$$A(\mathbf{Q}_{||}, Q_z) \propto \sum_{i=1,2,...}^{N} S^i(\mathbf{Q}_{||}) e^{iQ_z z^i} = \sum_{i=1,2,...}^{N} S^i(\mathbf{Q}_{||}) e^{ik_z^{in} z^i} e^{-ik_z^{out} z^i} \tag{3.28}$$

Now the term $e^{i\mathbf{k}_z^{in}\mathbf{r}_z}$ is identified as the incident wave and $e^{-i\mathbf{k}_z^{out} r_z}$ as outgoing wave. In kinematical theory the incident wave to the QD is always equal to the primary wave (from the source). In DWBA one must consider, additionally to the primary wave, a wave field that was first reflected at the surface and than hits the QD. The already reflected wave propagates with $-k_z^{in}$. The total wave that reaches the dot is written as $e^{i\mathbf{k}_z^{in} r_z} + Re^{-i\mathbf{k}_z^{in} r_z}$. Where R is the Fresnel coefficient:

$$R(k_z, K_z) = \frac{k_z - K_z}{k_z + K_z} \tag{3.29}$$

with k and K as the wave vectors in vacuum and inside the sample.
The same idea holds for the outgoing wave. Not only the wave field that comes directly from the diffraction with the QD, but also a wave that is reflected at the surface after the interaction with the dot, leaves the sample. Instead of the kinematical expression $e^{-i\mathbf{k}_z^{out}\mathbf{r}_z}$, the outgoing wave is replaced by $e^{-i\mathbf{k}_z^{out} r_z} + Re^{i\mathbf{k}_z^{out} r_z}$. Inserting the new expressions for the incident and outgoing z-wave field in equation 3.27 delivers:

$$I(\mathbf{Q}_{||}, Q_z) \propto \left| \sum_{i=1,2,...}^{N} S^i(\mathbf{Q}_{||}) \left\{ e^{ik_z^{in} z^i} + Re^{-ik_z^{in} z^i} \right\} \left\{ e^{-ik_z^{out} z^i} + Re^{ik_z^{out} z^i} \right\} \right|^2 \tag{3.30}$$

During the experiment $k_z^{in} = k_z^{fix}$ is fixed according to the incident angle (0,35°). The calculation algorithm is then written as:

$$I(\mathbf{Q}_{||}, Q_z) \propto \left| \sum_{i=1,2,...}^{N} S^i(\mathbf{Q}_{||}) \left\{ e^{ik_z^{fix} z^i} + Re^{-ik_z^{fix} z^i} \right\} \left\{ e^{-i(k_z^{fix} - Q_z) z^i} + Re^{i(k_z^{fix} - Q_z) z^i} \right\} \right|^2 \tag{3.31}$$

This formula was applied to simulate the scenario 2: kinematical theory + DWBA. If the two brackets in equation 3.31 are expanded, one obtains the four terms corresponding to the four channels of DWBA depicted in figure 2.7.
Comparing scenario 1 (pure kinematical) and scenario 2 (kinematical + DWBA), one finds differences in the intensity distribution. It can be seen that the intensity close to the substrate Bragg peak seems enhanced, while the intensity at the bottom of the RSM (coming from the top of the island) seems reduced. This is a very important insight. If one would analyse these two maps by evaluating the intensity profiles as frequently done in literature, one might think that scenario 1 depicts data from a quantum dot that is more relaxed than the RSM in scenario 2, since more intensity is diffracted in a region that corresponds to relaxed lattice parameters. This interpretation can not hold since both maps are calculated on the basis of the same test-QD. The different intensities can be explained by the interference between the different channels in DWBA. One must consider interference between the primary wavefield, diffracted at a volume at the height z in the dot and the wave field that first traveled to the substrate, was specular reflected and than diffracts at the volume at z in the dot. The two wave fields have traveled a different path. This path, depends on the height z. The larger z, the higher is the path difference and the phase difference. If z=0 (close to the substrate) this path/phase difference is close to 0, leading to constructive interference. If z has a critical value z' the path length difference corresponds to π and destructive interference occurs. For even larger z values constructive interference follows ect. We can state that a volume inside the QD contributes with different weight to the reciprocal space map depending on its height z inside the dot. This effect was recently published (72). In that publication a 2D plot showing the weight, with which a volume at height z contributes to the RSM, was calculated depending in the incident angle. The same calculation for the wave-

length of 8 KeV was calculated by M. Kaufholz (55) and is depicted in figure 3.12.

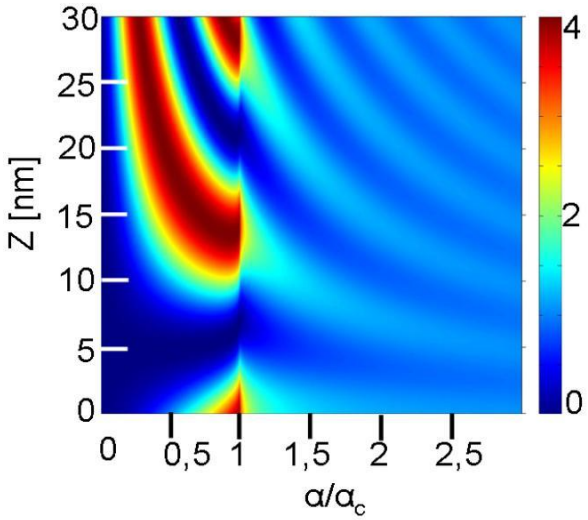

Figure 3.12: Contribution weight of a scattering volume inside the dot. Depending on the incident angle and the position z of the volume above the sample surface, constructive and destructive interference between the different DWBA channels leads to different contribution weights of the volume to the reciprocal space map. The calculation was performed for a photon energy of 8 KEV. Source: (55)

Interference between the different DWBA channels leads to a modulated weight of contribution to the RSM of volumes that are inside the QD at different height z above the surface. At z=0 in-phase interference leads to enhanced contribution, at $z \approx 6nm$ out of phase interference leads to reduced contribution of the volumes at z=6 nm to the RSM. The QDs in this thesis are about 5-6 nm high. This means that the bottom of the dots contributes with enhanced intensities to the RSM, while the top contribute with reduced intensities. This explains why the iso strain scattering concept, that neglects the substrate, fails in case of small dots. The dot contributes with reduced intensity to the RSM compared to the substrate, if DWBA is "switched on". Large dots are high enough to reach the next constructive interference between the DWBA channels at approximately z=14 nm. In this case volumes inside the dot (around a height of z=14) contribute with enhanced intensities. The ratio between substrate and dot contribution weights shifts towards the dot and the conventional iso strain model (that neglects the substrate) gains accuracy.

Besides the very important z dependence, figure 3.12 also indicated the dependence of the contribution weight on the incident angle. Principally it can be seen that below the critical angle the modulations are very pronounced. In this case the reflectivity coefficient is 1 and the primary and the already specular reflected wave have the same intensities. Therefore interference leads to strong enhancement or total destruction of the intensity. For incident angles larger than the critical angle, the specular reflected wave is weaker than the primary one. Interference between both modulates the contribution weight, however, never completely annihilates it.

In summary one can state that the extension of the kinematical approximation to kinematical approximation + DWBA leads to redistribution of the intensity on the RSM due to interference between the DWBA channels. Depending on the height z above the substrates, volumes in the dots contribute with enhanced or reduced intensity the the RSM. This effect shifts the total contribution ration between dot and substrate towards the substrate in case of small dots. This explains, why the conventional iso strain model, that neglects the substrate completely, holds better for large dots than for small ones.

Scenario 3: Holistic Iso Strain Scattering

The approximations of the HISS model were already evaluated in previous paragraphs. Kinematical theory was compared to kinamatical theory + HISS approximations. In this section the HISS approximation is shown again. It has to be studied, whether neglecting the possibility of interference between the scattering response of different ISAs is also justified, if multiple scattering is "switched on" (scenario 4) or "of" (scenario 3). The kinematical (and coherent term)

$$I(\mathbf{Q}) = \left|A(\mathbf{Q}_{||}, Q_z)\right|^2 \propto \left|\sum_{i=1,2,\ldots}^{N} S^i(\mathbf{Q}_{||}) e^{i\mathbf{Q}_z z^i}\right|^2 \tag{3.32}$$

is replaced according to the HISS approximation

$$\left|\sum_{i=1,2,\ldots}^{N} S^i(\mathbf{Q}_{||}) e^{i\mathbf{Q}_z z^i}\right|^2 \approx \sum_{i=1,2,\ldots}^{N} \left|S^i(\mathbf{Q}_{||}) e^{i\mathbf{Q}_z z^i}\right|^2 \tag{3.33}$$

Scenario 4: Iso Strain Scattering + DWBA

In this section the combination of HISS approximation and the multiple scattering via DWBA is investigated. The two brackets, that after expansion lead to the 4 DWBA channels, are visible again in equation 3.34. In difference to scenario 3, now the terms are incoherently added. This is visible in the calculation of the square before summation:

$$I(\mathbf{Q}_{||}, Q_z) \propto \sum_{i=1,2,...}^{N} \left| S^i(\mathbf{Q}_{||}) \left\{ e^{ik_z^{fix} z^i} + Re^{-ik_z^{fix} z^i} \right\} \left\{ e^{-i(k_z^{fix} - Q_z) z^i} + Re^{i(k_z^{fix} - Q_z) z^i} \right\} \right|^2 \tag{3.34}$$

The result (figure 3.11(c)) corresponds to the expectations based on the previous 2 scenarios. The shift of intensity from the lower part of the RSM (top of the dots) towards the region around the substrate peak can be seen, since the contribution weight (see figure 3.12), resulting from interference between different DWBA channel, is enhanced towards the bottom of the QD.

Conclusions for the HISS-analysis method

In the previous paragraph the kinematical approximation and the iso strain scattering approximation were tested. To obtain a qualitative evaluation of these approaches different scattering maps around the 220 reflection were simulated in GID geometry for the same QD model, but with different scattering scenarios. It is found that, depending on the scenario, different scattering maps are obtained. Switching the possibility of multiple scattering effects "on and off" or using coherent or incoherent addition of the scattering of the single ISAs leads to different scattering maps.
The differences between the scenarios can be summarized. While in the simplest approximation (kinematical theory+incoherent addition of the scattering of the different ISAs) every ISA contributes with the same intensity to the reciprocal space map, the distribution of the contributions becomes unequal in case of the other scenarios.

It is possible to draw a real space map that indicates which part of the QD model contributes with what intensity. This map shows periodic oscillations. It

is a characteristic of small QDs that their size is smaller than the length of this periodicity. Complete destructive interference between ISAs is possible for large, but not for small QDs. Nevertheless, even within the small area of the QDs of this thesis, a slight modulation of the contribution weight can be observed. Models or analysis procedures that claim to predict the scattered intensity must include these effect. Thereby it is intersecting that the wide accepted kinematical assumption seems to be even more rough than the assumption of incoherent addition of the scattering of different ISAs. Since in the HISS model intensities do not play any role, the model does not need any of those approximations. While the absolute and also the relative intensity of the first order oscillation maxima changes visibly depending on the specific scenario, its position remains unchanged. The use of this position is therefore not dependent on the validity of kinematical theory and it does not depend on the assumption of incoherent summation of the scattering responses from different ISAs. The amount of information that is extracted from the scattering map according to the HISS analysis is, for sure, reduced to a minimum. Its quality in terms of robustness is increased to a maximum.

3.3 methodical development 2 - the express analysis

Since the validity of the HISS model was in case of small dots was shown in details before the complete analysis procedure that is based on the HISS model will be explained in this paragraph.
The analysis routine is described in the following. Every ISA has its own lattice parameter a^i. The reciprocal space contribution of a certain ISA is centered around by $\mathbf{H^i}$, which is used to determine a^i according to equation 3.15
At a certain $\mathbf{H^i}$ the intensity profile along q_{ang} contains the *key feature*, which is the lateral shape scattering (shape oscillations) of the ISA. The position of the first order maximum Q^i_{max} of these oscillations delivers the diameter D_i of the ISA via equation 3.16.

In case of circular shaped ISAs $f = 5.13$ is the value of the first side maximum of $(J_1(x)/x)^2$. J_1 denotes the first order Bessel function. In this way the pair $(a_i; D_i)$ is obtained for every ISA without defining whether this ISA is situated in the dot or in the substrate.

The further procedure is demonstrated on the three QD samples, that were used for a light emission study (81). The samples consist of $Al_xGa_{0.4-x}In_{0,6}As$ QDs on GaAs(001) and differ by their nominal Al content ($x = 0$, 0.08 and 0.19), leading to emission wavelengths between 660 nm and 940 nm. Details can be found in (81).
The x-ray measurements were performed in grazing incidence diffraction (GID) geometry at a wavelength of 8.1 and 8.14 KeV at the ID01 and ID10B beamlines of the European Synchrotron Facility (ESRF), respectively. At ID01 micro focusing optics were used to reduce the beam size at the sample position to $1.2 \times 2\ \mu m$, which allows sufficient angular resolution for the outgoing beam in combination with a 2D-detector (pixel size: 50 μm, distance from the sample: 91 cm). At ID10B a Ge(111) crystal analyzer in combination with a line detector was used. Preliminary GID measurements were performed at the ANKA SCD beamline.

The first analysis step is the identification of the key features (black line in Figure 3.13(a) in the RSM). Along this line several points are picked. From the Q_{ang}, Q_{rad} values of these points the curves $a(D)$ are directly calculated according to equation (3) and (4), leading to the three data sets for three different samples in figure 3.13(c). That way the lattice parameter and lateral size of every ISA

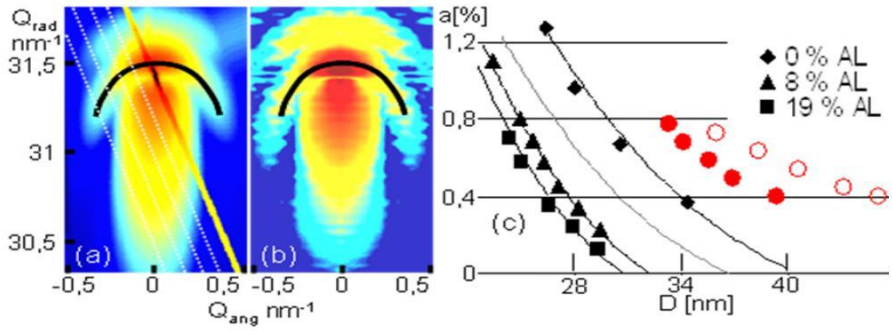

Figure 3.13: (a) Measured and (b) simulated reciprocal space map around the 220 reflection. The intensity perpendicular to the Q_{ang}/Q_{rad} plane was integrated from 0.42 nm^{-1} to 0.47 nm^{-1}, the incident angle α_i was 0.2°. The first order shape scattering maxima (black lines) are visible. Along these lines the black points in (c) are selected. The continuous lines in (c) depict the FEM simulation. The in-situ data (red circles) is shifted upwards by 0.3% to avoid overlap.

is obtained. These values deliver exactly the necessary information to determine the complete QD image if combined with FEM. With FEM calculations alone the system is under-defined, since whether the chemical composition has to be given as input to calculate the strain or vice versa. The situation changes, if the strain curves from the GID analysis (fig.3.13) are used as constraint for FEM simulation. In this case unique solutions are found (see figure 3.14).

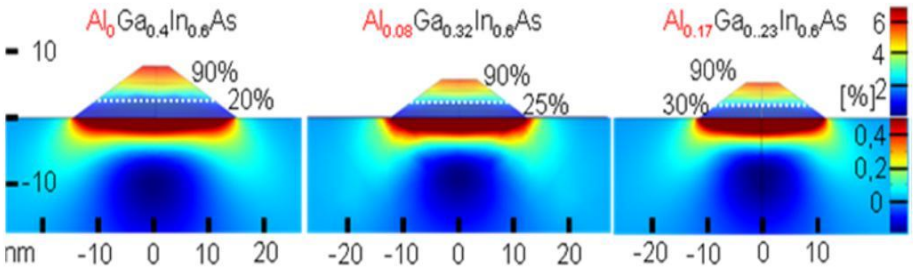

Figure 3.14: FEM data indicating the lattice parameter relative to the substrate for the three samples with different nominal Al concentrations (0, 8 and 17%). The different color scale bars for the dot and the substrate have to be notived.
Even if the nominal Indium concentration is 60% in all cases, a material redistribution inside the dots is visible. The models distinguish a bottom part with smaller and a top part with higher Indium concentrations. From left to right a decrease in size and an increase in the Indium concentration at the bottom is visible.

The FEM calculation procedure follows a systematic. The absolute D-axis

position of the FEM simulated curve $a(D)$ is obtained by choosing the appropriate lateral QD size (equation 3.16). The corresponding slope and curvature can be adapted by varying the amount and distribution of strain creating material (InAs in the present case) along the vertical axis. The concentration of Al is not reflected by FEM calculation, since GaAs and AlAs have nearly identical lattice parameter and elastic properties. The absolute QD height can be taken from SEM or AFM, if available, or from the Q_z intensity profiles, as frequently done in the past (e.g.(39)). The precision of the aaproach is illustrated by the gray curve in figure 3.13 that belongs to a QD with the same chemical composition and distribution as the $Al = 0\%$-sample, but with a 1.2 nm reduced lateral size. A significant shift to smaller D values is visible. The sensitivity to the size can be estimated to approx 0.1 nm. Comparing the grey curve with the $Al = 8\%$ curve, differences in slope and curvature indicate differences in material composition and distribution. A change of only $1 - 2\%$ of In-concentration leads to visible deformation of the curves and disagreement with the experimental data. Within a 5% frame the effect can be compensated by changing the size of the region, in which this content exists. The precision is suited to enable process and performance relevant optimization, such as positional ordering and light emission. A cross check of the method is shown in figure 3.13(b). A full reciprocal space map based on the FEM model for the Al=0% sample (figure 3.14 first Model), that resulted from the described analysis, is calculated (see ref. (27) for details). Conformity with the measured reciprocal space map is visible.

4 Quantum Dot Growth, Property and Performance Study

4.1 Introduction into Quantum Dot Growth with Molecular Beam Epitaxy

Molekular Beam Epitaxy

All samples that are characterized in this thesis are grown by Molecular Beam Epitaxy (MBE). An overview of this technique can be found in (73) "Basics of Molecular Beam Epitaxy". Even if this thesis is focused on the x-ray characterization, some technical growth aspects are shortly mentioned here, since the results of the x-ray characterization are discussed in relation to the growth conditions or post growth processing. Especially the material selection (indium, aluminum, gallium, arsenic), the growth speed and the growth temperature will play an essential role for the interpretation of the x-ray scattering data in chapter 4.2.

The derivation of the equations until the end of this paragraph are cited according to Ref. (73). A pure substance in a closed ultra high vacuum (UHV) at constant temperature T is considered. An equilibrium is established between the gas and the condensed phase (73). The equilibrium gas pressure p_{eq} is a function of the temperature and can be approximated by the Clapeyron equation (96).

$$P_{eq}(T) = A \exp\left(\frac{\Delta H}{k_b T}\right) \tag{4.1}$$

Here ΔH is the evaporation enthalpy and k_B the Bolzmann constant. In case of compound materials (e.g. GaAs) one must consider the possibility of coexistence of several phases. Besides solid gallium arsenide GaAs(s) also solid arsenic As(s) or liquid gallium Ga(l) may appear (see the phase diagram figure 4.1).

In the region 1 the reactions between the components are

$$GaAs(s) \rightleftharpoons Ga(g) + \frac{1}{2}As_2(g) \tag{4.2}$$

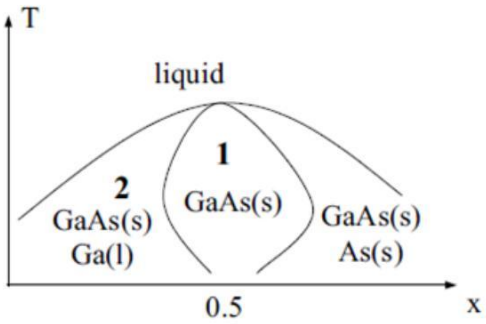

Figure 4.1: Simplified phase diagram (T-x section, temperature and relative material content) for GaAs. (s) is the solid and (l) the liquid phase. A gas phase is always present. Two regions (1 and 2) are distinguished. source: ref.(73)

and

$$2As_2(g) \rightleftharpoons As_4(g) \tag{4.3}$$

The associated mass action equation (32, 73) is

$$P_{Ga}P_{As_2}^{\frac{1}{2}} = K_{GaAs} = 2.73 \cdot 10^{11} \exp\left(-\frac{4.72}{k_b T}\right) \tag{4.4}$$

If $T < 450°$, the P_{AS_4} contribution can be neglected and the total pressure is given by:

$$P_T = P_{Ga} + P_{As_2} = \frac{K_{GaAs}}{P_{As_2}^{\frac{1}{2}}} + P_{As_2}. \tag{4.5}$$

If in a compound like Ga_xAs_{1-x} the partial pressure of Gallium for example is bigger than the Arsenide one, the composition of the condensed phase will be enriched with Gallium and the partial pressure is reduced. If a minimum for a certain x exists, this will be asymptotically reached. In this point the sublimation is congruent and the equation for a minimum of the pressure is

$$\frac{dP_T}{dP_{As_2}} = \frac{dP_T}{dP_{Ga}} = 0 \tag{4.6}$$

The solution using equation 4.5 brings the result

$$P_{Ga} = 2P_{As_2} = \left(2K_{GaAs}^2\right)^{\frac{1}{3}} \tag{4.7}$$

This corresponds to congruent sublimation of GaAs. When the temperature increases over a certain temperature T_{max}, the pressure of the more volatile com-

Compounds	$K_{III/V}$	$T_{max}(^{\circ}C)$
GaAs	$2.73{\cdot}10^{11}\exp\left(-\frac{4.72}{k_BT}\right)$	630
InAs	$7.76{\cdot}10^{11}\exp\left(-\frac{4.43}{k_BT}\right)$	508
AlAs	$1.63{\cdot}10^{10}\exp\left(-\frac{5.39}{k_BT}\right)$	902

Table 4.1: material dependency of growth temperatures

ponent, in this case arsenic, increases faster and there will be no minimum in the region 1. Under this condition, a liquid gallium phase is created. The temperature T_{max} is called "temperature of maximum sublimation". T_{max} is calculated imposing P_{Ga} from equation 4.7 equal to the value of the gallium pressure over the liquid gallium. Table 4.1 indicates T_{max} and $K_{III/V}$ for the compound materials that are used in this thesis.

A short look to this table intuitively motivates the next two chapters. The effect of post growth annealing on shape and ordering of InAs/GaAs quantum dots is investigated. To enable efficient material mobility for the quantum dot growth (see next paragraph) the temperature is kept high. For InAs the table indicates the high limit at $T_{max} = 508(^{\circ}C)$. The temperature chosen for this study was $T = 500(^{\circ}C)$ which is slightly below $T_{max} = 508$. The very high value of $T_{max} = 902(^{\circ}C)$ in case of AlAs already gives a hint why AlAs can be used as diffusion barrier. Once one quantum dot layer is grown, the sample must be kept at growth temperature in order to grow the subsequent layers. During this time the already grown layer risks to be affected by thermal diffusion. Small barriers of AlAs at the material interface can avoid or reduce the interdiffusion. Another aspect of using AlAs is studied in chapter 4.2.3. Here the reduced material mobility of AlAs compared to GaAs leads to smaller quantum dots and reduces strain relaxation (see following chapters).

Quantum Dot Growth

In the previous paragraph the conditions, e.g. temperature and pressure, that are necessary to deposit solid InAs, AlAs or GaAs on the substrate, were drafted. All quantum dots in this thesis were grown on GaAs(001). The lattice parameter and band gap of Indium- Aluminum- and Gallium arsenide are listed in table 4.2.

It is visible in table 4.2 that AlAs and GaAs have very similar lattice parame-

Compounds	lattice parameter[Å]	band gap [eV]
AlAs	5.662	2.16
GaAs	5.6532	1.42
InAs	6.0583	0.35

Table 4.2: lattice parameter and band gap

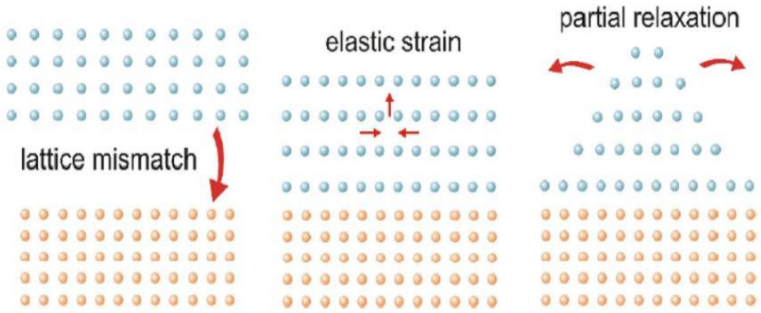

Figure 4.2: The epitaxy condition forces the lateral lattice parameter of the film and the substrate to adapt leading to tetragonal distortion. After the growth of a critical thickness, 3D islands start to form. source: ref. (97)

ter, while InAs differs by approximately 7% from GaAs. It becomes immediately clear that elastic energy is induced into the system, if InAs is epitactically grown on GaAs. This elastic energy can be reduced by reorganisation of the material, for example by the growth of Quantum Dots (see (10, 23, 41, 80)and figure 4.2).

On one hand the formation of the dots reduces the elastic energy that resulted from the tetragonal distortion, on the other hand the formation of dots brings new surfaces and edges into the system. The total elastic energy is therefore given by (66):

$$E_{tot} = E_{relax} + E_{surf} + E_{edge} \tag{4.8}$$

The formation of quantum dots reduces the first term E_{relax}, changes the second, and increases the third. The final equilibrium shape of quantum dots was calculated in the past (38, 56, 62, 66, 91). It is important to state that the equilibrium shape is usually not reached. Several constraints, such as material mobility, time, surface properties of the substrate, etc., cause variations to the equilibrium shape. A sequence of shapes adapted to the stepwise deposition of

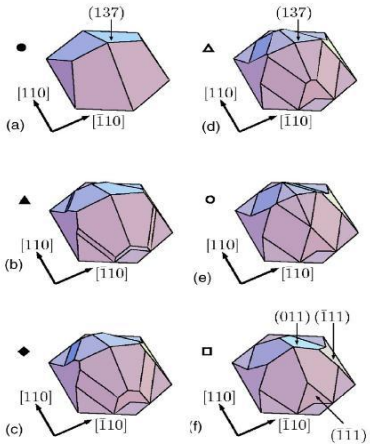

Figure 4.3: Proposed sequence of shapes for the growth of InAs quantum dots on GaAs(001) by Kratzer et al. Small quantum dots (a), are bounded by {137} and $\{\overline{111}\}$ facets. Growth proceeds mostly through layer-by-layer growth on the {137} facets; however, the newly grown layers do not make contact with the (001) substrate (b). As a result, {110} and {111} facets develop at the lower end of the added layers, giving the quantum dot an increasingly steeper appearance (c)(e) (66).

material was suggested in (66)(see figure: 4.3).

In the next chapter the transition of shape, strain and positional ordering during post growth annealing is experimentally studied.

4.2 Effect of Post Growth Annealing on Shape and Ordering

The effect of post growth annealing (79) is investigated comparing two InGaAs Quantum Dot samples. The growth and the AFM characterization were done by the group of Daniel Schaadt at the University of Karlsruhe. The x-ray scattering and diffraction measurements and analysis is part of this thesis. According to the short growth theory one expects that the quantum dots undergo change during post growth annealing, that intends to reduce the energy in the system. According to the predictions (figure 4.3) a trend towards more facets is expected. However, other effects, such as positional ordering contribute to the strain minimization and are therefore investigated. The results are also published in (75).

Self organization phenomena of positional correlation of QDs are usually stud-

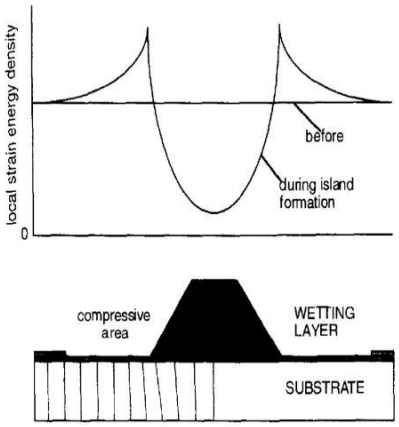

Figure 4.4: Visualization of the deformation of lattice planes due to strain in and around a 3D island. The corresponding local strain energy density at the surface before and during formation of the islands is shown schematically at the top figure. (88)

ied in *multilayers* where strain driven ordering occurs progressively during the multilayer growth.
In case of InGaAs QDs on GaAs(001) two different ordering types were found so far. The first type is a one dimensional (1D) two fold symmetric arrangement in chains elongated along $[1\bar{1}0]$ (100). The second type is a two dimensional (2D) four fold symmetric arrangement along the [100] and [010] axis (84). In case of InGaAs QDs on (311B) substrates two analogue types of correlation have been observed (28, 102). For quantum dot multilayer structures several publications report a transition from one to the other correlation type. This transition in the multilayer parameter space could be achieved by changing the substrate surface orientation (83), the spacer layer thickness (102) and the number of layers (84).

The effect of self ordering is most commonly explained by interplay of several factors such as crystallographic orientation, structure and temperature of the substrate, vertical and lateral material transfer (growth rate, in-plane mobility of ad-atoms) and several multilayer parameters.
The key mechanism of self-organization is usually attributed to the anisotropic elastic forces between the dots. The strain field induced by the QDs inside the surrounding host material was highlighted several times as driving force for positional correlation (24, 30, 92, 101). Ordering helps to minimize the strain mediated elastic interaction energy between neighboring islands.
Clearly the multilayer sequences supports the ordering. However, already for

single layer of InGaAs QDs on GaAs(001) ordering phenomena (84) have been reported. The conditions fostering the occurrence of ordering already in the first layer therefore gain interest.

The present work studies shape and ordering for the case of single layer InGaAs QDs on GaAs(001). We report the evolution of shape and ordering during post growth annealing. The study combines atomic force microscopy and strain and shape sensitive x-ray methods to gain insight into the mechanism of ordering.

sample preparation

The samples were prepared in a Riber 21 compact molecular beam epitaxy system. Epiready GaAs(001) substrates were degassed at 150°C for 1 h in a load lock chamber. Oxide desorption was carried out by keeping substrates at 600°C for 20 min under constant As_4 flux. The 2x4 surface reconstruction was clearly observed in the reflection high-energy electron diffraction pattern. A 250 nm thick GaAs buffer layer was deposited at 570 °C, followed by the deposition of 2.1 monolayer (ML) InAs at 500 °C. The growth rates of GaAs and InAs are 0.44 and 0.068 ML/s, respectively. Two samples are compared: One sample stayed unannealed, since it was rapidly cooled to room temperature. The other sample was kept at growth temperature for 5 min under constant As_4 flux and then rapidly cooled. After removal from the ultra-high vacuum (UHV) system the samples were covered with protective photo resist.

X-ray measurement set up

X-ray scattering measurements were performed with synchrotron radiation at the ESRF beamlines ID10B and ID01, and the ANKA beamline SCD. Shortly before starting measurements the photoresist was removed and the samples were placed inside a protective environment. Grazing incidence small angle scattering (GISAXS) was carried out at a wavelength of λ=1.53 $\AA$, making use of a position sensitive line detector in combination with a Si(111) analyzer. Grazing incidence diffraction (GID) was performed at λ=1.5028 $\AA$ based on a micro focused incident beam (1.2 $\mu m \times 2.5 \mu m$) and recording the diffraction pattern by a two dimensional CCD detector. This arrangement ensured quite fast data recording with sufficient resolution.

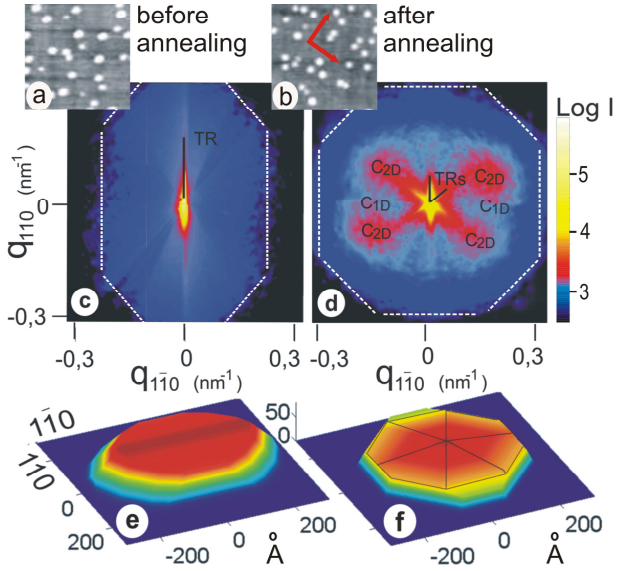

Figure 4.5: The two color maps (c) and (d) display the measured in-plane GISAXS data of the corresponding samples before (a) and after annealing (b) (α_i=0.7° and 0.8°). Atomic force micrographs (500x500 nm^2) show real space images of the QDs (a) before and (b) after annealing. The red arrows in (b) indicate the direction of QD positional correlation. The 3D models propose the shape of the QDs (e) before and (f) after annealing.

AFM results

The AFM analysis reveals that the density of the dots decreased considerably from 92 μm^{-2} to 56 μm^{-2} after annealing, while the size decreased slightly from 56 nm to 48 nm. The average height also decreased from 7.5 to 5 nm. That confirms the expectations from literature, where coarsening of dots has been observed at the beginning of annealing treatment while after critical annealing time a decrease in height and radius occurs due to enforced indium desorption (31, 67). Within the accessible scanned area of a 5x5 μm^2 AFM image, the Fourier Transform (FT) analysis did not display any clear positional correlation, neither before nor after annealing.

X-ray Results

Figure 4.5 shows two color maps (c) and (d) of the measured in-plane GISAXS intensity distribution in reciprocal space. The maps are achieved by projecting the measured 3D intensity distribution onto the $q_{110}/q_{1\bar{1}0}$ plane. All relevant scat-

tering contributions can be depicted by projecting along q_{001} the interval from 0.4 nm^{-1} to 0.75 nm^{-1}. Thereby enhanced diffuse scattering at the Yoneda wings ($\alpha_f = \alpha_c$) is included and the coherent specular reflection peak ($\alpha_f = \alpha_i$) is excluded (where α_i,α_f and α_c are the incident and exit angles and the critical angles of total external reflection). The reader may notice the logarithmic scale of the color maps.

Three main features can be observed in the GISAXS pattern. Side facets of QDs generate truncation rods (TR). The yellow shafts in the center of the maps are projections of that TRs onto the $q_{110}/q_{1\bar{1}0}$ plane. The clouds of diffuse scattering (blue areas indicated by the dashed lines) contain the squared FT of the QD shape. From the symmetry of the clouds we can conclude on the symmetry of the QD shape in real space. Positional correlation of QDs cause characteristic features of enhanced diffuse scattering intensities (visible in red in the image (d) of figure refGISAXmitAFM, which are related to the covariance functions of the scattered wave amplitudes (95).

In image (c) TR projections of two side facets are clearly visible, while six TRs of side facets appear after annealing (d). The in-plane directions of the TRs in reciprocal space directly indicate the crystallographic orientation of the corresponding QD side facets. The full 3D analysis resulted in $(119), (\overline{1}\overline{1}9)$ faceted dots before (e) and $(117), (\overline{1}17), (107), (\overline{1}07), (017), (0\overline{1}7)$ faceted QDs after annealing (d). Appearance of {117} facets after post growth annealing at 500°C was reported recently (67). The substrate TR contributes only to the central intensity spots as it is oriented perpendicular to the plane of projection.

The blue cloud in (c) is elongated if compared to (d). That is a fingerprint of the elongated base along $[1\bar{1}0]$ in case of the non-annealed QDs. Elongated shaped dots are typical for this material system. The reason for this shape asymmetry is the different surface diffusion length along the [011] and the $\left[1\bar{1}0\right]$ direction due to surface reconstruction (84). In case of the annealed sample (panel d), the blue cloud in the GISAXS pattern has the shape of a rounded octagon. No essential difference between the extension along the $[1\bar{1}0]$ and the [110] direction exists anymore. Thus it can be concluded that the annealing procedure gave time to compensate the limited diffusion length in the [011] direction and therefore the base shape of the dots became more symmetrical.

The non-annealed sample (c) does not show any positional correlation, while four correlation peaks C_{2D} positioned along [010] and [100] are clearly identified in

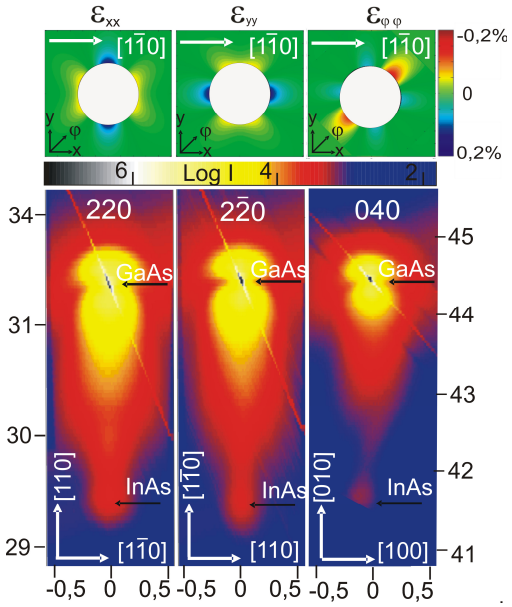

Figure 4.6: Upper part: continuum elasticity modeling (CEM) of the strain around a Quantum Dot. Three components of the strain tensor $\epsilon_{xx}, \epsilon_{yy}$ and $\epsilon_{\varphi\varphi}$ are plotted. The coordinates x,y,φ correspond to the crystallographic directions $[1\bar{1}0][110]$ and [010]. Lower part: GID measurements around the $[2\bar{2}0]$, [220] and [040] reflection. ($\alpha_i = 0.35°$)

case of the annealed sample (d). The distance between opposite peaks is 0.34 nm^{-1}, which corresponds to 37 nm correlation length in real space and reveals a close neighboring as it is also confirmed by AFM. Even if all positions of the correlation peaks are slightly compressed toward the C_{1D} direction, the findings give evidence for dominant 2D dot-dot ordering.

Interpretation - Shape and Ordering

The strain field around dots is determined by both, the elastic properties of the host crystal and the shape of the dot. The elastic property of bulk GaAs has a four fold symmetry in the (001) plane. In ref.(84) it was shown that in case of elongated dots the shape contribution is different along $[1\bar{1}0]$ and along [110]. Therefore the symmetry of the strain field around the dots is reduced from four fold to two fold, explaining the finding of two fold symmetric correlation for such structures.

The measurements give clear evidence for the formation of a dominant four fold symmetric correlation type after annealing. Simultaneously we observe dots with

rounded octagonal bases. Thus the shape contribution to strain is nearly identical in both, the [110] and [1$\bar{1}$0] direction, and the symmetry of the strain field around the dots is close to be four fold, as expected from the elastic properties of InAs and GaAs for (001) substrate.
The results of analytical strain simulation in upper part of figure 4.6 illustrate that symmetry. There the strain field around a dot with a round base has been calculated based on a continuum elasticity model (CEM) (1). It can be seen that for elastically equivalent [110] and [1-10] directions the corresponding strain components ϵ_{xx} and ϵ_{yy} are complementary, corresponding to a four fold symmetric lattice displacement field.
The GID measurements in figure 4.6, lower part, confirm this behavior, since we measured nearly identical intensity distributions in the reciprocal space maps around the [220] and [2$\bar{2}$0] reflections. Comparing the CEM calculations of the strain component $\epsilon_{\varphi\varphi}$ (oriented along [010]) to the previous, we find strong differences. And, in accordance to that, the GID intensity map around the [040] reflection differs strongly from the maps around [220] and [2$\bar{2}$0] and (all maps are normalized by structure factors).

We may conclude that the four fold symmetry of the strain field is responsible for the generation of the four fold symmetric correlation of the dots, which became visible in the GISAXS measurements (figure 4.5 d). The favorite directions of alignment are the elastically weak [010] and [100] directions. The observed small compression of the correlation pattern away from the [100] /[010] correlation directions is possibly caused by residual effects from surface dynamics (63, 77, 78, 90).

Conclusion

In summary four fold symmetric 2D lateral ordering of QDs after post growth annealing is found while no ordering can be seen for the non-annealed QDs. Concluding, ordering phenomena as already observed for growth close to thermodynamic equilibrium can also be achieved by growth away from thermodynamic equilibrium and subsequent post growth annealing. Elongated shape of dots, as shown recently (84), may cause the 1D (two fold symmetric) correlation type, while dots with higher symmetric bases allow to form 2D (four fold symmetric) ordering. Post growth annealing may transform the dot shape from elongated to round and therefore may represent a possibility to favor either the 1D or the 2D

correlation type.

4.3 Effect of Chemical Composition on Shape Ordering and Light Emission

For this study $In_{0.6}Ga_{0.4-x}Al_xAs$/GaAs(001) QDs were grown. Sample by sample the gallium content was gradually replaced by aluminum. In table 4.2 it can be seen that gallium and aluminum have nearly the same lattice parameter and they also have very similar elastic properties. From this point of view exchanging one by another should not change the equilibrium (energetic minimum) shape of the dots. The band gap of AlAs (2.16 eV) is considerably larger than the one of GaAs (1.42) and a shift in the light emission wavelength is expected. In the following study a series of $In_{0.6}Ga_{0.4-x}Al_xAs$/GaAs(001) QDs with aluminum contents of x=0, 0.08, 0.12, 0.17 and 0.19 is investigated. The study combines scanning electron microskopy (SEM), photo luminescence (PL) and x-ray measurements (GISAXS and GID). The sample growth, the SEM and the PL measurements were performed by the collaboration partner, the group around Sven Höfling and Thomas Schlereth (Optoelectronic Materials and Devices I, Universität Würzburg). The corresponding results are published by Schlereth et al.(81). The x-ray measurements and analysis are part of this thesis. An "x-ray publication" is in progress (57).

Sample Growth

All samples were grown by solid source molecular beam epitaxy (MBE) on (100) oriented GaAs substrates. The sample structure consists of a 200 nm GaAs buffer layer, followed by a 200 nm $Al_{0.4}Ga_{0.6}As$ barrier layer, on which 4.9 ML of $Al_xGa_{0.4-x}In_{0.6}As$ was deposited for QD formation. The QD layer was overgrown by another 200 nm $Al_{0.4}Ga_{0.6}As$ barrier layer and the sample was finished with an uncapped QD layer, nominally identical to the buried one. The QD layer was grown in several submonolayer cycles of consecutive $Al_{0.29}Ga_{0.59}In_{0.12}As$, $Ga_{0.83}In_{0.17}As$ and InAs depositions via controlling the shutter time of the corresponding effusion cells. Between each cycle a growth interruption of 10 s was introduced to enhance the surface migration ability of the deposited elements. AlAs, GaAs and InAs growth rates of 0.5, 1.0 and 0.2 μm/h were chosen. The samples were grown at a substrate temperature of 570°C. For the QD layer de-

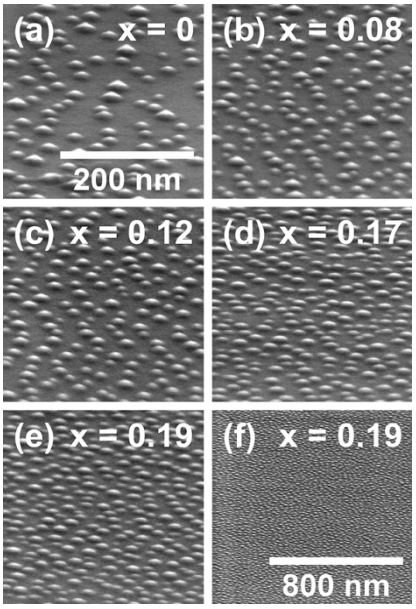

Figure 4.7: ((a)(e)) SEM images of uncapped $Al_xGa_{0.4-x}In_{0.6}As$ QD samples with a nominal Al content x of (a) 0, (b) 0.08, (c) 0.12, (d) 0.17 and (e) 0.19. (f) An SEM image showing the same sample as in (e) with lower magnification. The surface is tilted by 70°. to enhance the height contrast. source: ref. (81)

position the temperature was lowered to 520°C. Samples with $Al_xGa_{0.4-x}In_0.6As$ QDs of different compositions x=0, 0.08, 0.12, 0.17 and 0.19 have been fabricated.

SEM Results - Real Space Images

In figure 4.7 SEM images of the uncapped $Al_xGa_{0.4-x}In_{0.6}As$ QD samples with a nominal Al content x of 0, 0.08, 0.12, 0.17 and 0.19 (figure 4.7) are displayed. It can easily be seen that the QD surface density significantly increases with increasing Al content, whereas the average QD diameter decreases. By raising the Al content x from 0 to 0.19, the QD density increases almost by a factor of 3 from 3.91010 to 1.11011 cm^{-2}, and the average QD diameter decreases from 23 to 16 nm. This very dense QD layer is homogeneous on the whole sample, as can be seen from figure 4.7 (f), which shows a larger area of the sample (4 m^2).

GISAXS Results - Size, Shape and Ordering

Figure 4.8 depicts the SEM images together with in-plane GISAXS measurements. The blue cloud reveals the FT of the QD shape as explained in the theoretical

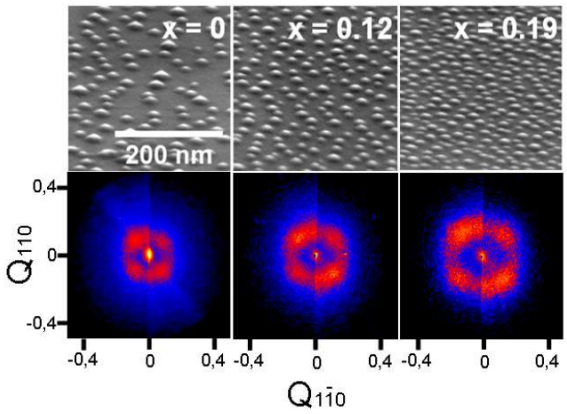

Figure 4.8: (ae) SEM images of uncapped $Al_xGa_{0.4-x}In_{0.6}As$ QD samples with a nominal Al content x of (a) 0, 0.12 and 0.19. Below, the corresponding in-plane GISAXS images are shown. The QD size decrease in the real space SEM images is reflected in an size increase of the reciprocal space picture.

part. The decrease in size of the dots in real space corresponds to an increase in the size of the corresponding features in reciprocal space. The symmetry of the blue clouds are similar comparing all three cases. From left to right they seem scaled up, but the characteristic picture remains the same. This means that the round QD shape is similar in all cases, just the size decreases with increasing Al content. Furthermore, the shapes of the blue clouds resemble the measurements of the post growth annealed sample in the previous paragraph. The same close to elastic energy minimized equilibrium shape can either be reached by growth interruptions (10 seconds between each cycle in this example) or by post growth annealing treatment as in the previous paragraph.

The most interesting part of the in-plane GISAXS study might be the investigation of positional correlations of the quantum dots. The red rings inside each GISAXS map reveal these correlations (see GISAXS introduction). All rings contain peaks with enhanced intensities along the [100] /[010]directions. This means that exactly the same correlation directions as for the post growth annealed sample in the previous chapter are found. In the post growth annealed case the correlation directions were explained by shape induced strain driven ordering. The present findings in this chapter confirm this concept. As these samples have a similar shape as the post growth annealed sample in the previous chapter, also the strain field around the dots inside the substrate is similar concerning its sym-

metries. As consequence, the same ordering type, namely ordering along the [100] /[010]directions, has to occur. Comparing the dots with different Al content it was stated that the shape is similar in terms of symmetry, but the absolute size is different. Consequently the directions of ordering are the same, independent of the Al content, but the characteristic distances are different. As the dots are scaled up or down in size depending on the Al contend, also the strain field around the dots scales up in its dimensions. This leads to different characteristic distances, which is perfectly visible in the GISAXS maps. The red rings have the same symmetry in all cases showing peaks at the [100] /[010] directions, but the radii of the rings are systematically increasing from left to right indicating decreasing characteristic distances from 54 nm over 41.9 nm to 31,2 nm.

GID - Strain and Chemical Composition

In the previous paragraph the shape and positional ordering in dependence of the Al concentration was investigated. Conclusions on the strain around the quantum dots inside the substrate could be derived. In this paragraph the strain inside the quantum dots as well as the chemical composition and its distribution inside the dots is investigated. On the one hand this will contribute to the explanation of the emission wavelength in the next paragraph, on the other hand the strain investigation enlightens the growth mechanism and therefore delivers explanations for the different QD sizes found just in the previous paragraph.

The analysis of the GID measurements was done with the new express method that is proposed in this thesis and described above. Nevertheless the main ideas should be quickly repeated in order to relate intuitively the measurements in figure 4.9 with the results in figure 4.10. On the first look one sees that the middle GID picture for the x=0.08 sample differs from the two others in terms of background intensity and length of the Ewaldsphere streak. The reason is the different measurement configuration. The x=0.08 image was taken in the parallel-beam-plus-analyzer-configuration leading to higher signal to noise sensitivity and supresion or air scattering. One advantage of the express analysis is that all these measurement artifacts do not need to be considered. The only parameters that are extracted are the position and curvature (not even the intensity!) of the first order shape scattering maximum, indicated with the white dashed lines (figure 4.9). The width between the left and the right arc along Q_{ang} indicates the

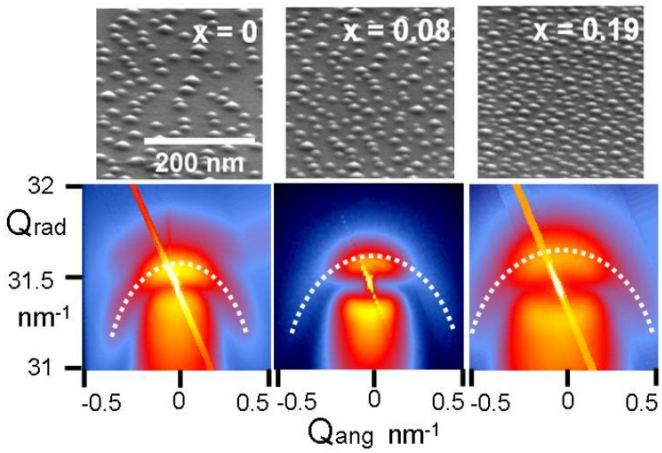

Figure 4.9: SEM and GID images for the samples with an Al content of x=0, 0.08 and 0.19. The middle one was measured in the parallel-beam-plus-analyzer-configuration (see 4.1.1), the other two GID images are taken with focused-beam-plus-2D-detector configuration. The white lines indicate the first order shape scattering maximum. In case of the x=0 sample the second order shape scattering maximum is also visible.

diameter (inverse proportional) of the ISA, the position of a certain point along Q_{rad} indicates the lattice parameter. The decrease of the QD size from sample to samplke (from the left to the right image) is visible in figure 4.9). The slope of the white line can be understood as a measure of strain gradient. The complete analysis was done for three of the five samples and resulted in the models in figure 4.10.

Figure 4.10 displays the FEM models, for which the $a(D)$ profiles correspond best to the measurement. It is visible that the QD size decreases from 29 nm over $24,5$ nm to $22,5$ nm. Indium is concentrated in the upper part of every QD in higher concentrations than the nominal value of 60% that follows from the deposition rate. Differences between the three samples are seen at the bottom, where the Indium concentrations are lower, especially in case of small Aluminum contents. This might be surprising since the nominal Indium concentration was kept constant in all 3 cases. The observations can be explained as follows: The replacement of Ga by Al does not appear in the FEM models, since AlAs and GaAs have very similar lattice parameters and elastic properties. Replacing one by the other does not affect the strain, if all other parameters are constant (81). However, during deposition Al changes the material mobility. The bond strength of Al to As is about 25% higher than the one of Ga to As (81). More Aluminum

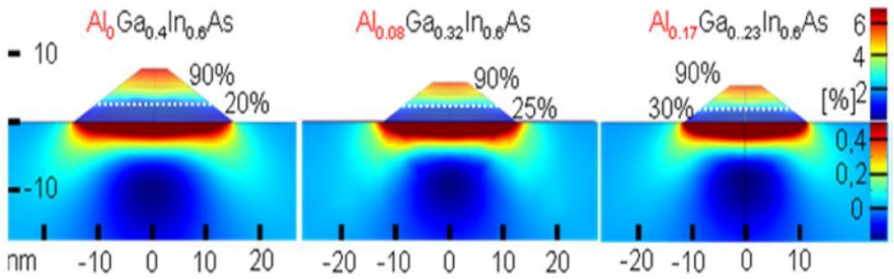

Figure 4.10: FEM data indicating the lattice parameter relative to the substrate for the three samples with different nominal Al concentrations (x=0, 8 and 17%). Please notice the different color scale bars for the dot and the substrate.
Even if the nominal Indium concentration is 60% in all cases, a material redistribution inside the dots is visible. The models distinguish a bottom part with smaller and a top part with higher Indium concentrations. From left to right a decrease in size and an increase in the Indium concentration at the bottom is visible.

therfore reduces the surface migration ability. As a consequence the dots grow less in size and the diffusion of AlAs/GaAs inside the dot is reduced. The In concentration thus remains higher in this case. The first effect, the reduction of size, was already described in (81). Concerning the chemical composition, however, we find little differences between the samples, especially between the $Al = 0\%$ sample and the others. So far the previous assumption of identical strain and composition in all cases can be refined. This might forward the interpretation of different light emission wavelenghts.

PL - Light Emission

The photoluminescence (PL) measurements were performed by the collaboration partner, the group around Sven Höfling and Thomas Schlereth (Optoelectronic Materials and Devices I, Universität Würzburg) before the beginning of this thesis and they are published in (81). The results are discussed here as they are in direct relation with the results of the x-ray investigation.

Figure 4.11 displays the results of the low temperature photoluminescence measurements. It is visible that the emission wavelength decreases with increasing Al concentration, if the In concentration is kept constant. Lower In concentrations also lead to a decrease in emission wavelength. As mentioned already the light

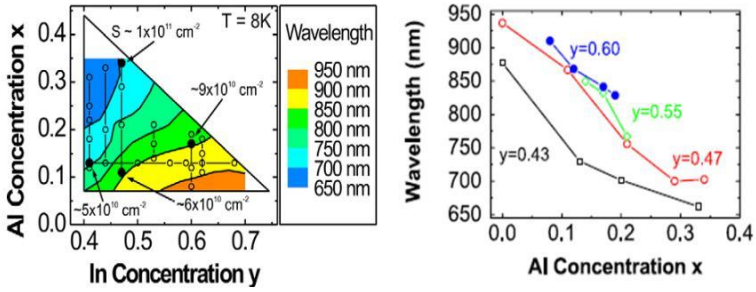

Figure 4.11: Left: Interpolated contour plot of the PL wavelength (T = 8 K) for samples with different In and Al concentration. The samples with an Indium content of 0.6 and different Al contents are the samples that are investigated with x-ray methods in this thesis. The open circles show some data points used to create the figure and the way they where acquired. Some data points (filled circles) are labeled with their corresponding QD surface densities to show, how the QD density can be tailored for a chosen emission wavelength. The triangular border represents the boundaries of the accessible In and Al concentrations. For the blank spots in the triangle not enough data points for an interpolation have been available. Right: Low temperature (8 K) PL emission wavelengths of $Al_xGa_{1-x-y}In_yAs$ QD samples with different Al and In concentrations. Source: (81)

emission of semiconductor quantum dots is dependent on the natural emission wavelength E_{gap} of the composite material, the strain inside E_{strain} and the size of the quantum dot due to quantum mechanical confinement E_{conf}. In (81) a simple model is used, that assumes that the transition energy of the QDs can be treated as the sum of these three factors:

$$E_{emission} = E_{gap} + E_{strain} + E_{conf} \tag{4.9}$$

For a quaternary alloys like $Al_xGa_{1-x-y}In_yAs$ the first term is calculated (34) according to:

$$E_{gap} = 1.519 + 1.36x - 1.584y + 0.55xy + 0.22x^2 + 0.475y^2 \tag{4.10}$$

The second term is the contribution of strain to the bandgap. The relationship between strain and bandgap is described in (13). The energy shift due to strain is approximated by the energy shift of the heavy hole band (E_{HH}), which is given by:

$$\Delta E_{strain} \approx \Delta E_{HH} = H - S \tag{4.11}$$

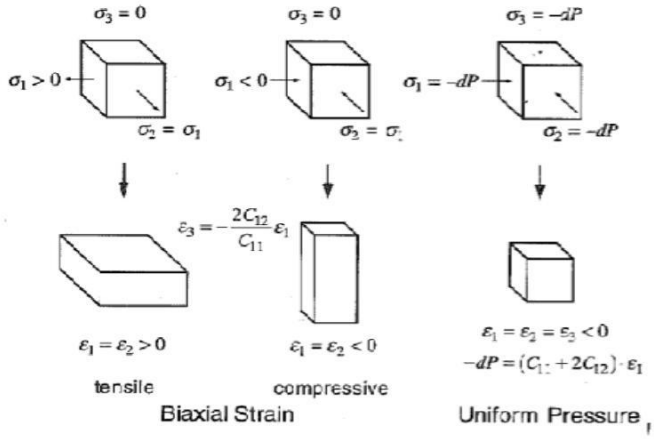

Figure 4.12: Example of the relation between stress and strain. Source: (13)

whereby H and S are related to the strain tensor through the a and b deformation potentials (see table 4.3). H is proportional to the change in volume of the crystal lattice created by strain. The shear strain energy S is proportional to the asymmetry in the strain parallel and perpendicular to the stress plane.

$$H = a \cdot (\epsilon_1 + \epsilon_2 + \epsilon_3) \tag{4.12}$$

$$S = b \cdot (\frac{1}{2}(\epsilon_1 + \epsilon_2) - \epsilon_3) \tag{4.13}$$

The epitactical growth of alloys on a substrate usually leads to biaxial strain due to the lattice mismatch (see figure 4.12) and one can write:

$$\epsilon \equiv \frac{a_{native} - a_{sub}}{a_{native}} \tag{4.14}$$

and

$$\epsilon_1 = \epsilon_2 = -\epsilon \tag{4.15}$$

$$\epsilon_3 = \frac{2C_{12}}{C_{11}}\epsilon \tag{4.16}$$

whereby a_{native} is calculated according to Vegard's law. Together with the values from table 4.3 E_{strain} can finally be calculated.

Compounds	Lattice Constant Å	a [eV]	b [eV]	C_{11} $[10^{11} dyn/cm^2]$	C_{12} $[10^{11} dyn/cm^2]$
GaAs	5.6533	-8.68	-1.7	11.88	5.38
InAs	6.0583	-5.79	-1.8	8.329	4.526
AlAs	5.6611	-7.96	-1.5	12.02	5.70

Table 4.3: Strain parameter in III-V semiconductors. Source: (13)

In (%)	Al (%)	Lat. size d (nm)	height h (nm)	E_{gap} (eV)	E_{strain} (eV)	E_{conf} (eV)	$E_{calculated}$ (eV)	$E_{measured}$ (eV)
60	8	19,2	5,6	0,886	0,145	0,157	1,188	1,362
60	17	15,7	5,3	1,033	0,145	0,158	1,336	1,473

Table 4.4: calculated and measured emission wavelength for the QD samples with Al content of x=0,08 and x=0,17. Homogeneous material distribution inside the DQs corresponding to the nominal deposition rates was assumed for the calculations. source: (81)

The third and last term in equation 4.9 is the contribution from the quantum confinement E_{conf}. The following equation shows the relationship between energy level and dimension spacing:

$$E_{n_x,n_y,n_z} = \frac{\hbar^2 \pi^2}{2m} \left[\left(\frac{n_x}{L_x} \right)^2 + \left(\frac{n_y}{L_y} \right)^2 + \left(\frac{n_z}{L_z} \right)^2 \right] \tag{4.17}$$

The Energy values for the 3 different QD samples are listed in table 4.4. As expected, the wavelength decreases strongly with increasing Al concentration. The interpretation is twofold: Firstly the incorporation of Al into the QDs increases the separation of the energetic levels of electrons and holes in the QD by increasing the natural bandgap E_{gap}. Secondly the QD dimensions are changed with impact on the confinement E_{conf}. The trend is reproduced in the calculated data. However, the calculated emission wavelength is approximately 10% too low (81).

Here one has to mention that the calculation in table 4.4 assumes that the material is homogeneously distributed inside the quantum dots and the chemical composition is equal to the nominal values following from the deposition rates. The results of the GID measurements in figure 4.10 show at least for Indium a

In (%)	Al (%)	Lat. size d (nm)	height h (nm)	E_{gap} (eV)	E_{strain} (eV)	E_{conf} (eV)	$E_{calculated}$ (eV)	$E_{measured}$ (eV)
25	8	19,2	5,6	1,274	0,045	0,157	1,476	1,362
30	17	15,7	5,3	1,352	0,048	0,158	1,558	1,473

Table 4.5: Calculated and measured emission wavelength for the QD samples with Al content of x=0,08 and x=0,17. The values for the Indium concentration and the strain are taken from the GID measurements.

clearly inhomogeneous material distribution inside the dots. High concentrations of Indium are found at the top of the dots, while lower ones are found at the bottom. These results confirm a strain minimizing material redistribution, that was several times observed in case of other QD systems (27, 35, 87). These changed Indium concentrations influence dramatically the emission wavelength. The top of the quantum dot with 90% Indium would not emmit visible light at all. The emission wavelength for the bottom part are calculated in table 4.5.

The values for the Indium concentration in table 4.5 are taken from the GID results (see figure 4.10). The changed Indium concentration has two effects: E_{gap} changes due to different semiconductor material composition and also E_{strain} is changed. The lowering of the strain contribution can intuitively be understood: The driving force for the material redistribution inside the quantum dot is the minimization of strain energy. Therefore the final QD strain has to be lower than the strain in a theoretical QD with homogeneous material distribution.
One can see that the values for the emission wavelength that are based on the QD properties found with the x-ray investigation, match better to the measured emission wavelength than the calculated emission wavelength deduced from the nominal composition values. It becomes clear that the material redistribution inside the quantum dots contributes essentially to the value of the emission wavelength, even more than the confinement effect. However, one important limitation of the present x-ray study has to be mentioned. The QDs that were investigated are free standing QDs. For the PL measurements the dots have to be overgrown. It was shown that this changes the shape and the chemical distribution (21). Therefore it is approximative to conclude from the free standing dot properties on the emission of the dots after overgrowth. In this context the methodical development, that was done in this thesis, may become important. It was shown that

the method detects iso strain areas underneath the dot inside the substrate. The reason was the sharp strain gradient at the edges of the buried iso strain areas, that give rise to shape oscillations. In the same manner one can expect shape oscillations from buried Quantum dots. This means that the proposed method may be applicable to buried QDs. In this way the QDs could be investigates in the same overgrown condition as they are when they emit light.

Conclusion

In summary a series of $In_{0.6}Ga_{0.4-x}Al_xAs/GaAs(001)$ quantum dots with changing Al content was investigated. For all dots a rather symmetrical round shape was found in GISAXS, revealing a condition close to the energetic minimum equilibrium shape. In the previous paragraph this equilibrium shape was achieved by post growth annealing, in this series many short growth interruptions seem to have a similar effect giving sufficient time and mobility to reach the energetic minimum. The concept of shape induced positional ordering of the dots discussed in the previous series was confirmed. The same energetic minimum shape that led to four fold symmetric dot ordering in the previous series again let to the same ordering type. Even more, the up and down scaling in dot-size resulted in up and down scaling of the characteristic dot to dot distances.
For the interpretation of the GID measurements the express analysis method, that was introduced in the previous paragraph could be applied. It revealed drastic material redistribution inside the dots compared to the nominal values. Again the strain and the strain minimization are the driving force for this inner material redistribution. The effect on the emission wavelength was calculated and discussed. Surprisingly, the redistribution of Indium inside the dots contributes more to the emission wavelength number than the confinement effect. The mechanism that is responsible for smaller sized dots in case of high Aluminum concentrations was confirmed by the GID measurements.

4.4 In-situ Experiments

The next milestone in the field of x-ray characterization of QDs is the in-situ experiment and the actual in-situ application of the express analysis method. For this purpose an in-situ UHV chamber, that provides UHV connectivity to growth chambers and further sample processing (annealing, overgrowth etc.) in

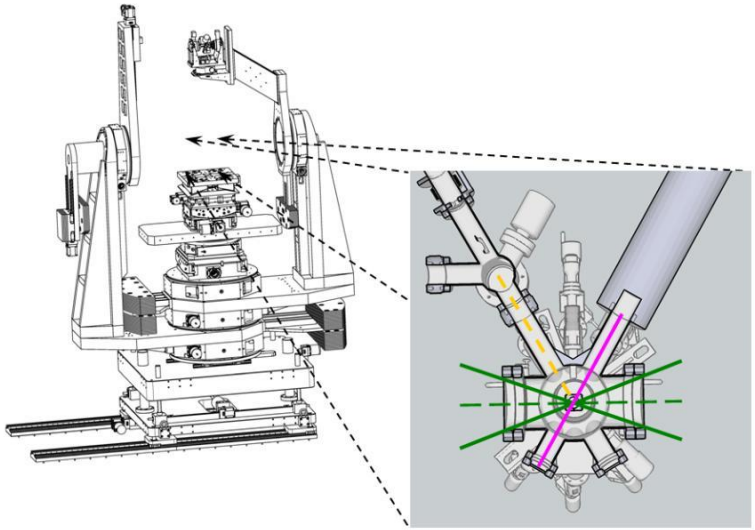

Figure 4.13: In-situ characterization stage at the ANKA synchrotron. The growth chamber (insert on the right) can be placed onto the diffractometer at the synchrotron beamline (e.g. at ANKA-Nano, ESRF ID03 or other) for in-situ x-ray measurements. The green lines on the right indicate the accessible angular range for the x-Ray beam, that was realized by two large beryllium windows. The possibility of UHV connection enables sample transfer to other growth chambers and a big number of complementary characterization methods, that are available for example in the neighbored UHV cluster.

isochronous combination with x-ray measurements, was designed at the institute (see figure 4.13).

First in-situ annealing experiments under arsenic atmosphere could be performed. InGaAs QDs were overgrown by 10 nm of GaAs and in-situ annealed at constantly increasing temperature. The red curves in figure 4.14 are *in-situ* data of these measurements. A right shift and a reduction of slope and curvature between the two temporal evolution points at T=235°C; t=50min (full circles) and T=423°C; t=112min (empty circles) is visible. Material inter diffusion leads to a blow-up of the buried ISAs and a reduction of the strain and the composition gradient.

In-situ applicability of the express method and the applicability to buried quantum dots could be shown. The detailed analysis and further in-situ experiments are projected as part of the PHD work of P. Schroth started in summer 2011.

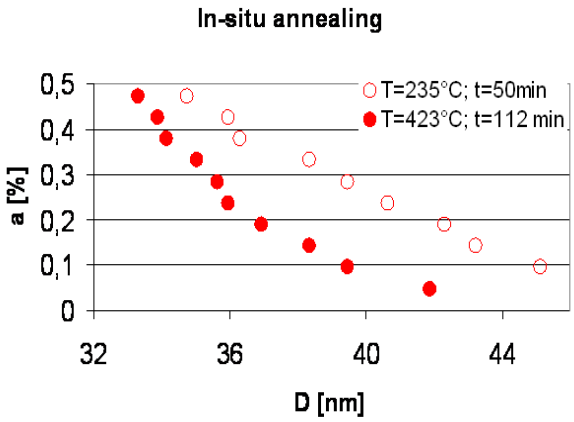

Figure 4.14: In-situ measurement at two different temporal evolution points. The circles reveal data directly extracted from selected areas along the first order shape scattering maxima. They indicate the lateral size D and the lattice parameter of the iso strain areas.

5 Discussion

The results of this thesis can be classified in two parts, a methodical development part, and a quantum dot characterization part. The aim of the methodical part was the development of an x-ray method for semiconductor quantum dot characterization which is simple, robust and in-situ applicable, but at the same time sufficiently precise to be technologically relevant. For this purpose the conventional iso strain scattering model was reviewed first. It was found that the iso strain approximation itself, i.e., the incoherent addition of the scattering responds of single iso strain areas, is sufficiently precise. However, the conventional ISS model leads to misinterpretations, in particular in the technologically important case of small dots, since an essential part of "key features" addressed by the ISS-model to the dot, is not generated by the quantum dots, but rather by strained regions outside the dot.
In order to overcome this limitation, a new holistic iso strain model, that includes iso strain areas in the dot as well as in the substrate, was developed. The model was verified on the basis of simulated data and later applied to real experiments. The functionality could be proofed on a sample series that was produced for a light emission study. These results are simultaneously part of the quantum dot characterization study. The in-situ applicability of the new method was exemplified.

In the second part of the thesis two quantum dot series were studied with conventional and with the new developed methods. In the first series the effect of post growth annealing on shape and ordering was studied. Four fold symmetric 2D lateral ordering of QDs after post growth annealing was found, while no ordering was seen for the non-annealed QDs. Hence, ordering phenomena as observed for growth close to thermodynamic equilibrium (second sample series) can also be achieved by growth away from thermodynamic equilibrium and subsequent post growth annealing. The concept of strain driven ordering that is mediated by the shape induced inter dot strain was clearly supported. An elongated shape of dots may cause a 1D (two fold symmetric) correlation type, while dots with higher symmetric bases allow to form 2D (four fold symmetric) ordering. Post growth

annealing may transform the dot shape from elongated to round and therefore may represent a possibility to favor either the 1D or the 2D correlation type.
The same type of shape and ordering which was found in the post growth annealed growth annealed sample has been observed for all samples in the second sample series. In this study multiple growth interruptions of 10 seconds guaranteed a condition of shape and ordering close to the thermodynamical equilibrium. The difference between the samples was the nominal content of Aluminum. A size reduction related to higher Al content already described by SEM measurements could be confirmed by the x-ray analysis. In addition, strain and internal chemical distribution of InAs could be measured by applying the new method that was developed in the first part of this thesis based on the HISS model. Instead of homogeneous material distribution corresponding to the nominal value (from deposition rate), higher concentrations are found at the top of the dots and lower ones at the bottom. The material redistribution and the related strain relaxation acts dramatically on the light emission wavelength. In fact, this effect is bigger than the often discussed confinement effect. Thus, the new developed analysis method contributed to a better understanding of the light emission and could reduce the discrepancy between the calculated and the measured emission wavelength.

The in-situ applicability of the new analysis method based on the holistic iso strain model was exemplified. For future in-situ studies the new developed method enables time resolved in-situ studies of quantum dots, for example at the ANKA synchrotron. First experiments are already in process.

The development of an holistic iso strain scattering model clarified the role of the substrate during scattering experiments. In future, this knowledge might not only serve in a simple, robust and in-situ applicable analysis method, but might also become an integral part of more complex and automatized analysis algorithms such as used for phase retrieval for example.

List of Figures

List of Tables

Glossary

AFM Atomic Force Microscopy

DWBA Distorted Wave Born Approximation

GID Grazing Incidence Diffraction

GISAXS Grazing Incidence Small Angle X-Ray Scattering

HISS Holistic Iso Strain Scattering

ISA Iso Strain Area

ISS Iso Strain Scattering

MBE Molekular Beam Epitaxy

ML Mono Layer

PL Photoluminescence

QD Quantum Dot

RSM Reciprocal Space Map

SEM Scanning Electron Microscope

STM Scanning Tunneling Microscope

TEM Transmission Electron Microscope

UHV Ultra High Vacuum

References

[1] A. A. Matyshev and E. Fohtung. *arXiv:0910.0365v1*, 2009. 87

[2] A.Lenz. *Phd thesis*, page Technische Universität Berlin, 2008. 2

[3] A. Autier. *Dynamical theory of X.Ray diffraction*. Oxford Uni. Press, 2001. 5

[4] L. V. Azaroff, R. Kaplow, N. Kato, R. J. Weiss, A.J.C. wilson, and R.A young. *X-ray Diffraction*. McGraw-Hill, 1974. 5, 10

[5] T. Baumbach and V. Holy. *Vorlesungsreihe*, page UNI Karlsruhe, WS 2008/2009. 17, 23, 103, 104

[6] T Baumbach and D. Lübbert. *J. Phys. D: Appl. Phys.*, **32**:726–740, 1999. 2, 6

[7] T. Baumbach, D. Lübbert, and M. Gailhanou. *J. Appl. Phys*, **87**:3744, 2000. 2

[8] T. Baumbach, Daniel Lübbert, and Marc Gailhanou. *Jpn. J. Appl. Phys.*, **38**:6591–6596, 1999. 2, 6

[9] T. Baumbach, D. Luebbert, and M. Gailhanou. *J. Appl. Phys.*, **87**:3744, 2000. 2

[10] D. Bimberg. *Semiconductor Nanostructures*. Springer, 2010. 1, 80

[11] D. Bimberg and M. Grundmann. *Quantum Dot Heterostructures*. John Wiley and Sons, 1999. 1

[12] G. W. Bryant and G. S. Solomon. *Optics of Quantum dots and wires*. Artech House, 2005. 1

[13] L. A. Coldren and S. C. Corzine. *Diode Lasers and Photonic Integrated Circuits*. Wiley, 1995. 94, 95, 96, 109, 111

[14] R. D. Cook. *Finite Element Modeling for Stress Analysis*. John Wiley and sons. 43

[15] GJ. Coraux, H. Renevier, M. G. Proietti, V. Favre-Nicolin, B. Daudin, and G. Renaud. *phys. stat. sol.*, **243**:15191523, 2006. 2

[16] J. M. Cowley. *Diffraction Physics*. North-Holland, 1975. 5, 10, 29

[17] A. S. Davydov. *Quantum Mechanics*. Pergamon Press, 1976. 9

[18] Internetseiten des Max Plank Instituts für Metallforschung. 33, 104

[19] H. Dosch, B. W. Batterman, and D. C. Wack. *Phys. Rev. Lett.*, **56**:1144, 1986. 21

[20] R. Feidenhans'l. *Surface Science Reports*, **10**:105–188, 1989. 21

[21] Fariba Ferdos, Shumin Wang, Yongqiang Wei, Anders Larsson, Mahdad Sadeghi, , and Qingxiang Zhao. *Appl. Phys. Lett.*, **81**:1195, 2002. 97

[22] J. R. Fienup. *Appl. Opt.*, **21**:2758, 1982. 2

[23] J. A. Floro, M. B. Sinclair, E. Chason, L. B. Freund, R. D. Twesten, R. Q. Hwang, and G. A. Lucadamo. *Phys. Rev. Lett.*, **84**:701, 2000. 80

[24] J. A. Floroand, E. Chason, M. B. Sinclair, L. B. Freund, and G. A. Lucadamo. *Appl. Phys. Lett*, **73**:951, 1998. 82

[25] M. Francardi, L. Balet, A. Gerardino, N. Chauvin, D. Bitauld, L .H. Li, B. Alloing, and A. Fiore. *Appl. Phys. Lett.*, **93**:143102, 2008. 1

[26] Bundesministerium für Bildung und Forschung. *Aktionsplan Nanotechnologie 2015*, page http://www.bmbf.de/de/nanotechnologie.php. 1

[27] D. Grigoriev, M. Hanke, M. Schmidbauer, P. Schäfer, O. Konovalov, and R. Köhler. *J. Phys. D: Appl. Phys.*, **36**:A225–A230, 2003. 76, 97

[28] M. Hanke, M. Schmidbauer, Zh. M. Wang, Yu. I. Mazur abd Sh. Seydmohamadi, G. J. Salamo, T. D. Mishima, and M. B. Johnson. *Appl. Phys. Lett*, **94**:203105, 2009. 82

[29] V. Holy, U. Pietsch, and T. Baumbach. *High resolution X-Ray scattering from Thin Films and Multilayers*. Springer Verlag, 1999. 5, 6, 8, 9, 10, 13, 18, 21, 28, 29, 30, 59, 103

[30] V. Holý, G. Springholz, M. Pinczolits, and G. Bauer. *Phys. Rev. Lett.*, **83**:356, 1999. 82

[31] D.Z. Hu, D.M. Schaadt, and K.H. Ploog. *Journal of crystal growth*, **293**:546, 2006. 84

[32] D.T.J. Hurle. *J. Phys. Chem. Solids*, **40**:613–326, 1979. 78

[33] J.A.Nielsen and D. McMorrow. *Elements of modern x-ray Physics*. Wiley, 2001. 5, 10, 12, 65

[34] J. R. Jensen, J. M. Hvam, and W. Langbein. *J. Appl. Phys.*, **86**:2584, 1999. 94

[35] I. Kegel, T. H. Metzger, A. Lorke, J. Peisl, J. Stangl, G. Bauer, J. M. Garca, and P. M. Petroff. *Phys. Rev. Lett.*, **85**:1694, 2000. 2, 6, 34, 97

[36] Ingo Kegel. *PHD thesis*, pages Ludwig–Maximilians–Universität München, 2000. 21, 34, 37, 38, 105

[37] Victor I. Klimov. *Appl. Phys. Lett.*, **89**:123118, 2006. 1

[38] P. Kratzer, A. Chakrabarti, Q. K. K. Liu, and M. Scheffler. *New J. Phys.*, **11**:073018, 2009. 80

[39] B. Krause, T. H. Metzger, A. Rastelli, R. Songmuang, S. Kiravittaya, and O. G. Schmidt. *Phys. Rev. B*, **72**:085339, 2005. 2, 6, 34, 76

[40] S. Labat, V. Chamard, and O. Thomas. *Thin Solid Films*, **515**:5557, 2007. 2

[41] D. Leonard, K. Pond, and P. M. Petroff. *Phys. Rev. B*, **50**:11687, 1994. 80

REFERENCES

[42] D. Litvinov, D. Gerthsen, A. Rosenauer, M. Schowalter, T. Passow, P. Feinugle, and M. Hetterich. *Phys. Rev. B*, **74**:165306, 2006. 2

[43] D. Lübbert, T. Baumbach, S. Ponti, U. Pietsch, L. Leprince, J. Schneck, and A. Talneau. *Europhys. Lett.*, **46**:479–485, 1999. 2

[44] R. Magalhaes-Paniago, G. Medeiros-Ribeiro, A. Malachias, S. Kycia, T. I. Kamins, and R. Stan Williams. *Phys. Rev. B*, **66**:245312, 2002. 6

[45] A. Malachias, S. Kycia, G. Medeiros-Ribeiro, R. Magalhaes-Paniago, T. I. Kamins, and R. Stanley Williams. *Phys. Rev. Lett.*, **91**:176101, 2003. 6

[46] S. Marchesini, H. He, H. N. Chapman, S. P. Hau-Riege, A. Noy, M. R. Howells, U. Weierstall, and J. C. H. Spence. *Phys. Rev. B*, **68**:140101, 2003. 2

[47] C. O. McPheeters, C. J. Hill, D. Z. Hu, S. H. Lim, D. Derkacs, D. Z. Ting, D. M. Schaadt, S. D. Gunapala, and E. T. Yu. *Proc. SPIE*, **7772**:777209, 2010. 1

[48] T.H. Metzger, I. Kegel, R. Paniago, A. Lorke, J. Peisl, J. Schulze, I. Eisele, P. Schittenhelm, and G. Abstreiter. *Thin Solid Films*, **336**:1–8, 1998. 2, 6, 34

[49] A. Meyer. *web page: www.gisaxs.de*, pages Institute of Physical Chemistry – University of Hamburg, 2011. 23, 25, 103, 104

[50] R. P. Millane and W. J. Stroud. *J. Opt. Soc. Am. A*, **14**:568, 1997. 2

[51] A. A. Minkevich, T. Baumbach, M. Gailhanou, and O. Thomas. *Phys. Rev. B*, **78**:174110, 2008. 2

[52] A. A. Minkevich, T. Baumbach, M. Gailhanou, and O. Thomas. *Phys. Rev. B*, **78**:174110, 2008. 2

[53] A. A. Minkevich, M. Gailhanou, J.-S. Micha, B. Charlet, V. Chamard, and O. Thomas. *Phys. Rev. B*, **76**:104106, 2007. 2

[54] M.I.Richard, T.U.Schülli, E. Wintersberger, G. Renaud, and G.Bauer. *NIM B*, **246**:35–38, 2006. 26

[55] M.Kaufholz. *diploma thesis*, 2010. 70, 107

[56] N. Moll, M. Scheffler, and E.Pehlke. *Phys. Rev. B*, **58**:4566–4571, 1998. 80

[57] M.Riotte, D.Grigoriev, P.Schroth, M.Kaufholz, A.A.Minkevich, E.Fohtung, T.Slobodskyy, S.Lazarev, T.Schlereth, S.Hfling, A.Forchel, D.Lbbert, T.Cornelius, T.H.Metzger, and T. Baumbach. *in process*, pages Grazing Incidence X–ray Diffraction for fast in–situ Characterization of Quantum Dots, 2011. 88

[58] J. Novac. *Phd thesis*, page Masaryk University and Johannes Kepler Universität Linz, 2006. 21, 103

[59] A.J. Nozik. *Physica E*, **14**:115, 2002. 1

[60] Robert Leroy Taylor J. Z. Zhu O. C. Zienkiewicz, R. L. Taylor. *The finite element method: its basis and fundamentals*. Butterworth-Heinemeann, 2000. 43

[61] T. Passow, S. Li, P. Feinugle, T. Vallaitis, J. Leuthold, D. Litvinov, D. Gerthsen, and M. Hetterich. *Journal of Appl. Phys.*, **102**:073511, 2007. 2

[62] E. Pehlke, N. Moll, A. Kley, and M. Scheffler. *Appl. Phys. A*, **65**:525–534, 1997. 80

[63] E. Penev, P. Kratzer, and Matthias Scheffler. *Phys. Rev. B*, **64**:085401, 2001. 87

[64] M. A. Pfeifer, G. J. Williams, I. A. Vartanyants, R. Harder, and I. K. Robinson. *Nature*, **442**:63, 2006. 2

[65] Z. G. Pinsker. *Dynamical Scattering of X-rays in Crystals*. Springer, 1978. 5

[66] P.Kratzer, Q. K. K. Liu, P. Acosta-Diaz, C. Manzano, G. Costantini, R. Songmuang, A. Rastelli, O.G.Schmidt, and K. Kern. *Phys. Rev. B*, **73**:205347, 2006. 80, 81, 108

[67] E. Placidi, A. Della Pia, and F.Arciprete. *Appl. Phys. Lett*, **94**:021901, 2009. 84, 85

[68] P.R. Pukite, C.S. Lent, and P.I. Cohen. *Surf. Sci*, **161**:39, 1985. 29

[69] Markus Rauscher, Rogerio Paniago, Hartmut Metzger, Zoltan Kovats, Jan Domke, and Johann Peisl. *J. Appl. Phys.*, **86**:6763, 1999. 21

[70] G. Renaud, R. Lazzari, C. Revenant, A. Barbier, M. Noblet, O. Ulrich, F. Leroy, J. Jupille, Y. Borensztein, C. R. Henry, J.P. Deville, F. Scheurer, J. Mane-Mane, and O. Fruchart. *Science*, **300**:1416–1419, 2003. 2

[71] C. Revenant, F. Leroy, G. Renaud, R. Lazzari, A. Letoublon, and T. Madey. *Surface Science*, **601**:34313449, 2007. 2

[72] M.I. Richard, V. Favre-Nicolin, G. Renaud, T. U. Schlli, C. Priester, Z. Zhong, and T.-H. Metzger. *Appl. Phys. Lett*, **94**:013112, 2009. 69

[73] Fernando Rinaldi. *Annual Report 2002, Optoelectronics Department, University of Ulm*, 2002. 77, 78, 107

[74] M. Riotte. *report de stage*, page CEA Grenoble, 2006. 26

[75] M. Riotte, E. Fohtung, D. Grigoriev, A. A. Minkevich, T. Slobodskyy, M. Schmidbauer, T. H. Metzger, D.Z. Hu, D. M. Schaadt, and T. Baumbach. *Appl. Phys. Lett.*, **96**:083102, 2010. 29, 81, 104

[76] I. Robinson and R. Harder. *Nature Materials*, **8**:291, 2009. 2

[77] M. Rosini, P. Kratzer, and R. Magri. *J. Phys.: Condens. Matter*, **21**:355007, 2009. 87

[78] Marcello Rosini, Maria Clelia Righi, Peter Kratzer, and Rita Magri1. *Phys. Rev. B.*, **79**:075302, 2009. 87

[79] D. M. Schaadt, D. Z. Hu, and K. H. Ploog. *J. Vac. Sci. Technol. B*, **24(4)**:2069, 2006. 81

[80] D. M. Schaadt, S. Krauss, R. Koch, and K. H. Ploog. *Appl. Phys. A - Mater. Sci. Proc.*, **83**:267, 2006. 80

[81] T. W. Schlereth, C. Schneider, S. Höfling, and A. Forchel. *Nanotechnology*, **19**:045601, 2008. 74, 88, 89, 92, 93, 94, 96, 108, 109, 111

[82] M. Schmidbauer, Sh. Seydmohamadi, D. Grigoriev, Zh. M. Wang, Yu. I. Mazur, P. Schäfer, M. Hanke, R. Köhler, and G. J. Salamo. *Phys. Rev. Lett.*, **96**:066108, 2006. 3

[83] M. Schmidbauer, Sh. Seydmohamadi, D. Grigoriev, Zh. M. Wang, Yu. I. Mazur, P. Schäfer, M. Hanke, R. Köhler, and G. J. Salamo. *Phys. Rev. Lett.*, **96**:066108, 2006. 82

[84] M. Schmidbauer, Zh. M. Wang, Yu. I. Mazur, P. M. Lytvyn, G. J. Salamo, D. Grigoriev, P. Schäfer, R. Köhler, and M. Hanke. *Appl. Phys. Lett.*, **91**:093110, 2007. 82, 83, 85, 86, 87

[85] W. V. Schoenfeld, T. Lundstrom, P. M. Petroff, and D. Gershoni. *Appl. Phys. Lett.*, **74**:2194, 1999. 1

[86] P. Schroth. *diploma thesis: In-situ Untersuchung von selbstorganisierten InAs/GaAs Quantenpunkten*, 2011. 43, 46

[87] T. U. Schülli, G. Vastola, M.-I. Richard, A. Malachias, G. Renaud, F. Uhlik, F. Montalenti, G. Chen, L. Miglio, F. Schäffler, and G. Bauer4. *Phys. Rev. Lett.*, **102**:025502, 2009. 2, 6, 34, 97

[88] W. Seifert, N. Carlsson, M. Miller, M. E Pistol, L. Samuelson, , and L. R Wallenberg. *Prog. Crystal Growth and Charact.*, **33**:423–471, 1996. 82, 108

[89] Q. Shen and S. Kycia. *Phys. Rev. B*, **55**(23):15791, 1997. 2

[90] X. Q. Shen and T. Nishinaga. *Journal of Crystal Growth*, **146**:374, 1995. 87

[91] B.J. Spencer and J.Tersoff. *Phys. Rev. Lett.*, **79**:4858–4861, 1997. 80

[92] G. Springholz, V. Holý, M. Pinczolits, and G. Bauer. *Science*, **282**:734, 1998. 82

[93] C.e C. Spyrakos. *Finite Element Modeling in Engineering Practice*. 1996. 43

[94] J. Stangl, V. Hol, and G. Bauer. *Rev. Mod. Phys.*, **76**:725–783, 2004. 6

[95] J. Stangl, T. Roch, V. Holý, M. Pinczolits, G. Springholz, G. Bauer, I. Kegel, T. H. Metzger, J. Zhu, K. Brunner, G. Abstreiter, and D. Smilgies. *J. Vac. Sci. Technol. B*, **18**:2187, 2000. 85

[96] R.A. Swalin. *John Wiley and Sons*, 1972. 77

[97] M. Sztucki. *Phd Thesis Universität München*, 2004. 80, 108

[98] S. Takagi. *J. Phys. Soc. Jpn.*, **26**:1239, 1969. 5

[99] Masamitu Takahasi, Toshiyuki Kaizu, and Junichiro Mizuki. *Appl. Phys. Lett.*, **88**:101917, 2006. 2

[100] X.-D. Wang, N. Liu, C. K. Shiha, S. Govindaraju, and A. L. Holmes Jr. *Appl. Phys. Lett*, **85**:1356, 2004. 82

[101] Zh. M. Wang, H. Churchill, C. E. George, and G. J. Salamo. *J. Appl. Phys.*, **96**:6908, 2004. 82

[102] Zh. M. Wang, C. Rodriguez, Sh. Seydmohamadi, Yu. I. Mazur, Y. Z. Xie, and G. J. Salamo. *Appl. Phys. Lett*, **94**:083107, 2009. 82

[103] G. J. Williams, M. A. Pfeifer, I. A. Vartanyants, and I. K. Robinson. *Phys. Rev. Lett.*, **90**:175501, 2003. 2

[104] G. J. Williams, H. M. Quiney, B. B. Dhal, C. Q. Tran, K. A. Nugent, A. G. Peele, D. Paterson, and M. D. de Jonge. *Phys. Rev. Lett.*, **97**:025506, 2006. 2

[105] J. Wollschläger and M Larson. *Phys. Rev. B*, **57**:14937, 7998. 30

[106] Y. Yoneda. *Phys. Rev.*, **131**:2010, 1963. 25